

*Università degli Studi di Napoli "Federico II"*



*Facoltà Ingegneria  
Dipartimento Ingegneria Aerospaziale*

Doctoral Thesis in Aerospace Engineering

# **Multi-Objective Numerical Optimization Applied to Aircraft Design**

Francesco Grasso

Tutor  
Prof. Domenico P. Coiro

Coordinator  
Prof. Antonio Moccia

December 2008







# Contents

Contents .....	5
List of Figures .....	7
List of Tables .....	12
List of Symbols .....	13
Chapter 1 .....	17
Introduction .....	17
1.1 General .....	17
1.2 Summary of Proposed Work .....	20
Chapter 2 .....	23
Numerical Optimization Methods .....	23
2.1 Basic Optimization Mathematical Formulation .....	23
2.2 Choice of Optimization Method .....	24
2.2.1 Gradient-Based Algorithms .....	24
2.2.2 Response Surface Methodology .....	24
2.2.3 Genetic Algorithms .....	25
2.2.4 Simulated Annealing .....	26
2.3 Gradient-Based Algorithms .....	27
2.3.1 The General Idea .....	27
2.3.2 The Mathematical Formulation .....	29
Chapter 3 .....	31
Airfoil Design and Optimization .....	31
3.1 Introduction .....	31
3.2 Geometry Parameterization .....	31
3.2.1 3 <sup>rd</sup> Degree Bezier Curves Properties .....	34
3.2.2 3 <sup>rd</sup> Bezier Curves Usage in Airfoil Shape Reconstruction .....	36

3.2.3	A critical point: the connection between two Bezier curves.....	39
3.3	Choice of Constraints.....	42
3.3.1	Geometrical Constraints.....	43
3.3.2	Aerodynamic Constraints.....	43
3.4	Objective Function Evaluation.....	45
3.5	Numerical Examples.....	46
3.5.1	High Lift Airfoil – Single Point Approach .....	47
3.5.2	High Aerodynamic Efficiency Airfoil .....	50
3.5.3	High Endurance Airfoil for Sailplanes – Dual Point Approach .....	57
3.5.4	Low-Drag Airfoil – Dual Point Approach .....	60
3.5.5	Airfoil for a S.T.O.L. High-Speed Ultra-Light Aircraft – Dual Point Approach .....	63
3.5.6	Multi-Element Airfoil; Gap and Overlap Optimization.....	66
3.6	Different Approaches Comparison .....	69
3.6.1	User’s Knowledge.....	69
3.6.2	Optimum Condition .....	70
3.6.3	Aerodynamic Solver Limitations.....	70
3.6.4	Autonomous Process.....	71
Chapter 4	.....	73
Lifting Surfaces Design and Optimization	.....	73
4.1	Introduction.....	73
4.2	VWING Numerical Code.....	73
4.2.1	Overview.....	73
4.2.2	The Mathematical Formulation.....	74
4.2.3	Preliminary Validation Tests .....	81
4.2.4	Low Aspect-Ratio Surfaces Improvement: Losito’s Formulation.....	87
4.2.5	Stall and Post-Stall Improvement: Chattot’s Artificial Viscosity.....	89

4.2.6	Non Conventional Surfaces .....	92
4.3	Numerical Optimization Examples .....	102
4.3.1	Chord Distribution Optimization .....	102
4.3.2	Twist Angle Distribution Optimization .....	106
4.3.3	Dihedral Angle Distribution Optimization ...	109
Chapter 5	.....	115
Conclusions and Future Works	.....	115
5.1	Conclusions .....	115
5.2	Future Works.....	116
Appendix A: Publications	.....	117
Appendix B: Optfoil user's Manual	.....	161
References	.....	168

## List of Figures

Fig. 1	Some of the disciplines involved in aircraft design.....	17
Fig. 2	Sequential block structured design loop; "Easy-fly" project.....	18
Fig. 3	Numerical optimization usage design loop.....	19
Fig. 4	Simple example of optimization problem.....	27
Fig. 5	Optimization scheme. ....	28
Fig. 6	Examples of Bezier Curve Control Polygon. ....	34
Fig. 7	Piecewise approach example. ....	36
Fig. 8	NACA 0012 airfoil reconstruction (deformed). ....	37
Fig. 9	NACA 4412 airfoil reconstruction (deformed). ....	37
Fig. 10	NLF0115 airfoil reconstruction (deformed). ....	38
Fig. 11	S1223 airfoil reconstruction (deformed). ....	38

Fig. 12 Effect of an arbitrary modification in the position of control points; no correction. ....	40
Fig. 13 Effect of an arbitrary modification in the position of control points; correction. ....	40
Fig. 14 Inviscid pressure distribution without correction; XFOIL calculation. ....	41
Fig. 15 Inviscid pressure distribution with correction; XFOIL calculation. ....	41
Fig. 16 Optimizer-solver connection scheme. ....	45
Fig. 17 S1223 airfoil. ....	47
Fig. 18 NACA0012 baseline and location of degrees of freedom. ....	47
Fig. 19 Objective Function History.....	48
Fig. 20 Configuration "A".....	48
Fig. 21 Comparison between the baseline, the final geometry and the S1223 airfoil. ....	49
Fig. 22 Comparison between the baseline, the final geometry and the S1223 airfoil; trailing edge zone detail. ....	49
Fig. 23 G1 airfoil and used degrees of freedom.....	50
Fig. 24 Optimal shape 1. ....	51
Fig. 25 Optimal shape 2. ....	51
Fig. 26 GT1 airfoil. ....	51
Fig. 27 Comparison between aerodynamic efficiency of geometries. ....	52
Fig. 28 Optimal geometry; $k=0.25$ .....	55
Fig. 29 Optimal geometry; $k=0.4$ .....	55
Fig. 30 Optimal geometry; $k=0.5$ .....	55
Fig. 31 Optimal geometry; $k=0.6$ .....	55
Fig. 32 Pareto frontier. ....	56
Fig. 33 Aerodynamic efficiency curve; comparison between different solutions. ....	56
Fig. 34 Pareto frontier. ....	58
Fig. 35 Final geometry; $k=0.3$ .....	59



Fig. 36 Final geometry; $k=0.5$ .....	59
Fig. 37 Final geometry; $k=0.6$ .....	59
Fig. 38 Comparison between baseline, final geometry ( $k=0.6$ ) and SM701. ....	59
Fig. 39 Pareto frontier. ....	61
Fig. 40 Final geometry; $k=0.2$ .....	61
Fig. 41 Final geometry; $k=0.3$ .....	61
Fig. 42 Final geometry; $k=0.5$ .....	62
Fig. 43 Final geometry; $k=0.8$ .....	62
Fig. 44 Comparison between drag polar curves.....	62
Fig. 45 Pareto frontier. ....	64
Fig. 46 Optimal geometry; $k=0.02$ .....	65
Fig. 47 Optimal geometry; $k=0.05$ .....	65
Fig. 48 Optimal geometry; $k=0.07$ .....	65
Fig. 49 Optimal geometry; $k=0.1$ .....	65
Fig. 50 Optimal geometry; $k=0.8$ .....	65
Fig. 51 G1F airfoil. ....	66
Fig. 52 30P30N airfoil. ....	66
Fig. 53 Modified 30P30N airfoil.....	66
Fig. 54 Comparison between initial and final configuration. .	67
Fig. 55 Objective function time history. ....	68
Fig. 56 Lift coefficient map; comparison between numerical and experimental data. ....	68
Fig. 57 Horseshoe vortices distributed along the quarter chord of a finite wing with sweep and dihedral. ....	75
Fig. 58 Position vectors describing the geometry for a horseshoe vortex. ....	75
Fig. 59 Unit vectors describing the orientation of the local airfoil section.....	79
Fig. 60 Spanwise aerodynamic load; comparison between VWING and exact solution; $\alpha=5.71^\circ$ . ....	82
Fig. 61 Spanwise lift coefficient; comparison between VWING and exact solution; $\alpha=5.71^\circ$ . ....	82

Fig. 62 Effect of number of assigned stations in terms of lift coefficient; $\alpha=4^\circ$ .....	83
Fig. 63 Tapered wing. ....	83
Fig. 64 Rectangular wing - Spanwise lift coefficient distribution; comparison between VWING and Multhopp method, $\alpha=5^\circ$ .....	84
Fig. 65 Tapered wing - Spanwise lift coefficient distribution; comparison between VWING and Multhopp method, $\alpha=5^\circ$ ..	84
Fig. 66 Induced drag coefficient; comparison between fixed wake and free wake.....	85
Fig. 67 Lift coefficient; comparison between fixed wake and free wake.....	86
Fig. 68 Oswald factor; comparison between fixed wake and free wake.....	86
Fig. 69 Comparison between VWING numerical code and Vortex Lattice Method; aerodynamic load along the span, $\alpha=3^\circ$ .....	88
Fig. 70 Comparison between VWING numerical code and Vortex Lattice Method; aerodynamic load along the span, $\alpha=6^\circ$ .....	89
Fig. 71 coefficient curve; effect of artificial viscosity factor..	90
Fig. 72 Lift coefficient curve; effect of artificial viscosity factor, detail. ....	91
Fig. 73 Aerodynamic load along span; effect of artificial viscosity term, $\alpha=20^\circ$ .....	91
Fig. 74 Planform configuration.....	93
Fig. 75 Winglet configuration.....	94
Fig. 76 Wake visualization; free wake model used. ....	94
Fig. 77 Blended winglet configuration. ....	95
Fig. 78 Wing shape. ....	96
Fig. 79 Wing geometry. ....	97
Fig. 80 Wing with multiple winglets during the experimental tests.....	98

Fig. 81 Effect of gap on aerodynamic load.....	98
Fig. 82 Effect of percent gap on the Oswald factor. ....	99
Fig. 83 Drag polar curve; numerical-experimental comparison. .....	100
Fig. 84 Efficiency curve; numerical-experimental comparison .....	101
Fig. 85 Endurance parameter curve; numerical-experimental comparison.....	101
Fig. 86 Wing's geometrical characteristics. ....	103
Fig. 87 Objective function history. ....	103
Fig. 88 Degrees of freedom history. ....	104
Fig. 89 Non optimal configurations. ....	104
Fig. 90 Optimal configuration.....	105
Fig. 91 Chord distribution along the span; effect of degrees of freedom increasing. ....	105
Fig. 92 Objective function history. ....	107
Fig. 93 Degrees of freedom history. ....	107
Fig. 94 Final configuration.....	108
Fig. 95 Some of the unfeasible configurations. ....	108
Fig. 96 Twist angle distribution along the span; effect of degrees of freedom increasing. ....	109
Fig. 97 Initial configuration. ....	110
Fig. 98 Objective function history. ....	111
Fig. 99 Degrees of freedom history. ....	111
Fig. 100 Configuration A.....	112
Fig. 101 Configuration B. ....	112
Fig. 102 Configuration C. ....	113
Fig. 103 Optimal configuration.....	113

## List of Tables

Table 1: Comparison between different mathematical formulations. ....	32
Table 2: Geometrical and aerodynamic constraints. ....	42
Table 3: Design parameters. ....	47
Table 4: Optimization results. ....	48
Table 5: Design conditions. ....	50
Table 6: Optimization results. ....	51
Table 7: Design parameters. ....	54
Table 8: Optimization results. ....	54
Table 9: Design parameters. ....	57
Table 10: Optimization results for several values of k parameter. ....	58
Table 11: Design parameters. ....	60
Table 12: Optimization results. ....	60
Table 13: Design conditions. ....	63
Table 14: Optimization results. ....	64
Table 15: Evolution of degrees of freedom and objective function during the optimization process. ....	67
Table 16: Free wake and fixed wake; elapsed time comparison. ....	85
Table 17: Comparison between VWING numerical code and Vortex Lattice Method. ....	88
Table 18: Summary of analyzed configurations. ....	92
Table 19: Comparison between OLD and VWING; winglets. ....	93
Table 20: Wing characteristics. ....	97
Table 21: Degrees of freedom and bounds. ....	102
Table 22: Initial, final values of design variables and their bounds. ....	106
Table 23: Initial, final values of degrees of freedom and their bounds. ....	110

## List of Symbols

### Latin

a	amplitude of movement along the search direction
AR	aspect ratio
c	chord
Cd	drag coefficient
$Cd_{\min}$	minimum drag coefficient
Cl	lift coefficient
$Cm_{c/4}$	moment coefficient respect to the 25% of the chord
$dA_i$	differential planform area at control point i
dF	differential aerodynamic force vector
dl	directed differential vortex length vector
F(X)	objective function
g	inequality constraint
G	dimensionless vortex strength vector
$G_i$	dimensionless vortex strength for section i
h	equality constraint
J	N by N matrix of partial derivatives
k	weight factor
$p_0$	static pressure
$p_v$	vapor pressure
q	dynamic pressure
R	residual vector
$r_0$	vector from beginning to end of vortex segment
$r_1$	vector from beginning of vortex segment to arbitrary point in space
$\overline{r_1}$	magnitude of $r_1$
$r_2$	vector from end of vortex segment to arbitrary point in space
$\overline{r_2}$	magnitude of $r_2$
Re	Reynolds number
S	search direction

$u_\infty$	unit vector in direction of the freestream
$u_{ai}$	chordwise unit vector at control point $i$
$u_{ni}$	normal unit vector at control point $i$
$V$	local fluid velocity
$V_\infty$	velocity of the uniform flow or freestream
$v_{ij}$	dimensionless velocity induced at control point $j$ by vortex $i$ , having a unit strength
$X$	design variable vector
$X^L$	lower bound vector
$X^U$	upper bound vector
<b>Greek</b>	
$\alpha$	angle of attack
$\alpha_i$	local angle of attack for wing section $i$
$\Gamma$	vortex strength in the direction of $r_0$
$\rho$	fluid density
$\sigma_v$	cavitation parameter







# Chapter 1

## Introduction

### 1.1 General

Aircraft design is a very complex process because several disciplines are involved at the same time: aerodynamics, structures, performances, propulsion, costs.

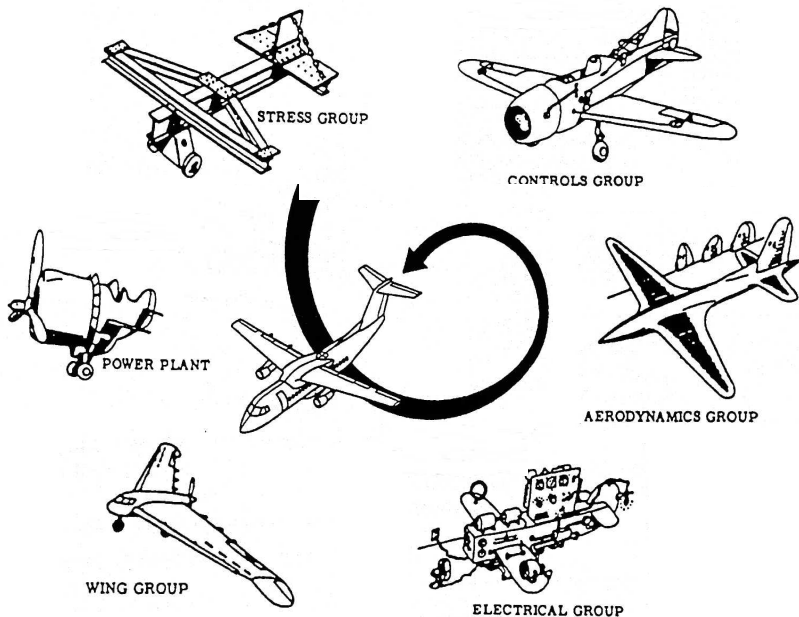


**Fig. 1** Some of the disciplines involved in aircraft design.

From this point of view, the real aircraft is a compromise between several requirements, often each conflicting with each other.

An important consequence of this research of a good compromise, is that, in general, the overall design process is a succession of blocks, each one connected with more blocks; this means that it is not easy to decide when to “freeze” a configuration.

It is possible to find this block structure also in design of single components. In the case for example, of airfoil design, the designer should take into account airfoil’s aerodynamic requirements, aircraft performances requirements and feasibility requirements (Fig. 2).

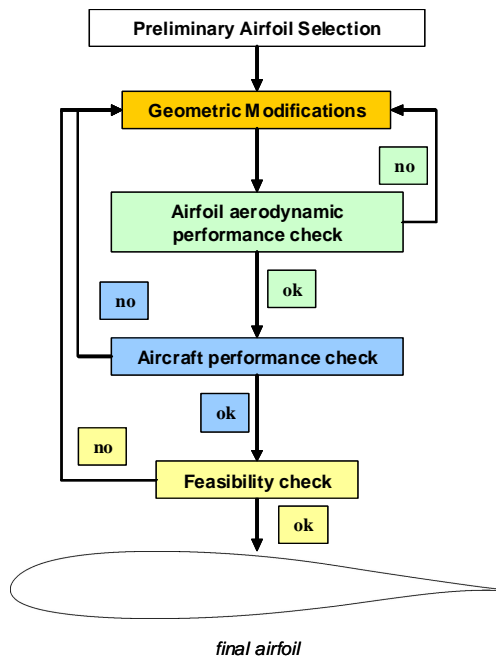


**Fig. 2** Sequential block structured design loop; "Easy-fly" project.

The main goal of the present research is to propose the usage of numerical optimization concepts as a new approach for aircraft design and investigate the potentialities of this new approach. Numerical optimization is the mathematical formulation of the optimum-finding problem; more in general, numerical optimization is central to any problem involving decision making, whether in engineering or in economics. The task of decision making entails choosing between various alternatives. This choice is governed by our desire to make the "best" decision. In this sense, numerical optimization can be applied also in design problems.

With reference at the previous example, from conceptual point of view, by applying numerical optimization approach it is possible to pass from a sequential design scheme to a different scheme in which any requirement and constraint is considered at the same time. In this way, the "optimal" geometry should be closer to the final, "ready-to-construction" product.

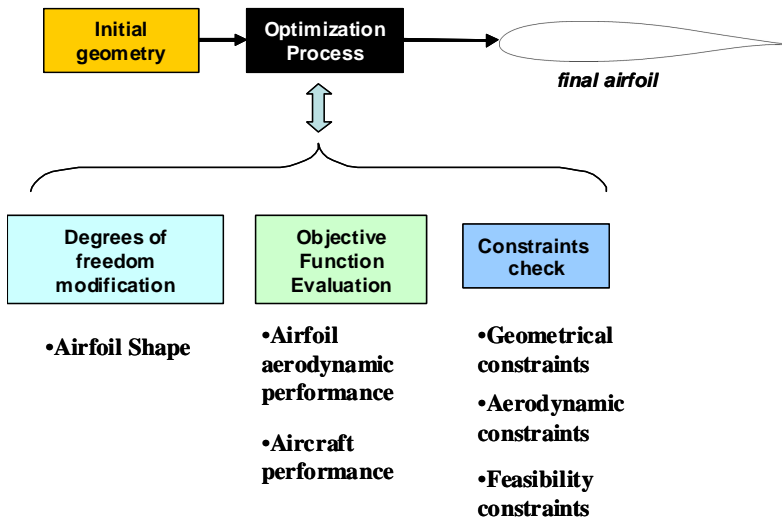


Fig. 3 Numerical optimization usage design loop.

The main advantages of this approach are evidently, the opportunity to reduce design time and development costs. This is because any kind of parameters regarding the airfoil or more in general the aircraft and any kind of constraints are taken into account during the same block of optimization process. In other words, by using this approach it is possible to condensate several steps in one step only.

In order to “build” an optimization process, several ingredients are necessary:

- choice of optimization method
- choice of parameterization
- evaluation of objective function
- choice of constraints

In the present thesis the attention is focused on aerodynamic and performances aspects of the aircraft design, but the approach is very versatile and easy to adapt to different contexts.

## ***1.2 Summary of Proposed Work***

As outlined in the previous paragraph, in order to “build” an optimization process, several ingredients should be developed. The first one of these ingredients is the choice of the optimization method. In the first part of the present work, an investigation about the different optimization methods developed during years is performed. This is done because, in dependence of the practical problem to solve, a particular optimization method can work better than another one. In this context, the concept of better working is not only a problem in terms of elapsed time to obtain the optimum, but it concerns

the validity of the optimum configuration. This investigation is the topic of the next chapter.

The rest of the research is developed in two different and independent sections. In the first one, numerical optimization is applied to airfoil design problem; in the second section, numerical optimization is applied to lifting surfaces design problem.

In the third chapter of this work, the use of numerical optimization for airfoil design problem is investigated; in particular, both the shape and the position between elements are used as degrees of freedom. The problems connected with the choice of geometrical parameterization and constraints have been studied. In particular, several geometrical parameterizations have been considered and compared. Different constraints, both geometrical and aerodynamic, have been implemented.

The fourth chapter is dedicated to lifting surfaces design. Here, the work is focused on the development of a new aerodynamic solver, based on a new generalized formulation of the Prandtl's lifting line theory. This formulation is deeply explained and validated through a lot of numerical examples in which, both conventional and non conventional configurations are used.

In both two chapters, a lot of importance is given to the practical use of numerical optimization to design airfoils and lifting surface.

At the end of the thesis, in appendix A, some publications are present.



## Chapter 2

# Numerical Optimization Methods

### ***2.1 Basic Optimization Mathematical Formulation***

In the most general sense, numerical optimization solves the nonlinear, constrained problem to find the set of design variables,  $X_i$ ,  $i=1, N$ , contained in vector  $\mathbf{X}$ , that will

$$\text{minimize } F(X) \qquad \text{eq 1}$$

subjects to:

$$g_j(X) \leq 0 \qquad j = 1, M \qquad \text{eq 2}$$

$$h_k(X) = 0 \qquad k = 1, L \qquad \text{eq 3}$$

$$X_i^L \leq X_i \leq X_i^U \qquad j = 1, N \qquad \text{eq 4}$$

Eq1 defines the objective function which depends on the values of the design variables,  $\mathbf{X}$ . Equations 2 and 3 are inequality and equality constraints respectively, and equation 4 defines the region of search for the minimum. The bounds defined by equation 4 are referred to as side constraints.

## **2.2 Choice of Optimization Method**

During years, a lot of optimization methods<sup>1,2,4</sup> have been proposed and developed, often starting from theoretical concepts and logics very far each from each other.

In general it is very difficult to state which method is the best because each one has several advantages and, at same time, disadvantages; just referring to a particular application, or problem, it is possible to operate this choice.

In this section, a brief overview of the most popular optimization methods is provided.

### **2.2.1 Gradient-Based Algorithms**

Gradient-based<sup>5</sup> (GB) search methods are a category of optimization techniques that use the gradient of the objective function to find an optimal solution. Each iteration of the optimization algorithm adjusts the values of the decision variables so that the simulation behaviour produces a lower objective function value. Each decision variable is changed by an amount proportionate to the reduction in objective function value. GB searches are prone to converging on local minima because they rely solely on the local values of the objective function in their search. They are best used on well-behaved systems where there is one clear optimum. GB methods will work well in high-dimensional spaces provided these spaces don't have local minima. Frequently, additional dimensions make it harder to guarantee that there are not local minima that could trap the search routine. As a result, as the dimensions (parameters) of the search space increases, the complexity of the optimization technique increases.

### **2.2.2 Response Surface Methodology**

Response surface methodology<sup>4</sup> (RSM) is a statistical method for fitting a series of regression models to the output of a



simulation model. The goal of RSM is to construct a functional relationship between the decision variables and the output to demonstrate how changes in the value of decision variables affect the output. RSM is useful at finding the right combination of decision variables that will satisfy some specification. Relationships constructed from RSM are often called meta-models. RSM usually consists of a screening phase that eliminates unimportant variables in the simulation. After the screening phase, linear models are used to build a surface and find the region of optimality. Then, second or higher order models are run to find the optimal values for decision variables. Factors that cause RSM to form misleading relationships include identifying an incomplete set of decision variables and failing to identify the appropriate constraints on those decision variables.

### **2.2.3 Genetic Algorithms**

Genetic algorithms<sup>3,4</sup> (GA) is a heuristic search method derived from natural selection and evolution. At the start of a GA optimization, a set of decision variable solutions are encoded as members of a population. There are multiple ways to encode elements of solutions including binary, value, and tree encodings. Crossover and mutation, operators based on reproduction, are used to create the next generation of the population. Crossover combines elements of solutions in the current generation to create a member of the next generation. Mutation systematically changes elements of a solution from the current generation in order to create a member of the next generation. Crossover and mutation accomplish exploration of the search space by creating diversity in the members of the next generation. One of advantages of GA is that multiple areas of the search space are explored to find a global minimum. Through the use of the crossover operator, GA are particularly

strong at combining the best features from different solutions to find one global solution. Through observation of these crossover combinations, the user gains insight about how parts of the simulation interact.

### **2.2.4 Simulated Annealing**

Simulated annealing<sup>4</sup> (SA) provides the user with an opportunity to combine exploitation and exploration. Exploitation comes from using gradient search, a simple algorithm that examines the nearby search space and moves towards the local minimum. Exploration comes from a stochastic element of the algorithm that causes deviation from the local minimum to other regions where improved solutions are possible. The stochastic nature of SA makes it well suited to find the minimum in systems that are not well behaved. The amount of randomness is controlled by two parameters: the initial temperature and cooling rate. The initial temperature determines the level of randomness in the algorithm while the cooling rate determines how quickly the level of randomness decreases as the number of iterations of the algorithm increase. Because of its exploration capability, SA is a good optimization technique to use where there are a large number of feasible solutions. If the algorithm is left to iterate indefinitely, the temperature slowly decreases, causing the amount of exploration to decrease and resulting in discovery of the global minimum.

Despite of their “just” local high accuracy, gradient-based algorithms have been preferred in the present research because of their intrinsic robustness and convergence speed. In the rest of this chapter, the principles of gradient-based algorithms are extensively explained.

## 2.3 Gradient-Based Algorithms

### 2.3.1 The General Idea

In order to explain the principles on which gradient-based algorithms are developed, a practical example is illustrated in Fig. 4.



Fig. 4 Simple example of optimization problem.

Two characters stay on the side of a hill and one of them is blindfolded. The objective function is to maximize his elevation on the hill in order to reach the top of the hill (or stay very close to the top). In terms of minimization, we will minimize the negative of the elevation so  $F(\mathbf{X}) = -\text{Elevation}$ . Remembering this, we can define all mathematics here assuming we will minimize  $F(\mathbf{X})$ . Also, our character must stay inside of several fences on the hill. These represent the inequality constraints.

Mathematically, the negative of the distance from each fence is the amount by which you satisfy the constraint. If you are touching a fence, the constraint value is zero. Remember that you are blindfolded so you can't see the highest point on the hill that is inside the fences. You must somehow search for this point. One approach would be to take a small step in the north-

south direction and another in the east-west direction and from that, estimate the slope of the hill. What you have done is to calculate the gradient of the objective function (-Elevation). This is a vector direction. The slope is the direction you might chose to search since this will move you up the hill at the fastest rate. This is called the “search” direction. Mathematically, this gradient of the objective is referred to as a direction of “steepest ascent.” Because we wish to minimize  $F(\mathbf{X})$ , we would move in the negative gradient, or “steepest descent” direction. It is possible to move in this direction until the crest of the hill is reached or a fence is encountered.



**Fig. 5 Optimization scheme.**

With reference at Fig. 5, it is possible to define  $X^0$  as the initial position and  $X^1$  as the position at the end of the first iteration.

$$X^1 = X^0 + a^* S^1 \quad \text{eq 5}$$

Where  $S^1$  is the search direction at the first iteration and  $a^*$  is the optimal amplitude of movement along  $S^1$  direction. By iterating this procedure, the complete optimization process can be described.

### 2.3.2 The Mathematical Formulation

The optimization problem is a process in which two steps are iteratively performed:

- Find a direction that will improve the objective while staying inside the fences.
- Search in this direction until no more improvement can be made by going in this direction.

About the search direction, this should be an “usable-feasible” direction, where a usable direction is one that improves the objective and a feasible direction is one that will keep you inside of the fence.

From a mathematical point of view, two conditions should be satisfied:

$$\nabla F(x)^T \cdot S \leq 0 \text{ (usable direction)} \quad \text{eq 6}$$

$$\nabla g_j(x)^T \cdot S \leq 0 \text{ (feasible direction)} \quad \text{eq 7}$$

In order to find the S direction, the left hand side of eq.6 should be as negative as possible and, at same time, the eq.7 should be satisfied.

In other words, there is a sub-optimization task to solve, in order to find the S direction.

$$\text{Minimize: } \nabla F(x)^T \cdot S$$

$$\text{Subject to: } \nabla g_j(x)^T \cdot S \leq 0 \text{ } j=1,J$$

In literature several gradient-based algorithms have been developed. In the present research some of these have been

implemented; in particular, Modified Feasible Direction (MFD), Sequential Linear Programming (SLP) and Sequential Quadratic Programming (SQP).

The basic difference between algorithms is the way to describe the objective function and the constraint functions in order to manage non linearity of these functions.

In the MFD algorithm, both objective and constraints are considered with their non linearity. In the SLP algorithm a Taylor series approximation to the objective and constraint functions are created. Then, this approximation is used for optimization instead of the original nonlinear functions. When the optimizer requires the values of the objective and constraint functions, these are very easily and inexpensively calculated from the linear approximation. Also, since the approximate problem is linear, the gradients of the objective and constraints are available directly from the Taylor Series expansion. The same concept is applied for the SQP algorithm; first, a Taylor series approximation is generated to the objective and constraint functions. However, instead of minimizing the linearized objective, a quadratic approximate objective function is used; the constraints are linearized.

On one hand, the MFD algorithm is more general and “closer” to the physic problem because it takes into account non linearity; on the other hand, the SLP and SQP algorithms could be faster because of their approximations. More details can be found in refs 5,6.

## Chapter 3

# Airfoil Design and Optimization

### **3.1 Introduction**

Both in aircraft design and in turbine design, the choice of airfoils is critical because it affects overall project performance. Often, an *ad hoc* designed airfoil is used.

A popular approach to do this is the inverse design technique; this method allows the airfoil geometry to be calculated from the pressure distribution on the airfoil surface.

The aim of this chapter is to apply numerical optimization concepts to the airfoil design problem.

In the next two paragraphs fundamental steps of numerical optimization are detailed explained: the choice of parameterization and the choice of constraints.

Then, several practical cases of airfoil design are proposed and solved by using numerical optimization approach.

At the end of this chapter, a comparison between this approach and the more “traditional” inverse design approach is provided.

### **3.2 Geometry Parameterization**

One of the most important ingredients in numerical optimization is the choice of design variables and the parameterization of our system by using these variables.

In general, an airfoil is given by its coordinates, typically a set of 150-200 points for panel codes; evidently, it is not possible to use directly the airfoil’s coordinates as design variables.

In order to reduce the number of parameters to take into account necessary to describe the airfoil's shape, but without geometrical information loss, several mathematical formulations have been proposed in literature.

Some of these formulations are here considered and compared. In particular, two criteria have been used to evaluate the formulations: the mathematical descriptive potentialities and the usage complexity from the user's point of view.

Parameterization	Advantages	Disadvantages
<b>Hicks-Henne Functions</b>	Few parameters	Harmonic expression
		Not easy user usage
<b>6<sup>th</sup> degree Legendre Function</b>	Polynomial expression	6 <sup>th</sup> degree expression
		Not easy inflection points controllability
<b>3<sup>rd</sup> degree Spline Curves</b>	Polynomial expression	Necessity of segmentation to accurate description
<b>3<sup>rd</sup> degree Bezier Curves</b>	Polynomial expression	Necessity of segmentation to accurate description
	Direct connection between parameters and geometry	
	Easy inflection points controllability	
	Easy user usage	
	Approximant formulation	

**Table 1: Comparison between different mathematical formulations.**



The first criterion takes into account the capability of the formulation to describe and control the airfoil shape. Because of the use in this context, regularity properties, derivative properties and control of inflection points are particularly important data to evaluate the potentialities of a formulation.

The second criterion takes into account the quantity of parameters necessary to describe the curve and the geometrical meaning of these parameters. The connection between mathematical formulation and geometrical interpretation is very important to help the designer to set up the design variables and to predict, for example, which zone of the airfoil will be modified; in this way also local modifications are possible.

Advantages and disadvantages for each formulation are summarized in Table 1.

Because of their harmonic expression, just two parameters (amplitude and phase) are necessary to manage the Hicks-Henne functions, but, at same time, for the same reason, it is quite difficult to control the position of inflection points, their quantity along the curve and in general to assign the range of variation for each parameter.

The main advantage of Legendre function is the polynomial expression, quite easy to manage, but its sixth degree leads to the same problems of Hicks-Henne function about the presence and the controllability of several inflection points.

From this point of view third degree Bezier curves and splines are more attractive. At the end of this comparative evaluation, the Bezier curves have been chosen as geometry parameterization; the advantages of this choice are explained in detail in the next section.

### 3.2.1 3<sup>rd</sup> Degree Bezier Curves Properties

In the following equation, the Bernstein expression of a 3<sup>rd</sup> degree Bezier curve is given.

$$P(t) = P_0(1-t)^3 + 3P_1t(1-t)^2 + 3P_2t^2(1-t) + P_3t^3 \quad \text{eq 8}$$

Where  $t$  is a parameter between 0 and 1.

In order to “build” a Bezier curve, its four coefficients  $P_0$ ,  $P_1$ ,  $P_2$  and  $P_3$  are necessary. In this case, these four coefficients are not just numbers, but they represent the coordinates of the control points of a polygonal domain that contains the curve.

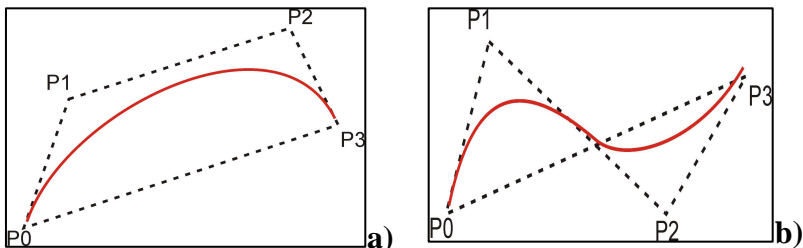


**Fig. 6 Examples of Bezier Curve Control Polygon.**

By applying this formulation to the problem of airfoil geometry description this characteristics allows the designer to easily control the four coefficients and set the range of variation for each one. Here, some other useful properties are showed.

- The two external control points coincide with the begin and the end of the curve
- The derivates at the begin and the end of the curve coincide with the directions of the control points connecting lines
- The curve is inside the convex domain generated by the control points

The last property is particularly interesting in airfoil design problems because it states that, if the domain is simply connected, no inflection points will be in the curve (and vice versa of course). First of all this means that the designer can a priori decide if he wishes or not, inflection points presence, but it means also that in a numerical optimization problem no special checks are necessary to control the presence of inflection points; these checks are mandatory for the other considered approaches.

By moving one of the control points, there will be an effect along all the curve. In order to allow optimizations also in localized zones of an airfoil, in the present research a “piece-wise” usage of Bezier curves is applied; in this way the airfoil geometry is divided in four sectors and an independent Bezier curve is used for each sector. With reference at Fig. 7, the control points from 1 to 4 cover the first sector, the control points from 4 to 7 the second sector, the control points from 7 to 10 the third one, the control points from 10 to 13 the fourth one. The control points 4, 7 and 10 are intersections between different Bezier curves and they should be managed in a special way.

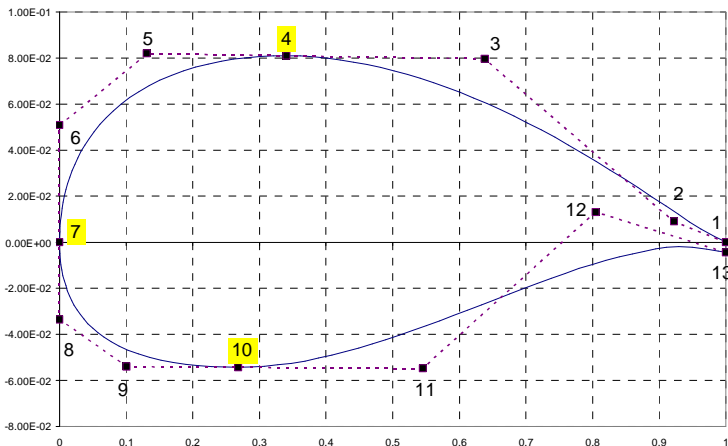


Fig. 7 Piecewise approach example.

### 3.2.2 3<sup>rd</sup> Bezier Curves Usage in Airfoil Shape Reconstruction

If the control points are assigned, no problems will be to generate the airfoil geometry and during an optimization process this is the way to use Bezier curves. Unluckily, at begin of a numerical optimization, it is necessary to know the initial values of our degrees of freedom (the control points); this means that if we decide to use a NACA0012 airfoil as baseline, we need to find the control points to generate the NACA 0012 airfoil.

This step is very important and a special algorithm has been designed and implemented to do this. In order to validate it, several airfoils have been considered; in the following figures the original shape and the shape generated starting from the calculated control points, are compared.

This is also the way to demonstrate that the 3<sup>rd</sup> degree Bezier curves offer a very general approach to obtain smooth airfoil geometries.

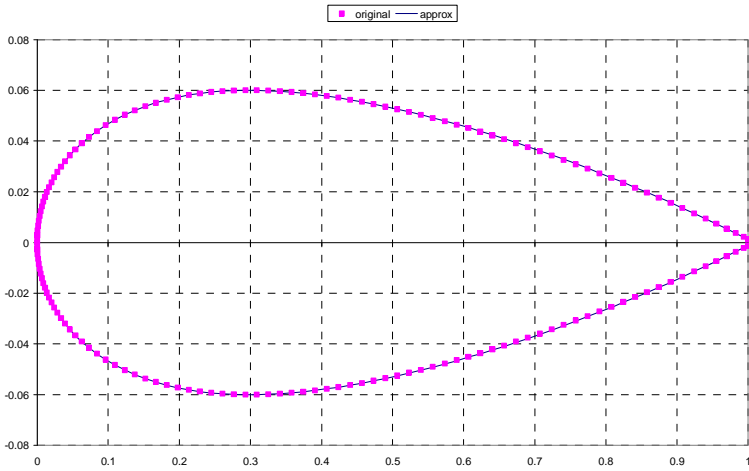


**Fig. 8 NACA 0012 airfoil reconstruction (deformed).**

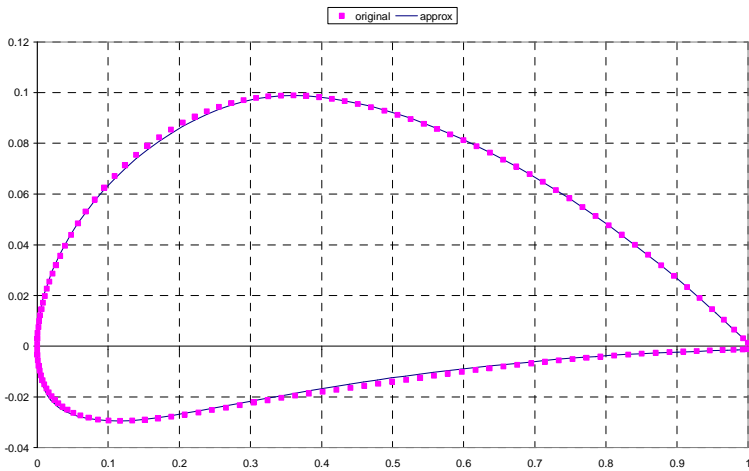


**Fig. 9 NACA 4412 airfoil reconstruction (deformed).**

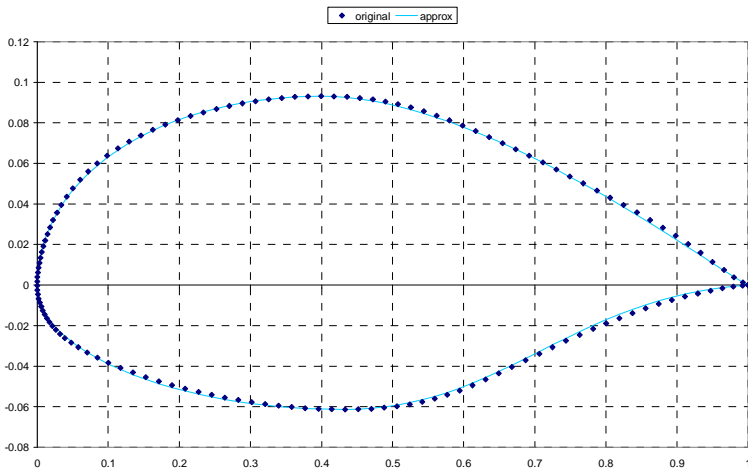


**Fig. 10 NLF0115 airfoil reconstruction (deformed).**

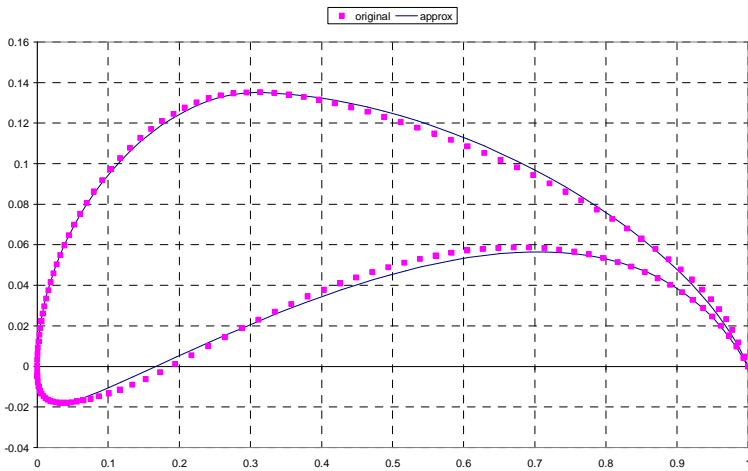


**Fig. 11 S1223 airfoil reconstruction (deformed).**

### **3.2.3 A critical point: the connection between two Bezier curves**

The connection points between two consecutive Bezier curves represent a critical aspect of this proposed approach to describe the airfoil geometry. This is due to the fact that, in order to have a smooth geometry, the continuity of the curve and of its derivatives should be guaranteed; during an optimization process, specially when a gradient based algorithm is used, it can be not easy to do.

In this section, a possible solution to this problem is illustrated and tested.

The idea is that the connection point between two Bezier curves and the directly connected ones should be aligned on the same straight line; in this way, the connection line between the control points and its derivatives are continuous and, of consequence, the airfoil geometry is smooth.

To test this idea, the NACA0012 airfoil has been considered and its control points have been calculated; then, an arbitrary modification to one of the control points adjacent to the intersection between two Bezier curves has been imposed; by using the “MDES” tool of XFOIL code, the inviscid velocity distribution on the airfoil has been calculated.

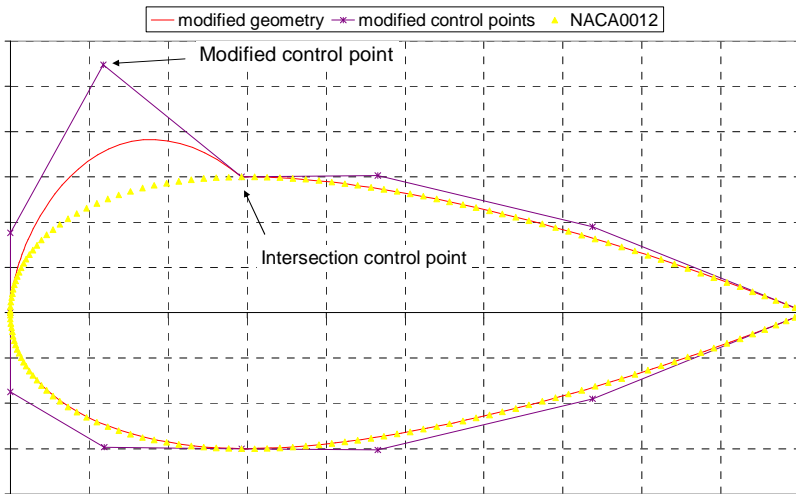


**Fig. 12 Effect of an arbitrary modification in the position of control points; no correction.**

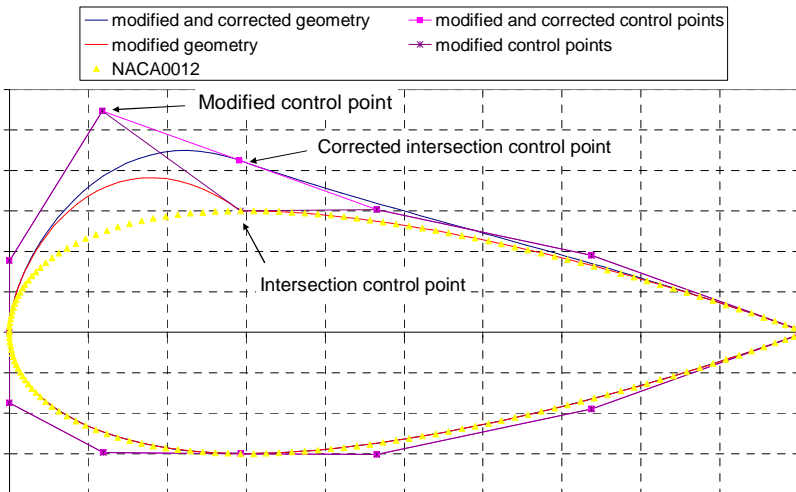


**Fig. 13 Effect of an arbitrary modification in the position of control points; correction.**



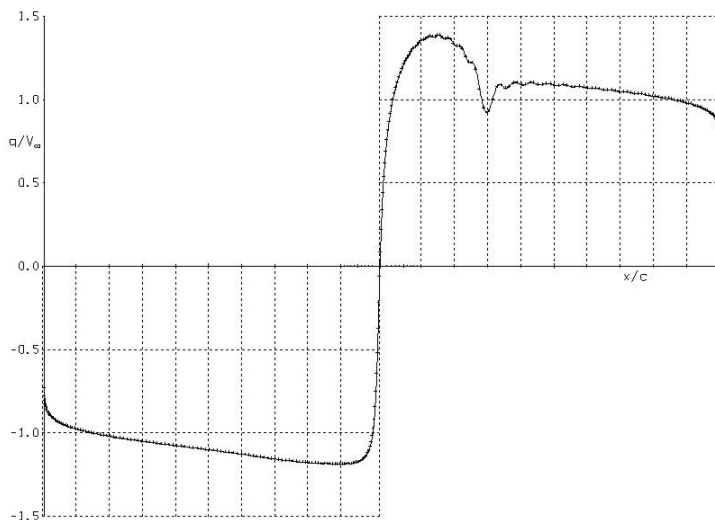


**Fig. 14** Inviscid pressure distribution without correction; XFOIL calculation.

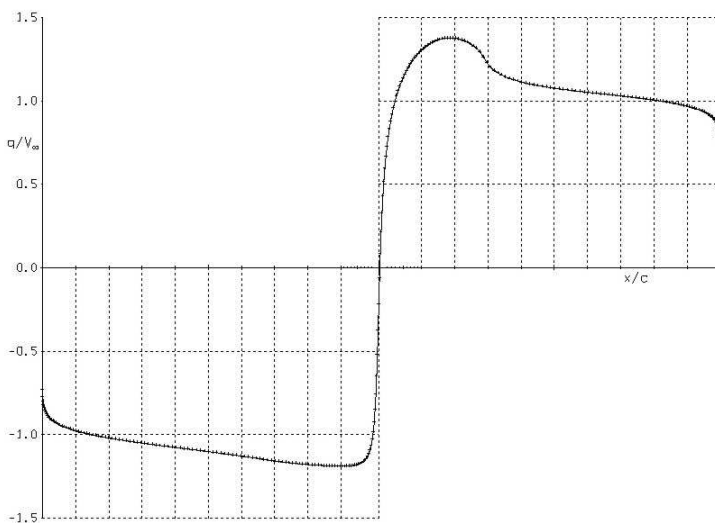


**Fig. 15** Inviscid pressure distribution with correction; XFOIL calculation.

From Fig. 14 and Fig. 15 it is evident the positive effect of the proposed correction: after correction there is not irregularity or “noise” in the pressure distribution.

### 3.3 Choice of Constraints

In airfoil design problems, in order to obtain a realistic geometry, several constraints should be taken into account; some of these are geometrical constraints, some of these are aerodynamic constraints.

In the present research, both geometrical and aerodynamic constraints have been considered and integrated in the optimization process (Table 2); in this paragraph a description for each constraint is provided.

Geometrical Constraints	Airfoil Minimum Thickness
	Airfoil Maximum Thickness
	Minimum Gap
	Minimum Thickness at specific location
Aerodynamic Constraints	Minimum $C_l$
	Minimum $C_{m_{c/4}}$
	Cavitation Check

**Table 2: Geometrical and aerodynamic constraints.**

### **3.3.1 Geometrical Constraints**

About geometrical constraints, it is possible to prescribe limits both on the airfoil's maximum thickness and the minimum thickness.

It is also possible to prescribe a lower bound for the minimum gap; this constraint is very important for two reasons. First of all, by using this constraint it is possible to prevent the case in which, during the design process, there is an inversion between upper and lower surface that is clearly an absurd from the practical point of view. By using this constraint it is also possible to take into account limitations connected with the material used for the manufacture of the airfoil (i.e. the minimum thickness needed for correct placement of fibre and epoxy matrix in composite materials to guarantee the necessary strength).

In order to take into account the presence of the fuel tank or the strut inside the wing, it is possible to assign a minimum thickness at a specific location along the chord. In this way it is also possible to take into account structural problems and weight limitations.

One of the advantages of the Bezier parameterization is that there is a direct connection between mathematical description and airfoil geometry. This means that it is possible to manage the geometrical limitations directly by correctly and carefully prescribing modification ranges for control points. By explicitly assigning geometrical constraints, the main advantage is that the designer can set the degrees of freedom in an easier way without strict limitations.

### **3.3.2 Aerodynamic Constraints**

It can be not difficult to manage the geometrical constraints by properly setting the degrees of freedom and avoid to use the

use of explicit constraints. In the case of aerodynamic constraints it is more difficult to do.

Both constraints on lift coefficient and moment coefficient have been implemented. Specially for aeronautical applications the opportunity to control the moment coefficient can be useful.

If we consider the airfoil as part of an airplane, the constraint on the moment coefficient allows the designer to take into account the trim drag of the horizontal plan and, indirectly, the weight of the airplane's tail zone. This is due to the fact that, in order to balance an airfoil with a high negative pitching moment, stronger equilibrium capabilities will be required to the horizontal plan; it means that it will be necessary to increase the surface of horizontal plan and/or the distance from the wing and, in this way, the structural weight will be increased.

For marine applications, the cavitation phenomenon play an important role. Cavitation is defined as the phenomenon of formation of vapor bubbles of a flowing liquid in a region where the pressure of the liquid falls below its vapor pressure. If cavitation occurs on a blade, it can lead to the corrosion of the blade.

The parameter that controls the cavitation is the *cavitation parameter*  $\sigma_v$ , defined as:

$$\sigma_v = \frac{p_v - p_0}{q} \quad \text{eq 9}$$

Where:

$q$  is the dynamic pressure,  $p_v$  is the vapour pressure and  $p_0$  is the static pressure.

In this work a special constraint takes into account the presence of cavitation and allows the designer to avoid that cavitation occurs for the prescribed design asset.

### 3.4 Objective Function Evaluation

In order to obtain an efficient optimization process, the problem regarding the evaluation of objective function and aerodynamic constraints cannot be neglected.

In this context, efficiency of the optimization process means that the airfoil's aerodynamic characteristics predicted during the process should be as accurate and realistic as possible; this is because the optimum searching process is an iterative process in which each adjustment along the way depends on the values predicted in each step. If these values are not consistent with the physics of the problem in exam, the final result will be meaningless.

A practical example of these concepts can be the development of high lift airfoil. If an inviscid solver is used, the separation phenomenon will not be taken into account and the final geometry will be not realistic.

One of advantages of numerical optimization is that, if an external code is used, this code will be used in direct mode (the geometry is prescribed and its aerodynamics is calculated); this means that, in principle, every software, both commercial or in house developed, can be integrated.

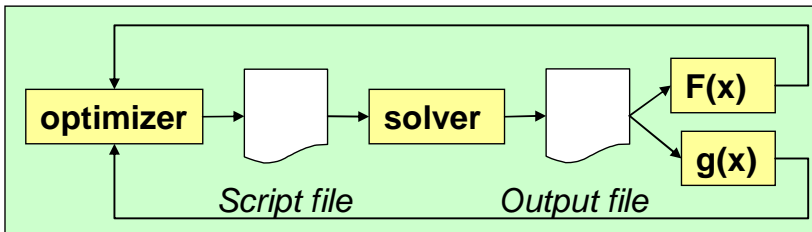


Fig. 16 Optimizer-solver connection scheme.

The only limitation is connected with the communication needs between the aerodynamic solver and the optimizer. In order to preserve the autonomous characteristics of the optimization process, this communication should be necessarily in remote way, through script files usage (Fig. 16).

So, integration means first of all establishing and managing of these communications, also providing special checks to increase the general robustness of the process.

In the present research, three existing numerical codes have been integrated to evaluate both objective function and aerodynamic constraints: XFOIL<sup>8</sup>, MSES<sup>9,10</sup> and the in house developed TBVOR<sup>11,12,13</sup>.

### ***3.5 Numerical Examples***

By implementing the concepts explained in the previous paragraphs, a new numerical code, named Optfoil, has been developed and illustrated in Appendix B of the present work.

In this section, several practical examples are provided to demonstrate the potentialities of the numerical optimization applied to the airfoil design problem. In each sub-section the design of a particular airfoil to satisfy specific requirements is illustrated; for each case time histories and other details regarding the optimization process are provided.

Both single-objective and multi-objective cases are shown. In most of these tests the initial geometry (baseline) is the NACA0012 airfoil; this choice is due to the fact that one of the goals of these tests is to demonstrate that it is not mandatory to use an initial configuration close to the expected optimum. The NACA0012 airfoil is not designed for high lift, high efficiency or low drag applications, but, despite of this, very good results have been obtained. All the proposed examples are performed on a Intel Centrino CPU@1.7Ghz.

### 3.5.1 High Lift Airfoil – Single Point Approach

The aim of this test is to develop an airfoil for high lift needs; a classical example of this class of airfoils is the S1223 airfoil designed by Selig<sup>14,15</sup>.

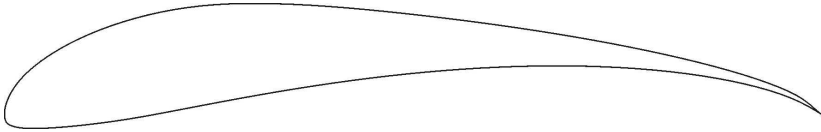


**Fig. 17 S1223 airfoil.**

The baseline for this test is the NACA0012 airfoil; the objective is to maximize the lift coefficient at angle of attack equal to  $10^\circ$ , with Reynolds number equal to 200000 and free transition. Table 3 summarizes these data.

Obj1	Reynolds Number:	200000
Max Cl	Mach:	0
	Transition:	free
	Prescribed Asset:	$\alpha=10^\circ$

**Table 3: Design parameters.**

Fourteen degrees of freedom are used (Fig. 18); the constraints are a thickness between 12% and 12.5% referred to the airfoil chord and the minimum gap positive.

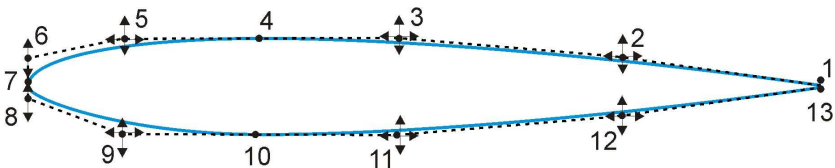


**Fig. 18 NACA0012 baseline and location of degrees of freedom.**

XFOil numerical code is used to evaluate the aerodynamic performances of the airfoil.

Fig. 19 shows the history of the objective function and Fig. 20 shows the configuration out of trend indicated as “A”

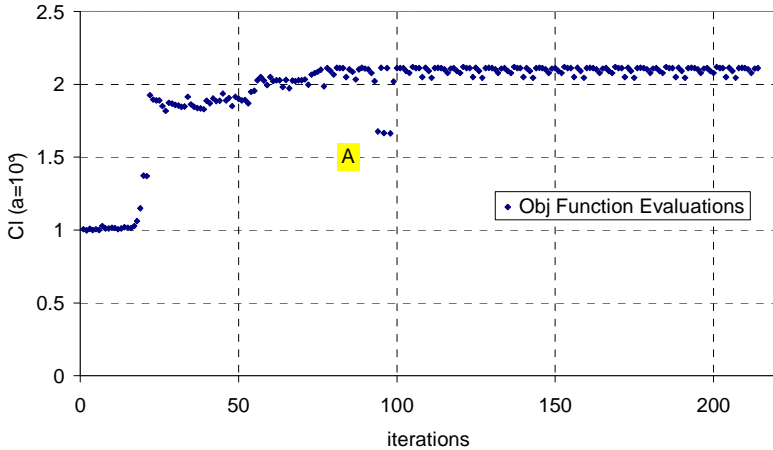


**Fig. 19 Objective Function History.**



**Fig. 20 Configuration "A".**

In Table 4, the initial and the final values of objective function are shown with the information about the elapsed time.

Objective Function		Elapsed time (sec)	Obj Func Eval.
Initial Value	Final Value		
1.01	2.11	96	214

**Table 4: Optimization results.**



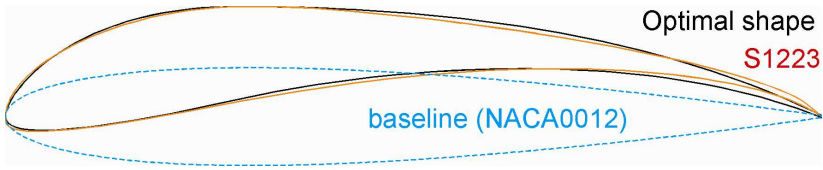


**Fig. 21 Comparison between the baseline, the final geometry and the S1223 airfoil.**

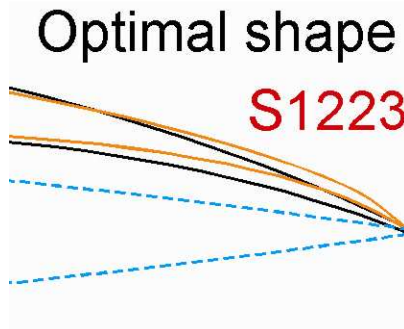


**Fig. 22 Comparison between the baseline, the final geometry and the S1223 airfoil; trailing edge zone detail.**

The optimal configuration is compared with the baseline and the S1223 geometry (Fig. 21); a comparative numerical analysis in design conditions, between the S1223 and the final geometry, has been performed by using XFOil. The lift coefficient of S1223 is slightly higher but the minimum drag coefficient of the optimal configuration is lower.

	S1223	Optimal Shape
$C_l (\alpha=10^\circ)$	2.18	2.11
$C_{d_{\min}}$	0.0168	0.0144

Starting from a NACA0012, an airfoil for high lift applications, very similar to the S1223 in a very short time it has been designed.

### 3.5.2 High Aerodynamic Efficiency Airfoil

In wind turbine and tidal turbine applications, high aerodynamic efficiency ( $L/D$ ) airfoils are required.

In this paragraph, the design of a high efficiency airfoil is proposed; in particular, both single point and dual points approaches are used. In this way, one of the possible sources of error by using numerical optimization approach is illustrated and the solution is explained.

In this case the baseline is the G1 airfoil and fourteen degrees of freedom are used (Fig. 23); Table 5 shows the design conditions. In this case a minimum thickness of 14% is prescribed and no cavitation should occur.

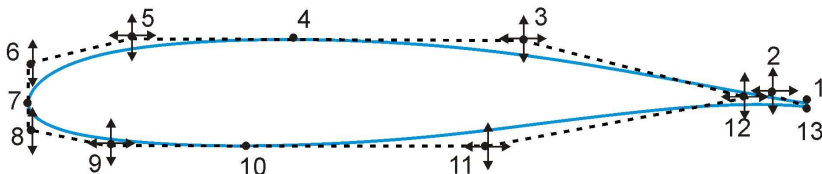


Fig. 23 G1 airfoil and used degrees of freedom.

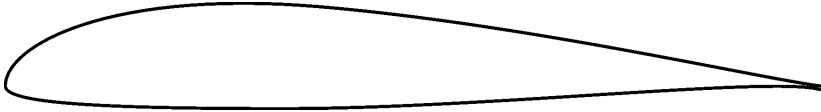
Initial Airfoil:	G1
Reynolds Number:	500000.
Mach:	0.
Transition:	free
Prescribed Asset:	$Cl = 1.1$

Table 5: Design conditions.

#### 3.5.2.1 Single Point Approach

Two geometries have been designed by using the same number of degrees of freedom but different ranges of variation.

The final geometries are shown in the following figures and a comparison in terms of aerodynamic efficiency curves is illustrated in Fig. 27.



**Fig. 24 Optimal shape 1.**

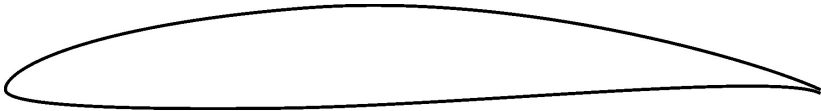


**Fig. 25 Optimal shape 2.**



**Fig. 26 GT1 airfoil.**

Objective Function: Aerodynamic Efficiency	Initial Value	Final Value	
		Optimal shape1	Optimal shape2
	69.4	102.3	133.7
Elapsed time (sec):		36	54
Objective eval. calls:		98	178

**Table 6: Optimization results.**

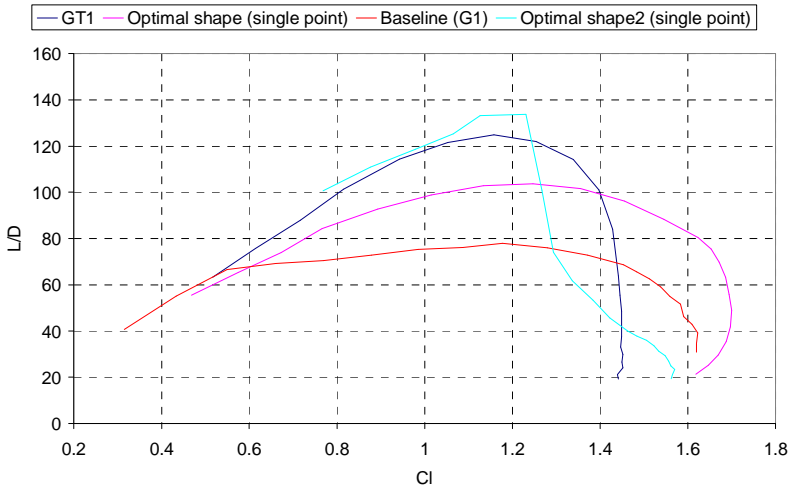


**Fig. 27 Comparison between aerodynamic efficiency of geometries.**

In both two cases, the final geometry represents a sensible enhancement compared with the initial configuration.

In Fig. 27 there is also the aerodynamic efficiency curve of another airfoil, named GT1. This airfoil has been designed with the same requirements, but the inverse design technique has been applied. By comparing the GT1 airfoil with the two solutions, the optimal shape1 is not good as the GT1, the optimal shape2 is better than GT1, but just in correspondence of design conditions. In off-design conditions, the GT1 airfoil is preferable.

This example leads to an important conclusion; specially when drag coefficient is used as objective function, the results of numerical optimization are optimal just in the prescribed configuration. Out of these conditions, nothing can ensure that the characteristics are optimal again.

On one hand this is consistent with the formulation of the problem because we ask the optimizer to take into account a

specific set of conditions and constraints; we should expect that the solution is optimal just in these conditions.

On the other hand, in general, an airfoil will work also in off-design conditions; so it can be preferable a solution “good” (i.e. GT1) in a wide range of operative conditions instead of one “optimal” (i.e. optimal shape2) just in a specific operative condition.

In order to fix this problem in our approach, some conceptual correction should be add to our formulation; this can be done by applying a dual point approach or, more in general, a multi-point approach.

### 3.5.2.2 Multi Point Approach

The main difference between single-point and multi-point optimization is that several objective functions and/or several sets of design conditions are taken into account at same time.

From the practical point of view, this approach is more realistic because in real design problems more than one design condition or objective function are involved; often these objective functions are in contrast each one with each other.

This means that, in general, it doesn't exists just one optimal solution, but a “family” of optimal solutions; each one corresponding to a particular compromise between design conditions.

The most popular way to combine together different objective functions, is a weighted linear combination of single objectives. Formerly, the problem is solved as a single objective problem; for a bi-objective problem:

$$F(X) = kf_1 + (1 - k)f_2 \quad \text{eq 10}$$

Where  $f_1$  and  $f_2$  are the single objective functions and  $k$  is a parameter between 0 and 1.

Table 7 summarizes the design conditions of interest; basically, a operative region is specified.

Obj1	Reynolds Number:	500000
Max: L/D	Mach:	0
	Transition:	free
	Prescribed Asset:	Cl=0.8
Obj2	Reynolds Number:	500000
Max: L/D	Mach:	0
	Transition:	free
	Prescribed Asset:	Cl=1.3

**Table 7: Design parameters.**

By using the same baseline of single point approach, several values of k parameter have been used to take into account different compromise conditions (Table 8).

k	L/D (Cl=0.8)	L/D (Cl=1.3)	Obj Eval.*	Elaps. time (sec)
0	89	134	166	132
0.25	96	130	227	184
0.4	96	126	127	90
0.5	96.4	125	154	107
0.6	91.8	130.6	142	121
0.75	110	80	138	107
1	114	72.6	108	85
Overall time	826 sec (14min)			
Overall calls	1062 *			
* The effective XFoil calls number is double				

**Table 8: Optimization results.**

Some of the optimal geometries are represented in the following figures.



**Fig. 28 Optimal geometry;  $k=0.25$ .**

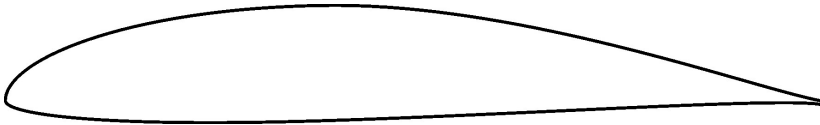


**Fig. 29 Optimal geometry;  $k=0.4$ .**

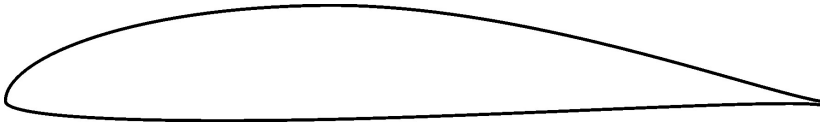


**Fig. 30 Optimal geometry;  $k=0.5$ .**

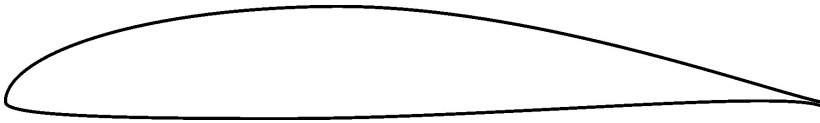


**Fig. 31 Optimal geometry;  $k=0.6$ .**

By representing all these partial solutions in the same graph, it is possible to build the Pareto frontier. In the most general case, the Pareto frontier is the hyper-surface generated by the solutions of partial optimization problems. In dual point problems the Pareto frontier is a curve in the plan (Fig. 32).

Both looking at Fig. 32 and Fig. 33, it is evident that several geometries have been obtained with good characteristics as the GT1 airfoil; the advantage in usage of numerical optimization approach is the time spent to obtain the geometries. By using the inverse design approach, around a couple of hours have been necessary, instead of 14 minutes, to design the GT1 airfoil. More details about the GT1 airfoil design are available in Appendix A.

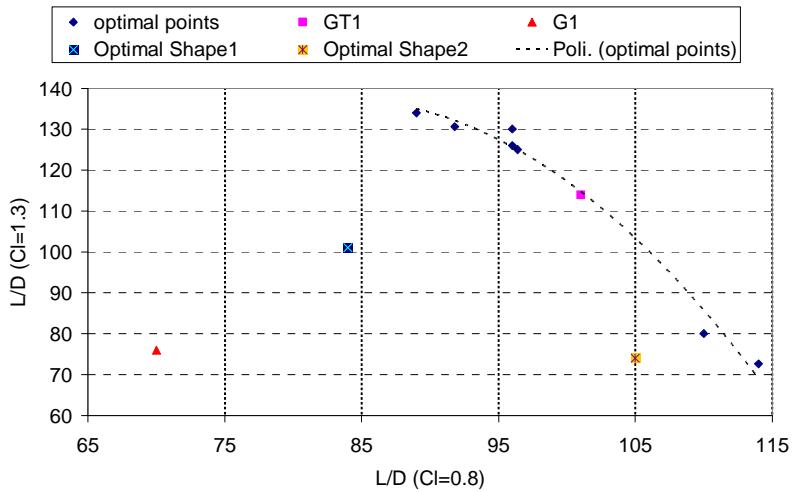


**Fig. 32 Pareto frontier.**

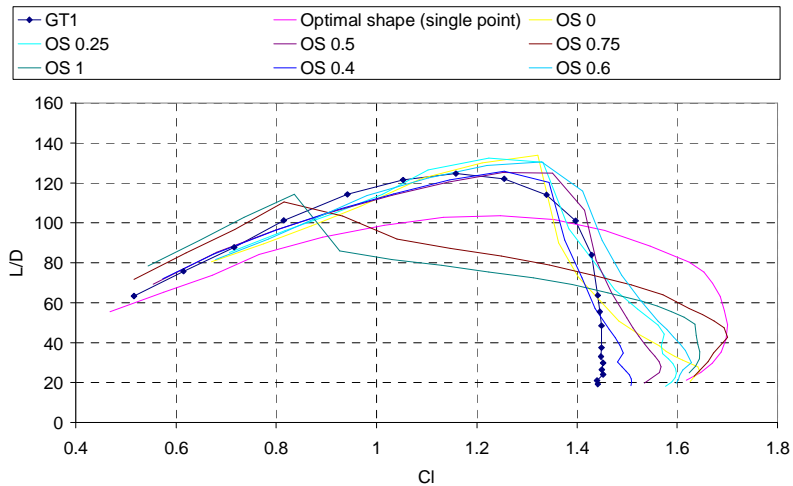


**Fig. 33 Aerodynamic efficiency curve; comparison between different solutions.**



### 3.5.3 High Endurance Airfoil for Sailplanes – Dual Point Approach

An example of this class of airfoils is the SM701 airfoil developed by Selig and Maughmer<sup>16</sup>. The requirements for this airfoil are in Table 9 and have been used as design conditions.

Obj1	Reynolds Number:	3000000
Min: Cd	Mach:	0
	Transition:	free
	Prescribed Asset:	Cl=0.2
Obj2	Reynolds Number:	1500000
Min: Cd	Mach:	0
	Transition:	free
	Prescribed Asset:	Cl=1.5

**Table 9: Design parameters.**

It is required an airfoil that minimizes the drag coefficient at same time in cruise condition ( $Cl=0.2$ ) and in high lift condition ( $Cl=1.5$ ). By using the dual point approach, it is necessary to minimize an objective function  $F$  given by eq.10.

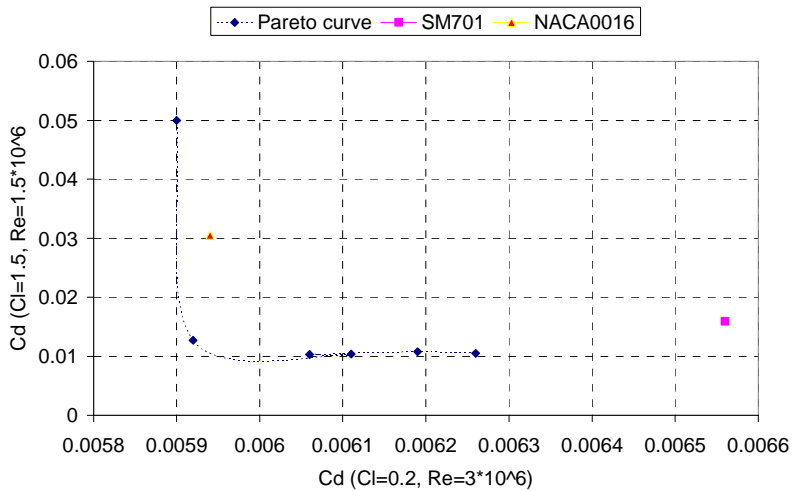
The baseline is the NACA0012 and fourteen degrees of freedom are used. The airfoil thickness should be greater than 16% of the chord and the moment coefficient should be greater than -0.1 in order to limit the trim drag.

Table 10 shows the results for several values of  $k$  weight factor. The Pareto frontier is illustrated in Fig. 34; in the same figure the reference airfoil SM701 is indicated. As we can see, all the designed geometries are dominant compared with SM701 and they have been obtained after a very competitive overall time equal to 42 minutes.

Some of these geometries are shown and the geometry for  $k=0.6$  and the SM701 are compared.

k	Cd (Cl=0.2)	Cd (Cl=1.5)	Obj Func. Eval	Elapsed Time (sec)
0.3	0.00626	0.0105	293	462
0.5	0.00619	0.0108	222	656
0.55	0.00611	0.0104	311	823
0.6	0.00592	0.01273	127	431
0.7	0.0059	0.05	150	123
elapsed time (min)				42
Total Obj Func evaluations			1103	
* the effective Xfoil calls number is double				

**Table 10: Optimization results for several values of k parameter.**



**Fig. 34 Pareto frontier.**

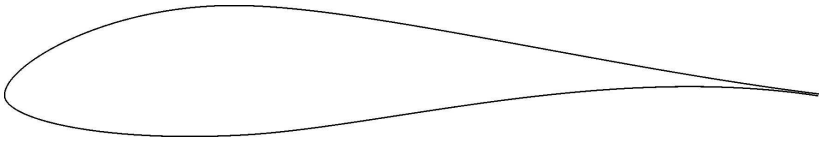


**Fig. 35 Final geometry;  $k=0.3$ .**

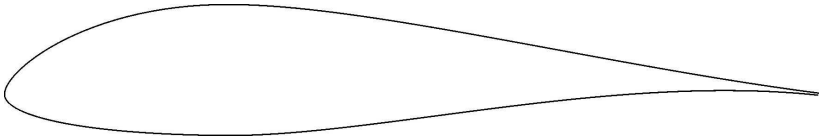


**Fig. 36 Final geometry:  $k=0.5$ .**

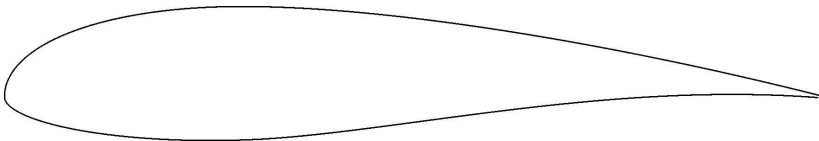


**Fig. 37 Final geometry:  $k=0.6$ .**

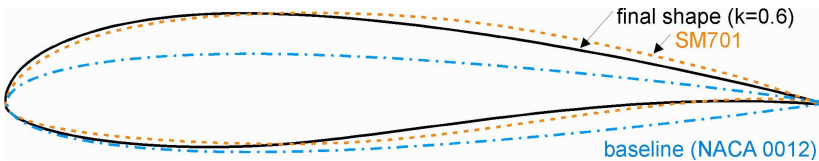


**Fig. 38 Comparison between baseline, final geometry ( $k=0.6$ ) and SM701.**

One of the constraints indicated by Selig and Maughmer is the limit on the moment coefficient; each designed airfoil respects the prescribed value. This doesn't happen for the SM701; its moment coefficient is around -0.12, but the authors accept this fact because the SM701 respects the rest of requirements. By using the numerical optimization approach, it is possible to obtain several geometries respecting the complete set of constraints in a competitive time.

### 3.5.4 Low-Drag Airfoil – Dual Point Approach

In this case, the objective of the test is to minimize of the drag coefficient in two different conditions, in order to obtain a low drag airfoil with the characteristic low-drag pocket in the polar curve.

The baseline is the NACA0012 and fourteen degrees of freedom are used (Fig. 18); in this case the only constraint is the airfoil thickness not less than 12% of the chord. In Table 11 the design conditions are indicated.

Obj1 Min: Cd	Reynolds Number:	1000000.
	Mach:	0.
	Transition:	free
	Prescribed Asset:	Cl=0.2
Obj2 Min: Cd	Reynolds Number:	1000000.
	Mach:	0.
	Transition:	free
	Prescribed Asset:	Cl=0.6

**Table 11: Design parameters.**

k	Cd (Cl=0.2)	Cd (Cl=0.6)	function calls	elapsed time (min)
0.2	0.00556	0.00499	447	6.8
0.3	0.00541	0.00495	457	7.5
0.5	0.00484	0.00535	368	5.1
0.6	0.00464	0.00582	306	5.05
0.8	0.00456	0.00674	430	6.85
1	0.00457	0.00914	182	2.95
total elapsed time (min):			34	
total function calls:			2190	

**Table 12: Optimization results.**

In this case too, several values of  $k$  parameters have been used; the results of the optimization process are shown in Table 12. The calculated Pareto frontier is shown in Fig. 39.

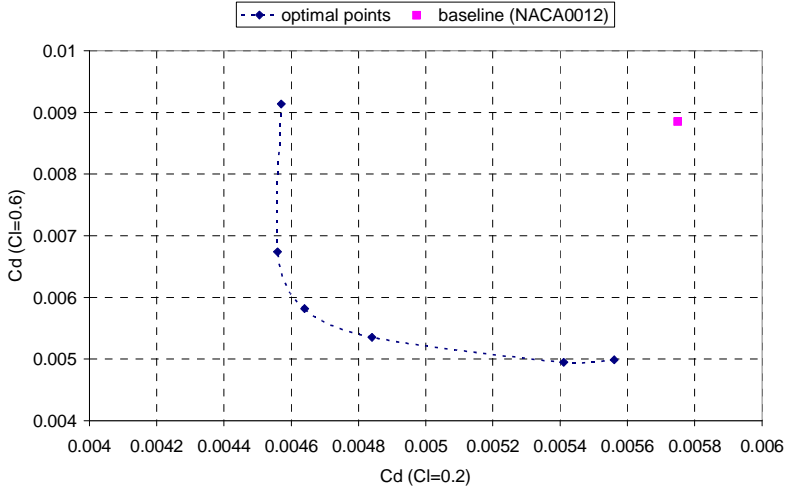


**Fig. 39 Pareto frontier.**

Some of the obtained geometries are shown in the following figures.



**Fig. 40 Final geometry;  $k=0.2$ .**

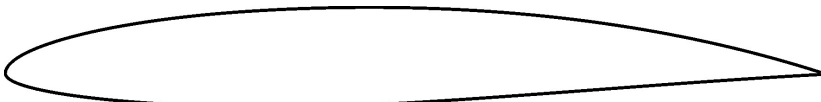


**Fig. 41 Final geometry;  $k=0.3$ .**

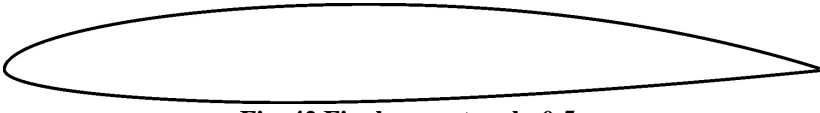


**Fig. 42 Final geometry; k=0.5.**

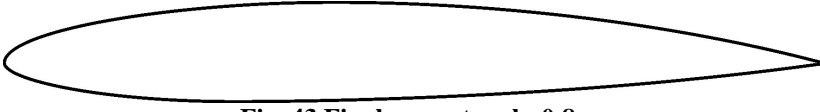


**Fig. 43 Final geometry; k=0.8.**

A comparison between these geometries in terms of drag polar curve is illustrated in Fig. 44.

In each curve there is the characteristic low-drag pocket as required; by modifying the  $k$  parameter it is possible to finely tune the shape of the polar curve.

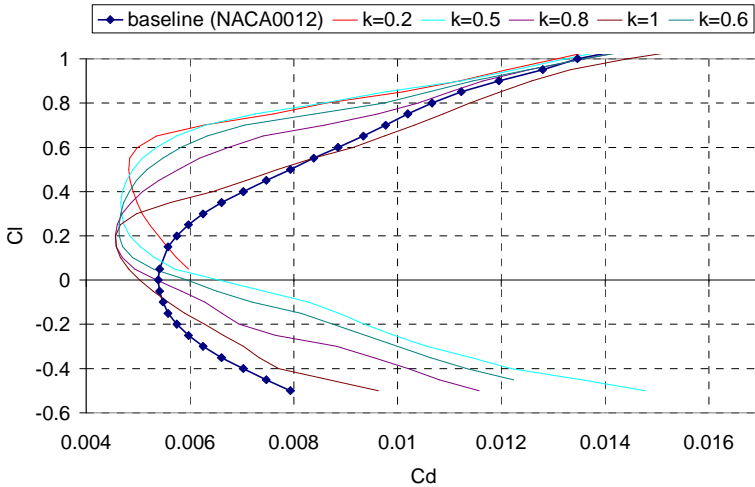


**Fig. 44 Comparison between drag polar curves.**

### 3.5.5 Airfoil for a S.T.O.L. High-Speed Ultra-Light Aircraft – Dual Point Approach

The last case study is the design of an airfoil installed on a ultra-light aircraft made in composite materials with high cruise speed and S.T.O.L. performances. We need an airfoil with good drag coefficient characteristics in cruise configuration and good high lift performances; Table 13 summarizes the design conditions.

Obj1 Min: Cd	Reynolds Number:	4000000.
	Mach:	0.
	Transition:	free
	Prescribed Asset:	Cl=0.2
Obj2 Max: Cl	Reynolds Number:	1000000.
	Mach:	0.
	Transition:	free
	Prescribed Asset:	$\alpha=10^\circ$

**Table 13: Design conditions.**

In this case three constraints are used.

First of all, a minimum thickness of 13.5% referred to the chord is imposed.

Then a minimum gap not less than 0.2% of the chord is used; this constraint is a consequence of the need of composite materials usage, in order to ensure a minimum thickness for the correct positioning of composites and guarantee the necessary structural strength.

The third limitation is prescribed on the minimum moment coefficient: it should be greater than -0.035. In this way, it is possible to take into account the trim drag of the horizontal plan and, indirectly, the weight of the airplane's tail zone.

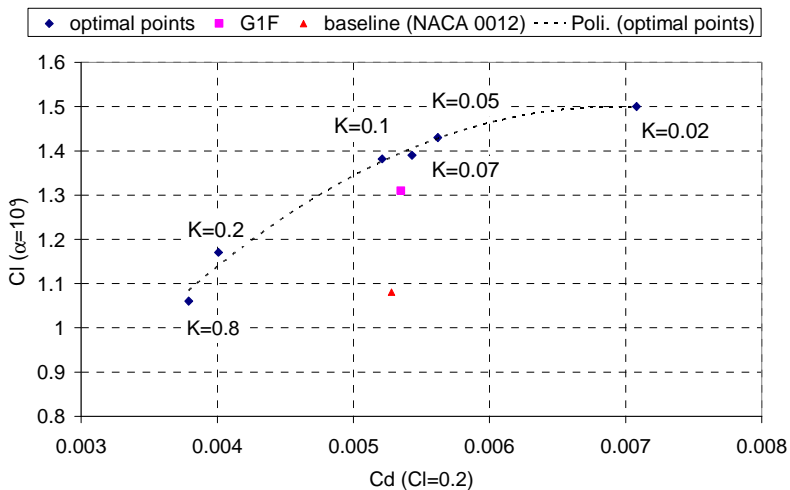
The baseline is the NACA0012 airfoil and fourteen degrees of freedom are used.

Table 14 shows the results for different values of  $k$  parameter.

k	Cd (Cl=0.2)	Cl ( $\alpha=10^\circ$ )	elapsed time (sec)	Obj Func eval*
0.02	0.00708	1.5	299	240
0.05	0.00562	1.43	298	235
0.07	0.00543	1.39	210	198
0.1	0.00521	1.382	234	210
0.2	0.00401	1.17	274	285
0.8	0.00379	1.06	204	190
total elapsed time (min)			25	
total obj func. Eval*			1358	

**Table 14: Optimization results.**

Some of the optimal geometries and the Pareto frontier are illustrated in the following figures.



**Fig. 45 Pareto frontier.**





**Fig. 46 Optimal geometry;  $k=0.02$ .**



**Fig. 47 Optimal geometry;  $k=0.05$ .**



**Fig. 48 Optimal geometry;  $k=0.07$ .**



**Fig. 49 Optimal geometry;  $k=0.1$ .**



**Fig. 50 Optimal geometry;  $k=0.8$ .**

In the plot of Pareto frontier, also the point referred to the G1F airfoil is present (Fig. 51); this airfoil has been developed with the same set of constraints, but by using the inverse design approach. As we can see, the optimal geometry for  $k=0.1$  is dominant compared with the G1F airfoil. More details about the G1F airfoil are available in Appendix A.

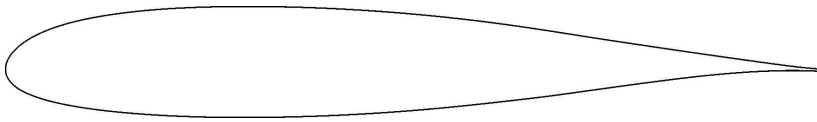


**Fig. 51 G1F airfoil.**

### **3.5.6 Multi-Element Airfoil; Gap and Overlap Optimization**

In the previous cases the airfoil's shape has been optimized. In this test the position between elements is modified to maximize the lift coefficient of the configuration at Reynolds number equal to 1000000, angle of attack equal to  $14^\circ$  and free transition.

The baseline is the 30P30N (LB546A in McDonnell Douglas nomenclature) three component airfoil, one of the most popular multi-component configurations because of its use as CFD test case.

The solver used during the optimization process is MSES. In this code just one sharp point is allowed per element; for this reason the geometry has been slightly modified in the cove zone. The lift curve at Reynolds number equal to  $9 \cdot 10^6$  has been calculated and compared with experimental data; no differences have been recognized due to this modification.

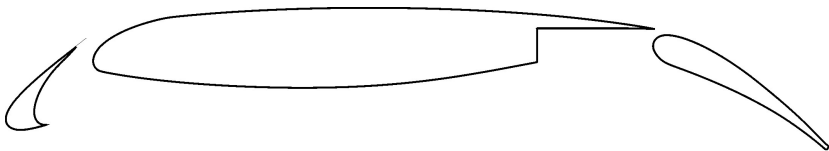


**Fig. 52 30P30N airfoil.**



**Fig. 53 Modified 30P30N airfoil.**

Other minor modifications have been done to the set of coordinates of the airfoil because of internal MSES features. The total number of has been reduced from 500 and more points per element, to 141 points per element and an extra point has been added to the slat and the main component in correspondence of the cove.

In Fig. 54 the initial configuration and the final one are compared; in Table 15 the evolution in terms of degrees of freedom and objective function are indicated. Compared with the previous examples, the elapsed time is quite long; this is due to the MSES numerical code. In fact in this case, for each iteration, in order to guarantee the numerical stability of the code, it is necessary to perform not just the analysis at  $14^\circ$  but all the angles of attack until  $14^\circ$ .

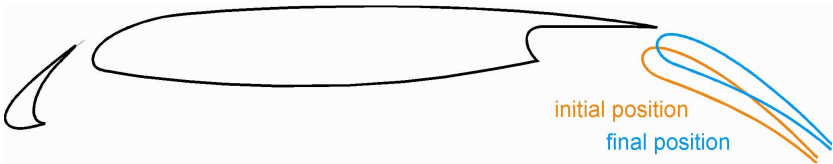


**Fig. 54 Comparison between initial and final configuration.**

	Initial Value	Final Value
Gap (%c)	2.75	1.50
Overlap (%c)	2.00	0
Cl ( $\alpha=14^\circ$ )	3.36	3.57
Elapsed time	8hr	

**Table 15: Evolution of degrees of freedom and objective function during the optimization process.**

Fig. 55 shows the objective function's time history.

In order to validate the numerical results, these ones have been compared with experimental results of Landman and Britcher<sup>17</sup>. In their publication the same airfoil is experimentally optimized; Fig. 56 shows the superimposition between numerical and experimental data. The numerical values predicted by MSES are overestimated but the trend is consistent with the experimental results.

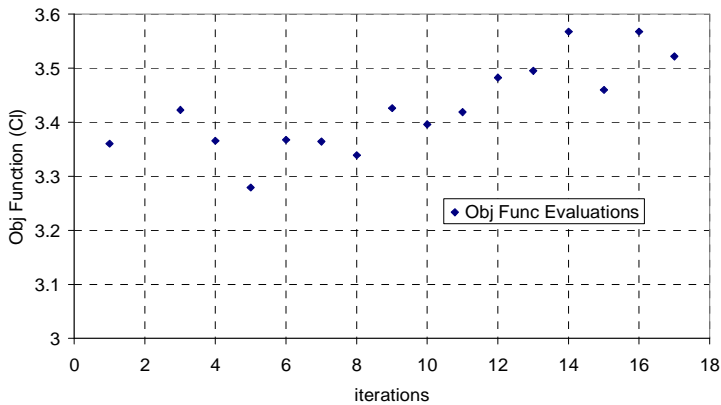


Fig. 55 Objective function time history.

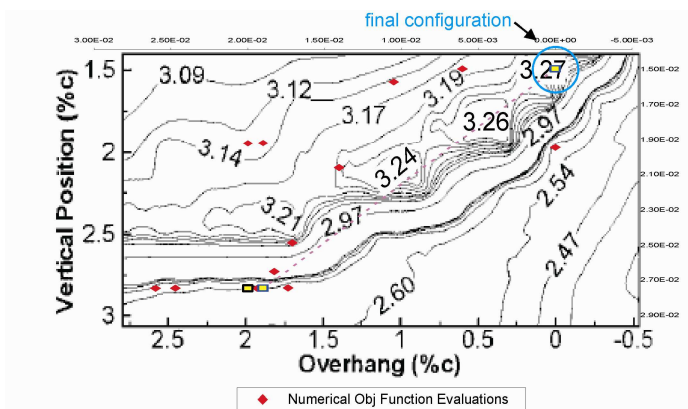


Fig. 56 Lift coefficient map; comparison between numerical and experimental data.

### **3.6 Different Approaches Comparison**

One of the most popular techniques to design airfoils is the inverse design technique, proposed by Lighthill, widely developed by Eppler<sup>18,19</sup> and Drela<sup>8</sup> and implemented also in “MDES” and “QDES” tools of XFOIL code.

The basic principle of this design method is that, the pressure coefficient on the airfoil surface is prescribed and the airfoil geometry is created; in this way the designer can generate a geometry of an airfoil that fits specific requirements by iteratively modifying the pressure distribution on the airfoil surface.

Despite of its large usage, by using this technique, there are several disadvantages in the following areas:

- User’s knowledge
- Optimum condition
- Aerodynamic solver limitations
- Autonomous process

#### **3.6.1 User’s Knowledge**

In order to reach good results, a strong background in aerodynamics and airfoil design is required. This is due to the fact that, it is necessary to edit the pressure distribution to obtain the geometry of an airfoil with specific aerodynamic characteristics; this means that the user should know how and how much to edit the pressure distribution.

By using numerical optimization approach, knowledge in aerodynamics and airfoil design is necessary of course, but just to properly set the design variables and the constraints; the

final shape and the characteristics of the pressure distribution are a consequence of the aerodynamic requirements.

### **3.6.2 Optimum Condition**

In numerical optimization approach, mathematical conditions to recognize if the optimum is reached are provided. This means that the final configuration of a design problem is at least a local optimum.

By using the inverse design approach there is not a standard criterion to establish if the optimum is obtained or not; it is just the user's experience to help deciding if a satisfying configuration has been reached. In general, the final configuration won't be an optimal solution, but a satisfying solution in the sense that probably it can be again enhanced if more time is spent.

### **3.6.3 Aerodynamic Solver Limitations**

One of the most interesting aspects of using numerical optimization approach is that it is possible to integrate in the design process every aerodynamic solver, both commercial or in house developed numerical codes. Just it is necessary the code is remotely drivable and the results are available in some output file. This is because the solver is used in direct mode: the geometry is assigned and the aerodynamic characteristics are calculated.

In inverse design approach the solver is used inverse mode: the pressure distribution is prescribed and the geometry is calculated. This means that just codes "compatible" with the inverse formulation can be used.

Most of inverse design tools are non viscous; this means that, for each iteration, the user needs to verify, by using the solver in direct mode analysis, the real effect of pressure distribution modification when viscous effects are active.

Another consequence of this aspect is that, by applying inverse design approach, there is no way to take into account (in the pressure modification phase) other parameters regarding for example overall aircraft performances or cost factors, but just airfoil's aerodynamic parameters.

If the numerical optimization is used, it is possible to choice as objective function some parameters very “far” from the airfoil aerodynamics (i.e. the fuel consumption).

### **3.6.4 Autonomous Process**

Another disadvantage of inverse design technique is that the designer is actively involved during all the design process.

In numerical optimization approach, the user is involved during the input phase (this step is very important because the final result will be the consequence of initial settings), but not during the process. This allows the designer to stay focused on the main aerodynamic problem and not on the numerical one, and allows to maximize the advantages of using more computational resources.





## Chapter 4

# Lifting Surfaces Design and Optimization

### ***4.1 Introduction***

In the same way as done in the previous chapter, the aim of this chapter is to apply the numerical optimization approach to design and optimize lifting surfaces.

In this case however, the research's focus has been pointed on the development of a new aerodynamic solver, ad hoc suited for its integration and easy usage in a numerical optimization process.

In the next section, the development of this numerical code, named VWING, and the extensive validation tests are illustrated. In the same section, several improvements added to the original formulation and the relative validation tests are widely described.

In the last section of this chapter several numerical optimization examples are proposed.

### ***4.2 VWING Numerical Code***

#### **4.2.1 Overview**

VWING is a numerical code for aerodynamic analysis of lifting surfaces, based on the Prandtl's lifting line theory.

Actually, instead of the classical formulation, a new generalized mathematical formulation, proposed by

Phillips<sup>24,25</sup>, has been implemented. Despite of its increased complexity compared with the original one, by using this formulation, a very versatile numerical code has been developed.

Some of the major features are here summarized:

- Analysis of multi-body configurations
- Airfoil's viscous characteristics taken into account
- Analysis of non planar and non conventional configurations
- Analysis in presence of angular velocities
- Analysis in stall and post-stall conditions
- Mutual inductions calculation (downwash, upwash)
- Aerodynamic and stability derivatives calculation
- Both free wake and fixed wake models implemented

#### **4.2.2 The Mathematical Formulation**

In what is commonly referred to as the numerical lifting-line method (e.g., Katz and Plotkin<sup>21</sup>), a finite wing is synthesized using a composite of horseshoe shaped vortices.

The continuous distribution of bound vorticity over the surface of the wing, as well as the continuous distribution of free vorticity in the trailing vortex sheet, is approximated by a finite number of discrete horseshoe vortices, as shown in Fig. 57.

The bound portion of each horseshoe vortex is placed coincident with the wing quarter-chord line and is, thus, aligned with the local sweep and dihedral. The trailing portion of each horseshoe vortex is aligned with the trailing vortex sheet. The left-hand corner of one horseshoe and the right-hand corner of the next are placed on the same nodal point.

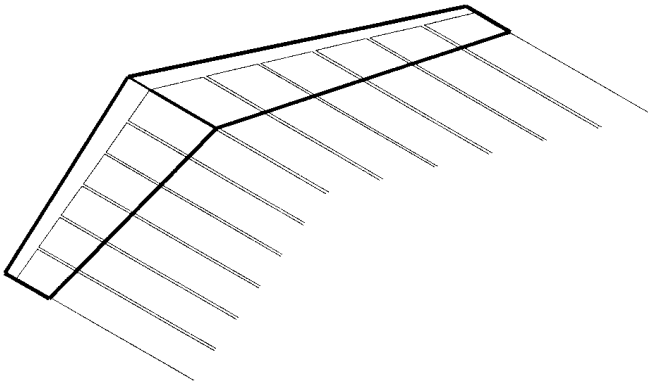


**Fig. 57 Horseshoe vortices distributed along the quarter chord of a finite wing with sweep and dihedral.**

Thus, except at the wing tips, each trailing vortex segment is coincident with another trailing segment from the adjacent vortex. If two adjacent vortices have exactly the same strength, then the two coincident trailing segments exactly cancel because one has clockwise rotation and the other has counter clockwise rotation. The net vorticity that is shed from the wing at any internal node is simply the difference in the vorticity of the two adjacent vortices that share that node.

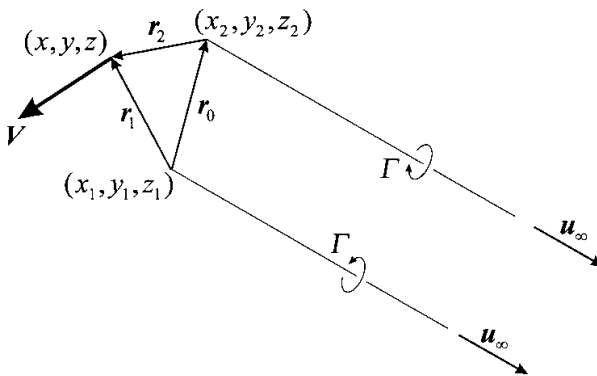


**Fig. 58 Position vectors describing the geometry for a horseshoe vortex.**

Each horseshoe vortex is composed of three straight vortex segments.

From the Biot–Savart law and the nomenclature defined in Fig. 58, the velocity vector induced at an arbitrary point in space, by any straight vortex segment, is readily found to be,

$$V = \frac{\Gamma}{4\pi} \frac{r_1 \times r_2}{|r_1 \times r_2|^2} r_0 \cdot \left( \frac{r_1}{r_2} - \frac{r_2}{r_2} \right) \quad \text{eq 11}$$

Where:

$$r_0 = r_1 - r_2, r_1 \cdot r_2 = r_1 r_2 \cos \theta, |r_1 \times r_2| = r_1 r_2 \sin \theta$$

By rearranging eq.11, it is possible to obtain:

$$V = \frac{\Gamma}{4\pi} \frac{(r_1 + r_2)(r_1 \times r_2)}{r_1 r_2 (r_1 r_2 + r_1 \cdot r_2)} \quad \text{eq 12}$$

For the finite bound segment and the two semi-infinite trailing segments shown in Fig. 58, the velocity vector induced at an arbitrary point in space, by a complete horseshoe vortex, is

$$V = \frac{\Gamma}{4\pi} \left[ \frac{u_\infty \times r_2}{r_2 (r_2 - r_2 \cdot u_\infty)} + \frac{(\bar{r}_1 + \bar{r}_2)(r_1 \times r_2)}{r_1 r_2 (r_1 r_2 + r_1 \cdot r_2)} - \frac{u_\infty \times r_1}{r_1 (r_1 - r_1 \cdot u_\infty)} \right] \quad \text{eq 13}$$

Using Prandtl's hypothesis, we assume that each span-wise wing section has a section lift equivalent to that acting on a similar section of an infinite wing with the same local angle of attack. Thus, applying the vortex lifting law to a differential segment of the lifting line

$$dF = \rho \Gamma V \times dl \quad \text{eq 14}$$

If flow over a finite lifting surface is synthesized from a uniform flow combined with horseshoe vortices placed along the quarter-chord line, from eq.13, the local velocity induced at a control point placed anywhere along the bound segment of horseshoe vortex  $j$  is

$$V_j = V_\infty + \sum_{i=1}^N \frac{\Gamma_i v_{ij}}{c_i} \quad \text{eq 15}$$

where  $v_{ij}$  is the dimensionless induced velocity:

$$v_{ij} = \begin{cases} \frac{\Gamma_i}{4\pi c_i} \left[ \frac{\frac{u_\infty \times r_{i2j}}{r_{i2j}(r_{i2j} - u_\infty \cdot r_{i2j})} + \frac{(r_{i2j} + r_{i1j})(r_{i2j} \times r_{i1j})}{r_{i1j} r_{i2j} (r_{i1j} r_{i2j} + r_{i1j} \cdot r_{i2j})}}{r_{i1j}(r_{i1j} - u_\infty \cdot r_{i1j})} \right], & i \neq j \\ \frac{\Gamma_i}{4\pi c_i} \left[ \frac{\frac{u_\infty \times r_{i2j}}{r_{i2j}(r_{i2j} - u_\infty \cdot r_{i2j})} + \frac{u_\infty \times r_{i1j}}{r_{i1j}(r_{i1j} - u_\infty \cdot r_{i1j})}}{r_{i1j}(r_{i1j} - u_\infty \cdot r_{i1j})} \right], & i = j \end{cases} \quad \text{eq 16}$$

At this point,  $\overline{c_i}$  could be any characteristic length associated with the wing section aligned with horse shoe vortex  $i$ . This

characteristic length is simply used to have eq.16 in non-dimensional form and has no effect on the induced velocity. The aerodynamic force acting on a span-wise differential section of the lifting surface located at control point  $i$  is given by:

$$dF_i = \rho \Gamma_i \left( V_\infty + \sum_{j=1}^N \frac{\Gamma_j v_{ij}}{c_j} \right) \times dl_i \quad \text{eq 17}$$

At the same time:

$$|dF_i| = \frac{1}{2} \rho V_\infty^2 Cl_i(\alpha_i, \delta_i) dA_i \quad \text{eq 18}$$

$\delta_i$  is the flap deflection angle and  $\alpha_i$  is the local angle of attack at control point  $i$ .

$$\alpha_i = \tan^{-1} \left( \frac{V_i \cdot u_{ni}}{V_i \cdot u_{ai}} \right) \quad \text{eq 19}$$

where  $u_{ai}$  and  $u_{ni}$  are, respectively, the unit vectors in the chordwise direction and the direction normal to the chord, both in the plane of the local airfoil section as shown in Fig. 59.

From eq. 17 and eq. 18:

$$2 \left( v_\infty + \sum_{j=1}^N v_{ji} G_j \right) \times \zeta_i \left| G_i - Cl_i(\alpha_i, \delta_i) = 0 \quad \text{eq 20} \right.$$

Where:

$$v_\infty = \frac{V_\infty}{V_\infty}, \zeta_i = \frac{-dl_i}{c_i dA_i}, G_i = \frac{\Gamma_i}{c_i V_\infty}$$

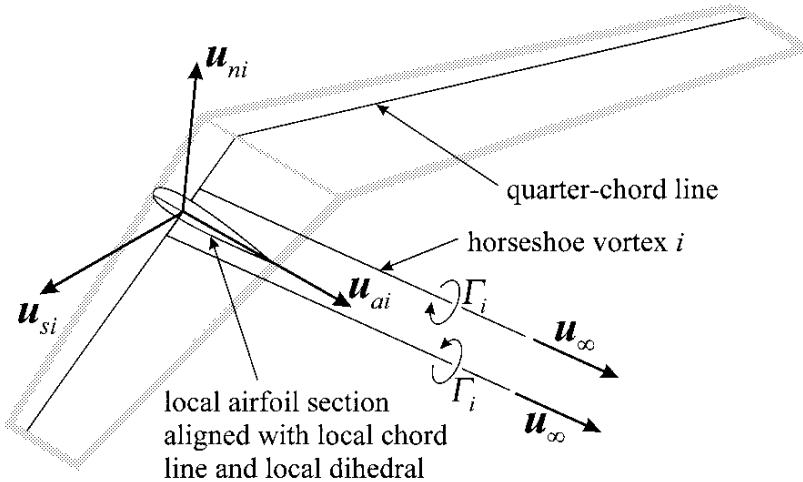


**Fig. 59 Unit vectors describing the orientation of the local airfoil section.**

Eq.20 can be written for  $N$  different control points, one associated with each of the  $N$  horseshoe vortices used to synthesize the lifting surface or system of lifting surfaces. This provides a system of  $N$  nonlinear equations relating the  $N$  unknown dimensionless vortex strengths  $G_i$  to known properties of the wing.

This system is solved by applying the Newton's method; in order to do this, the system of equations should be written in vector form:

$$Z(G) = R$$

Where:

$$Z(G) = 2 \left( v_\infty + \sum_{j=1}^N v_{ji} G_j \right) \times \zeta_i \left| G_i - Cl_i(\alpha_i, \delta_i) \right.$$

We wish to find the vector of dimensionless vortex strengths  $\mathbf{G}$  that makes all components of the residual vector  $\mathbf{R}$  go to zero. Thus, we want the change in the residual vector to be  $-\mathbf{R}$ . We start with an initial estimate for the  $\mathbf{G}$  vector and iteratively refine the estimate by applying the Newton corrector equation

$$[J]\Delta G = -R \quad \text{eq 21}$$

Where  $[J]$  is the matrix of partial derivatives.

$$J_{ij} = \begin{cases} \left[ \begin{array}{l} \frac{2w_i \cdot (v_{ij} \times \zeta_i)}{|w_i|} G_i \\ - \frac{\partial Cl_i}{\partial \alpha_i} \frac{\overline{v_{ai}} (v_{ji} \cdot u_{ni}) - \overline{v_{ni}} (v_{ji} \cdot u_{ai})}{v_{ai}^2 + v_{ni}^2} \end{array} \right], i \neq j \\ \left[ \begin{array}{l} \frac{2w_i \cdot (v_{ij} \times \zeta_i)}{|w_i|} G_i \\ - \frac{\partial Cl_i}{\partial \alpha_i} \frac{\overline{v_{ai}} (v_{ji} \cdot u_{ni}) - \overline{v_{ni}} (v_{ji} \cdot u_{ai})}{v_{ai}^2 + v_{ni}^2} \\ + 2|w_i| \end{array} \right], i = j \end{cases} \quad \text{eq 22}$$

Where:



$$w_i = (v_\infty + \sum_{j=1}^N v_{ij} G_j) \times \zeta_i$$

$$v_{ni} = (v_\infty + \sum_{j=1}^N v_{ij} G_j) \times u_{ni}$$

$$v_{ai} = (v_\infty + \sum_{j=1}^N v_{ij} G_j) \times u_{ai}$$

By combining eq.21 and eq.22 the correction vector  $\Delta G$  can be calculated; this correction vector is used to obtain an improved estimate for the dimensionless vortex strength vector  $G$  according to

$$G = G + \Omega \Delta G$$

$\Omega$  is the relaxation factor.

This process is repeated until the magnitude of the largest residual is less than the prescribed convergence factor.

## 4.2.3 Preliminary Validation Tests

### 4.2.3.1 Elliptical Wing

An elliptical wing with span equal to 5m and chord at the root equal to 1m is assigned. The numerical result predicted by using VWING is compared with the exact analytical solution in terms of span-wise distribution of aerodynamic load and lift coefficient.

One of the objectives of this first test is also to verify the accuracy of the results by varying the number of given station.

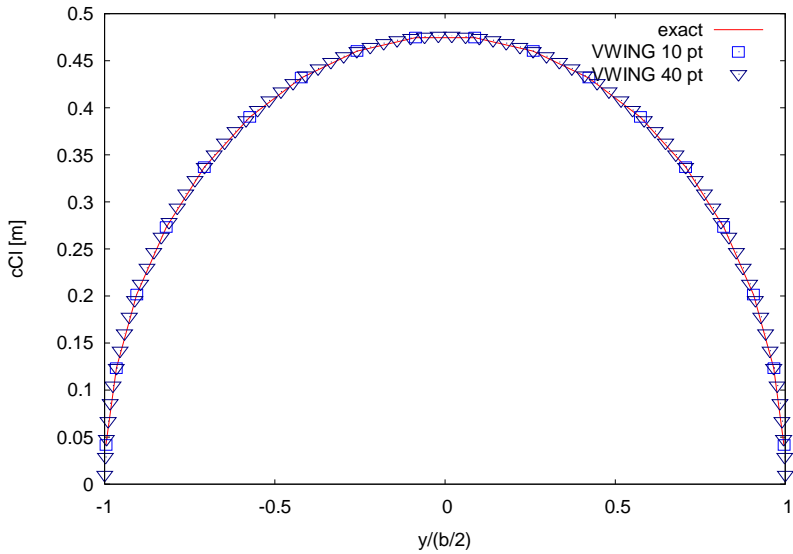


**Fig. 60** Spanwise aerodynamic load; comparison between VWING and exact solution;  $\alpha=5.71^\circ$ .

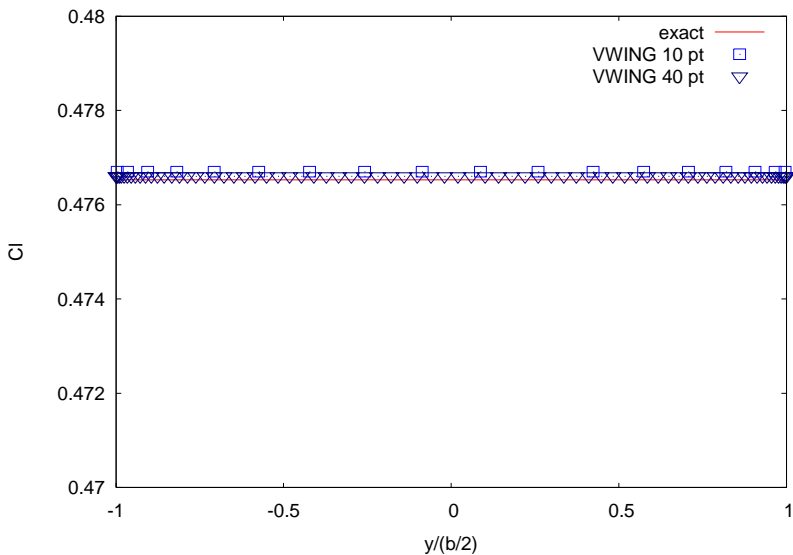


**Fig. 61** Spanwise lift coefficient; comparison between VWING and exact solution;  $\alpha=5.71^\circ$ .

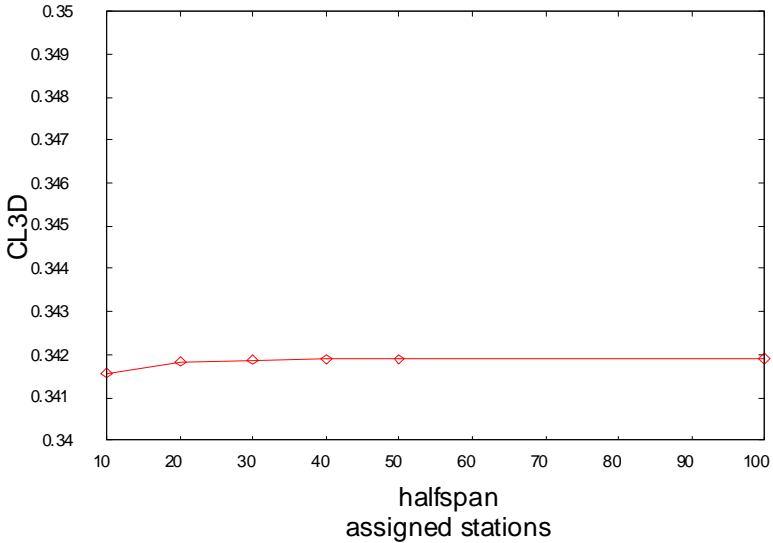


**Fig. 62** Effect of number of assigned stations in terms of lift coefficient;  $\alpha=4^\circ$ .

#### 4.2.3.2 Non Elliptical Wings

In the first case a rectangular wing is considered with span equal to 10m and chord at root equal to 1m; the comparison with the Multhopp method in terms of lift coefficient at angle of attack equal to  $5^\circ$  is shown.

In the second case a tapered wing is used as test case (Fig. 63); in this case also, the comparison is in terms of lift coefficient distribution at angle of attack equal to  $5^\circ$ .

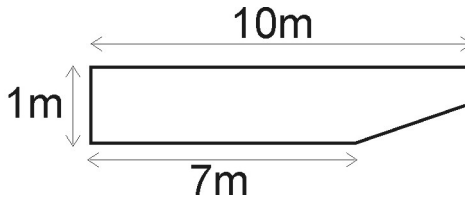


**Fig. 63** Tapered wing.

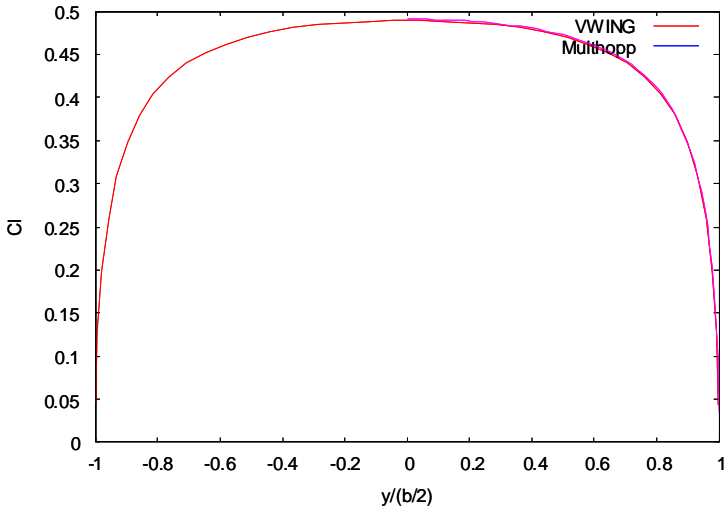


**Fig. 64 Rectangular wing - Spanwise lift coefficient distribution; comparison between VWING and Multhopp method,  $\alpha=5^\circ$ .**

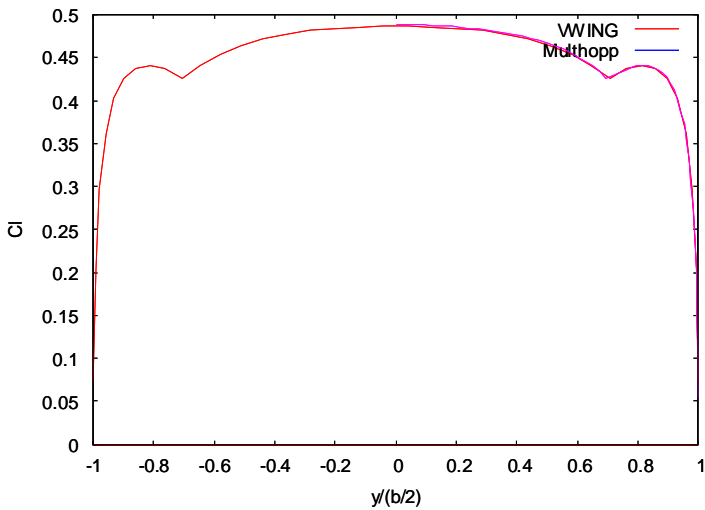


**Fig. 65 Tapered wing - Spanwise lift coefficient distribution; comparison between VWING and Multhopp method,  $\alpha=5^\circ$ .**

### 4.2.3.3 Free Wake and Fixed Wake

Both free wake and fixed wake models are implemented in VWING; in order to compare them in terms of accuracy of the solution and elapsed time, an elliptic wing with span equal to 12m and chord at root equal to 1m, is considered as test case.

With reference at the following figures and Table 16, it is evident that the free wake model is very time expensive and not compatible with an optimization process in which also a hundred of objective function evaluations are necessary.

On the other hand, this model can be used to obtain very precise results.

	free wake	fixed wake
elapsed time	5 hr	14.5 sec

**Table 16: Free wake and fixed wake; elapsed time comparison.**

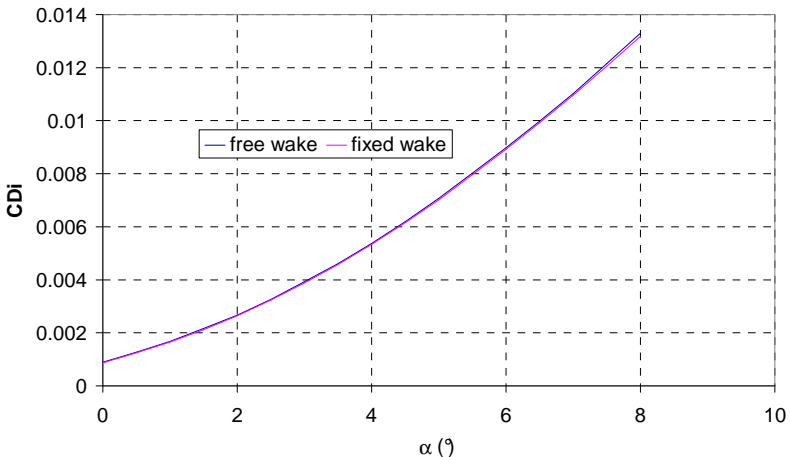


**Fig. 66 Induced drag coefficient; comparison between fixed wake and free wake.**

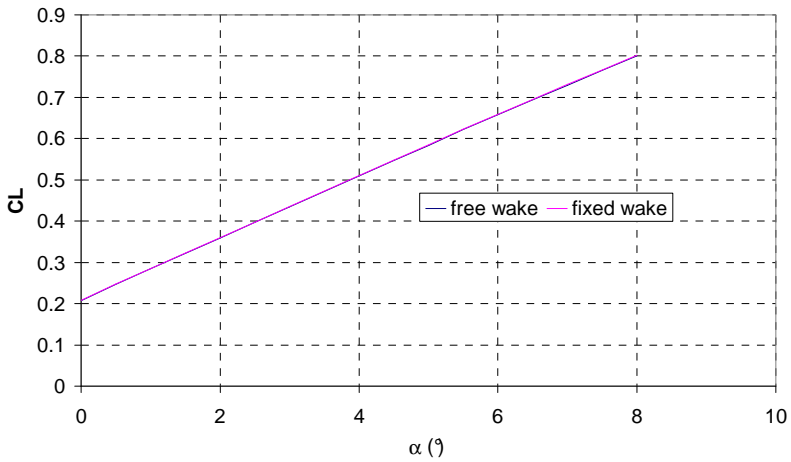


**Fig. 67 Lift coefficient; comparison between fixed wake and free wake.**

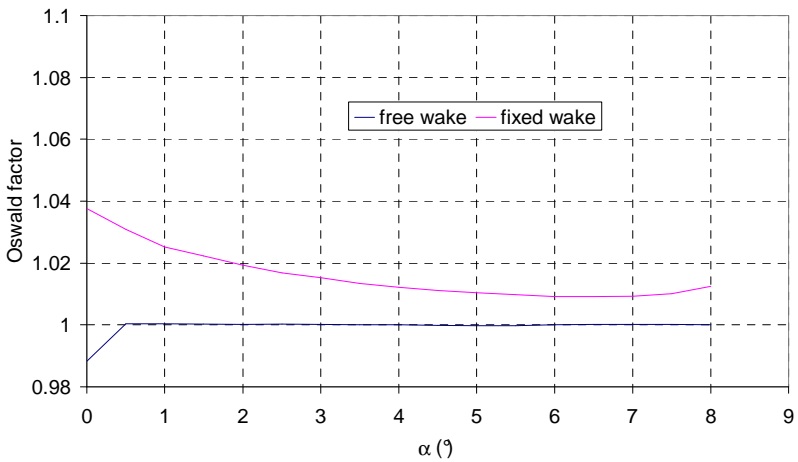


**Fig. 68 Oswald factor; comparison between fixed wake and free wake.**

#### 4.2.4 Low Aspect-Ratio Surfaces Improvement: Losito's Formulation

One of the limitations of the Prandtl's lifting line theory, is that it is valid for high aspect ratio wings; this is because one of the hypothesis is that each wing section works in the same way as in bi-dimensional problems. In other words, the aerodynamic characteristics of each wing section coincide with those of the corresponding airfoil without three-dimensional effects.

It is evident that for low aspect ratio wings this theory cannot be used because the presence of three-dimensional effects cannot be neglected.

In order to extend the capabilities of VWING also for low aspect ratio wings, the correction proposed by Losito<sup>26</sup> has been implemented.

This model does not take into account the effective three-dimensional interactions, but introduces a correction in the calculation of the local induced angle of attack.

In the classic formulation:

$$\alpha_i(y) = \alpha(y) - \frac{1}{2} \alpha_{i\infty}(y) \quad \text{eq 23}$$

By using the Losito's model, the coefficient of infinite induced angle of attack is a parameter  $n$  dependent by the aspect ratio.

$$n(AR) = \begin{cases} 0.5 + \frac{4}{\pi^2} \frac{1}{AR} (\log \pi AR - \frac{7}{8}) \\ 1 - \frac{1}{4} AR + 0.067147 AR^2 - 0.0062767 AR^3 \end{cases} \quad \text{eq 24}$$

If the aspect ratio is greater than 3 the first expression should be used; if the aspect ratio is less than 3 the second one.

Eq 23 can be rewritten as:

$$\alpha_{ind}(y) = \alpha(y) - n(AR)\alpha_{i\infty}(y) \quad \text{eq 25}$$

In order to test this improvement, a rectangular wing with aspect ratio equal to 2.5, calculated by using a vortex lattice method, is used as test case. The results of this comparison are indicated in Table 17 and shown in Fig. 69 and Fig. 70 in terms of spanwise aerodynamic load.

	VWING	VLM	err %
CL ( $\alpha=3^\circ$ )	0.149	0.149	0.31
CL ( $\alpha=6^\circ$ )	0.305	0.296	2.88
$Cl\alpha$ ( $1/^\circ$ )	0.052	0.049	5.55

**Table 17: Comparison between VWING numerical code and Vortex Lattice Method.**

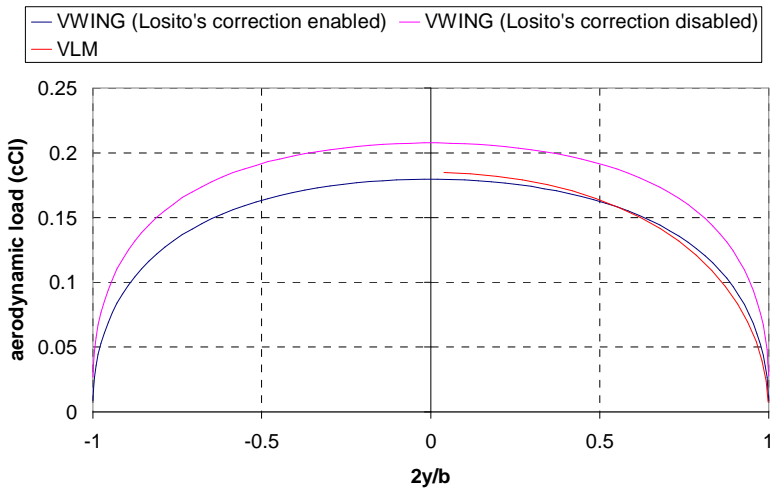


**Fig. 69 Comparison between VWING numerical code and Vortex Lattice Method; aerodynamic load along the span,  $\alpha=3^\circ$ .**



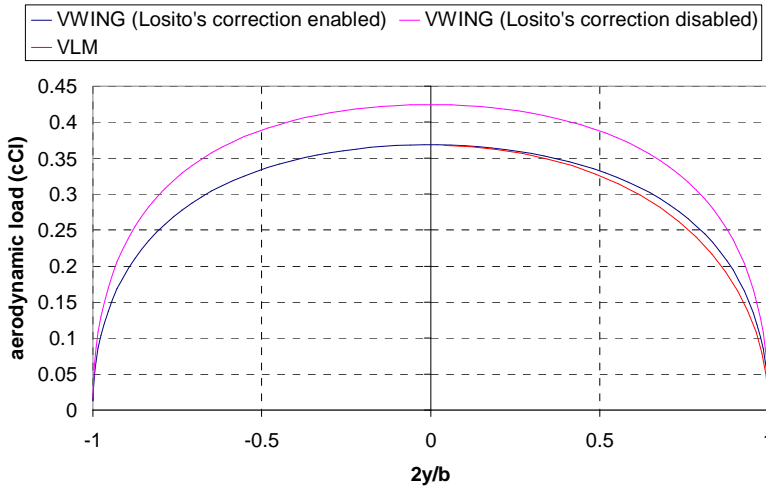


**Fig. 70 Comparison between VWING numerical code and Vortex Lattice Method; aerodynamic load along the span,  $\alpha=6^\circ$ .**

By using the Losito's model, there is a good agreement with the vortex lattice method.

#### **4.2.5 Stall and Post-Stall Improvement: Chattot's Artificial Viscosity**

For angles of attack below stall, the method converges very rapidly using almost any initial estimate for  $\mathbf{G}$  and a relaxation factor  $\Omega$  of unity. At angles of attack beyond stall, the method must be highly under relaxed and is very sensitive to the initial estimate for  $\mathbf{G}$ .

From the mathematical point of view, at stall and post-stall conditions, the matrix is not more diagonal dominant. This is due to the fact that in eq.22 there is a term in which the sign depends on the sign of  $\partial Cl / \partial \alpha$ .

In order to overcome this problem, the approach proposed by Chattot<sup>27,28</sup> has been implemented.

The basic idea is to add a artificial viscosity term ( $\mu$ ) to the expression; in this way the important property of diagonal dominance is ensured also in stall and post-stall conditions.

$$\mu \geq \sup\left(\frac{1}{4} dA_i \frac{\partial Cl_i}{\partial \alpha_i} \frac{\partial\left(\frac{v_i \cdot n_i}{v_i \cdot c_i}\right)}{\Delta G_{bj}} \frac{1}{1 + \left(\frac{v_i \cdot n_i}{v_i \cdot c_i}\right)^2}; 0\right) \quad \text{eq 26}$$

In order to do not modify the physics of the problem, the artificial viscosity term is added both in the R residual vector and in [J].

To test the effects of this extra term, a rectangular wing is considered as test case and analyzed by using VWING both with and without the artificial viscosity term.

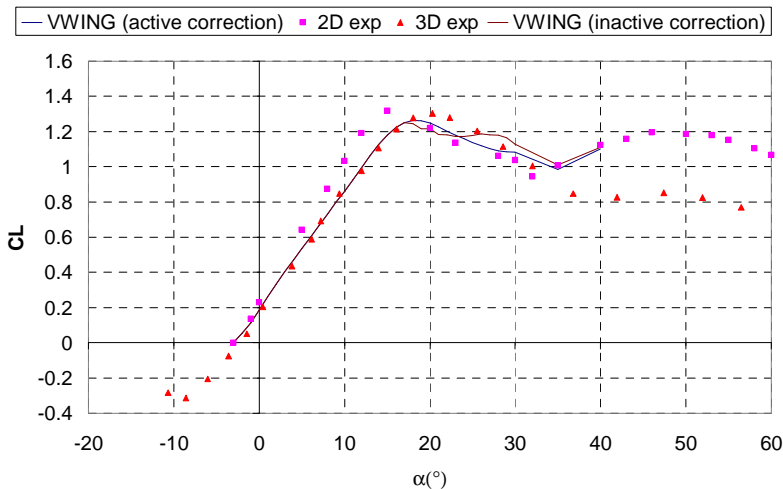


**Fig. 71 coefficient curve; effect of artificial viscosity factor.**

When  $\partial Cl / \partial \alpha$  is positive, there is not difference between VWING and experimental data, with or without artificial

viscosity enabled. When  $\partial Cl/\partial \alpha$  becomes negative, we should expect a trend similar to the experimental 2D curve. This is a direct consequence of the theoretical approach. It is evident the positive effect of the correction; the curve is more smooth and similar to the 2D curve.

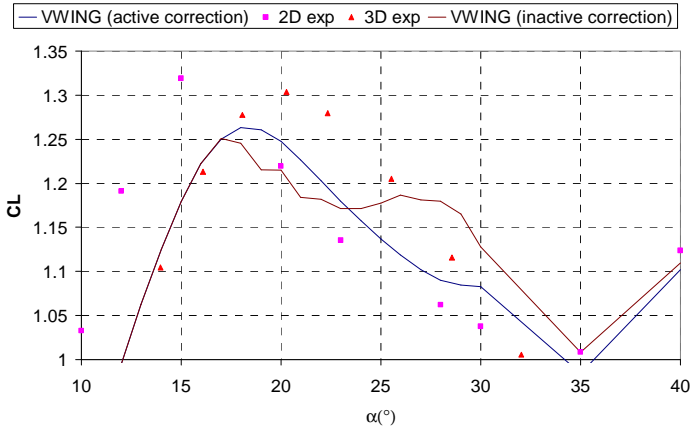


Fig. 72 Lift coefficient curve; effect of artificial viscosity factor, detail.

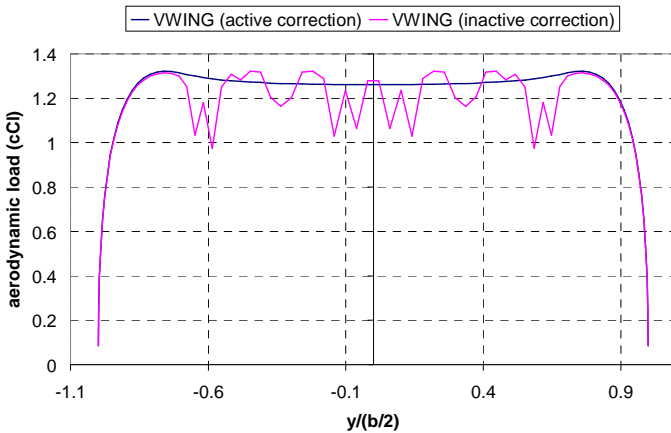


Fig. 73 Aerodynamic load along span; effect of artificial viscosity term,  $\alpha=20^\circ$ .

In Fig. 73 the comparison in terms of aerodynamic load, is shown. In this case the usage of the artificial viscosity term is fundamental to obtain a smooth distribution.

#### 4.2.6 Non Conventional Surfaces

One of the most interesting features of VWING is the possibility to analyse surfaces of arbitrary shape and orientation in the space. In order to test these capabilities, some results proposed by Kroo<sup>29</sup> have been used as test case. The Kroo's results have been obtained by using a vortex lattice method; for each configuration the ratio between span and height is prescribed to be 0.2.

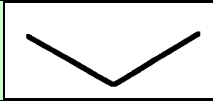
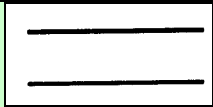
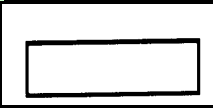
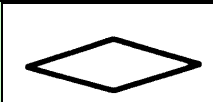
Wing Type		Oswald Factor	
		Kroo	VWING
V wing		1.03	1.02
Biplane wing		1.36	1.4
Boxed wing		1.46	1.43
Diamond wing		1.05	1.07

Table 18: Summary of analyzed configurations.

By looking at Table 18, there is a very good agreement between VWING results and Kroo results.

### 4.2.6.1 Winglets

In this paragraph, a wing with winglets is considered. The reference data in this case are obtained by Prof. Chattot's OLD numerical code.

The geometry is an elliptical wing with winglets (not blended). The aspect ratio is 11.7, the chord at the root is 0.2m and the winglet's toe angle is  $6.5^\circ$  (inward).

Parameter	OLD	VWING
AR	11.685	11.7
toein ( $^\circ$ )	6.5	
cr (m)	0.2	
CL	1.5	1.51
$\alpha_{CL=1.5}$ ( $^\circ$ )	-0.44425	-1.3
Osw fact.	1.221	1.25
CD (induced)	0.050205	0.05

**Table 19: Comparison between OLD and VWING; winglets.**

The winglet has been designed by Prof. Chattot to work at lift coefficient equal to 1.5. By comparison between OLD and VWING numerical code (Table 19) there is a very good agreements of results, both in terms of Oswald factor and induced drag coefficient.

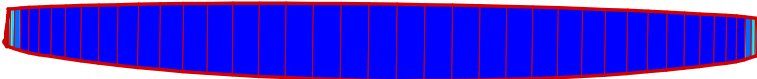


**Fig. 74 Planform configuration.**

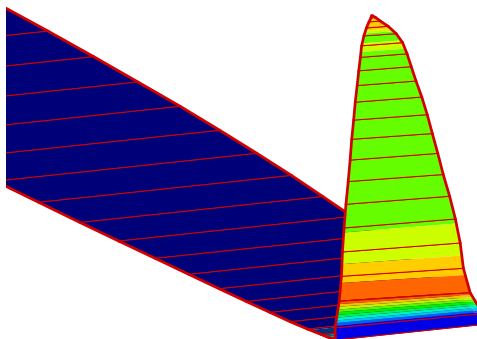


**Fig. 75 Winglet configuration.**

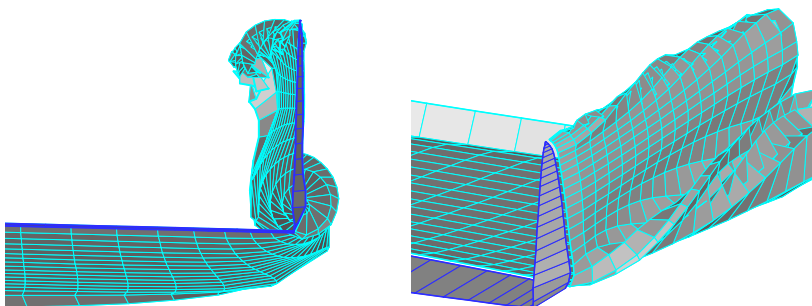


**Fig. 76 Wake visualization; free wake model used.**

#### **4.2.6.2 Blended Winglets**

Another case of winglets is analyzed in this section; the main difference compared with the previous case is that now the winglet is blended, with a uniform modification of dihedral angle.

Also in this case, the Prof. Chattot's OLD numerical code is used as reference.

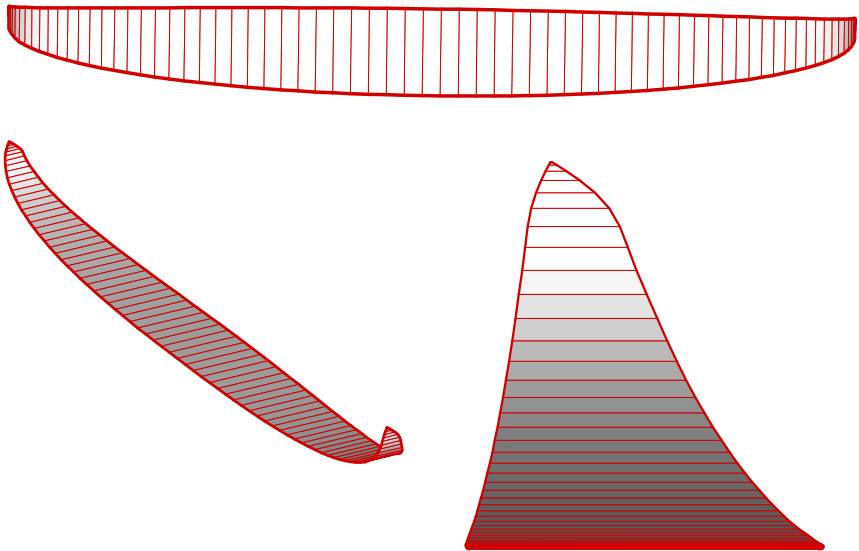


**Fig. 77 Blended winglet configuration.**

In this case the aspect ratio is 12, the chord at the root is 0.2m, but no toe angle is prescribed. The design condition is a lift coefficient equal to 1.5; both the induced drag coefficient and the Oswald factor are very similar.

Parameter	OLD	VWING
AR		12.
toein (°)		0
cr (m)		0.2
CL	1.5	1.5
$\alpha_{CL=1.5}$ (°)	-0.5	-1.5
Osw fact.	1.12	1.15
CD (induced)	0.0506	0.05

### 4.2.6.3 Multiple Winglets

The last case proposed to demonstrate the capabilities of VWING is the multiple winglets configuration; this is also an example of multi-body configuration.

In this wing, instead of the classic wing tip or the classic single winglet, a system of multiple winglets is applied. The aim of this idea is to decompose the wing tip vortex in more smaller vortices in which the sum of their intensities is less than that one of the single winglets. A second mechanism should be constituted by the fact that a thrust component can be generated by properly twisting and pitching the winglets.

For this configuration, the test case is a series of experimental tests<sup>30</sup> performed by ADGAG research group at wind tunnel test facility of University of Napoli “FedericoII”.

The geometry is an elliptical wing with NLF1015 airfoil, but instead of the traditional tip, multiple rectangular winglets (SD7032 airfoil) are installed.

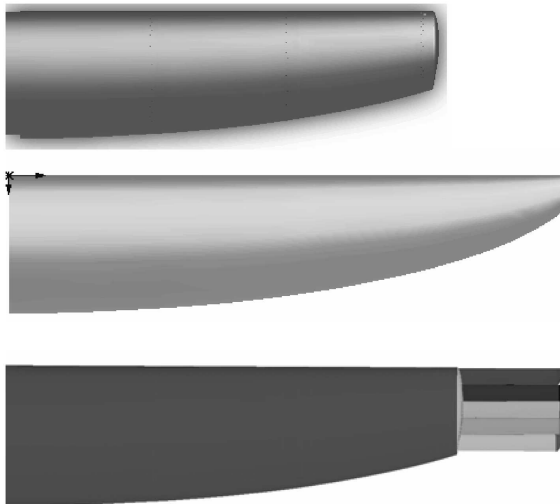


**Fig. 78** Wing shape.



wing	b (m)	S (m <sup>2</sup> )	Cr (m)	Ct (m)
Main-normal	1.51	0.452	0.37	0.097
Main-short	1.2	0.396	0.37	0.233
winglet	0.25	0.01	0.04	0.04

**Table 20: Wing characteristics.**

During the “construction” of the geometry (Fig. 79), a minimum gap between main wing and winglets has been preserved because of numerical problems in the initial tests.

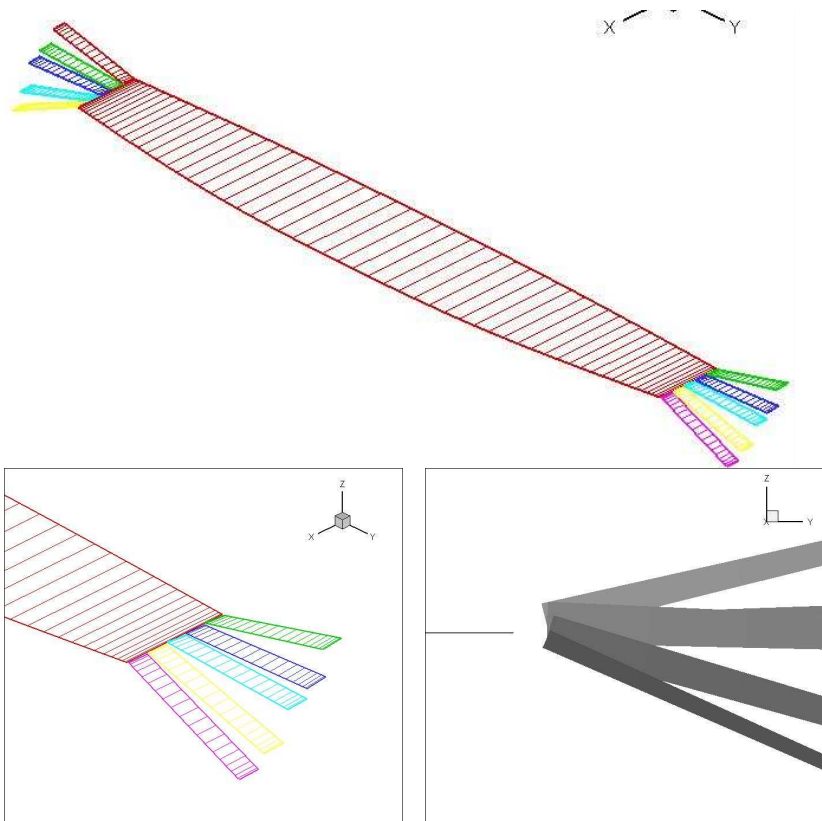


**Fig. 79 Wing geometry.**

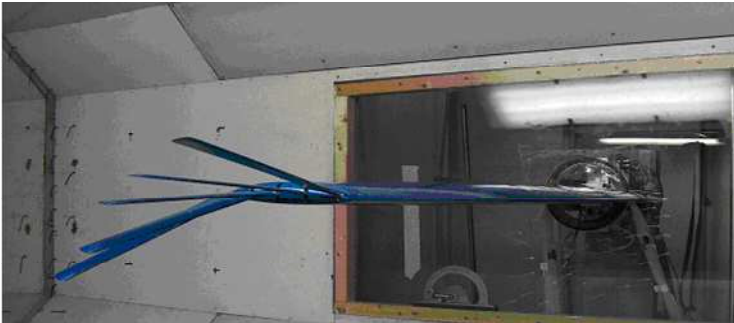


**Fig. 80** Wing with multiple winglets during the experimental tests.

This gap is around the 0.15% of the main wing span. In order to investigate the effect of the distance between two bodies, a preliminary study has been performed on an elliptical wing divided in two parts; several analysis have been done for different values of distance between wings.

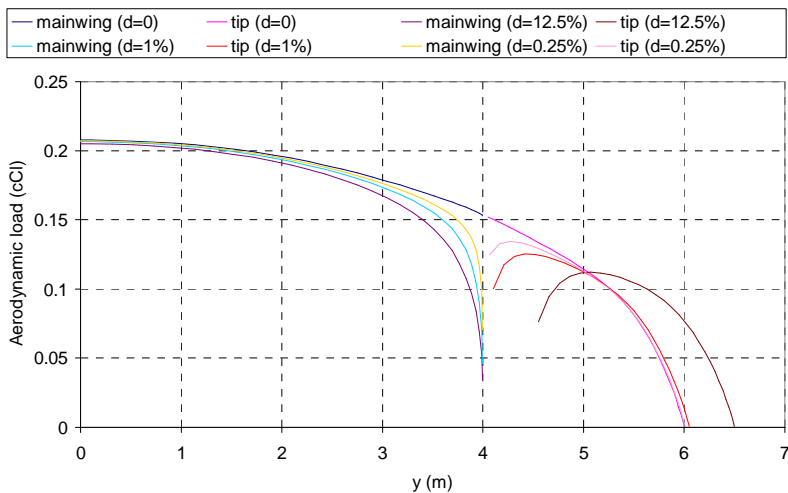


**Fig. 81** Effect of gap on aerodynamic load.

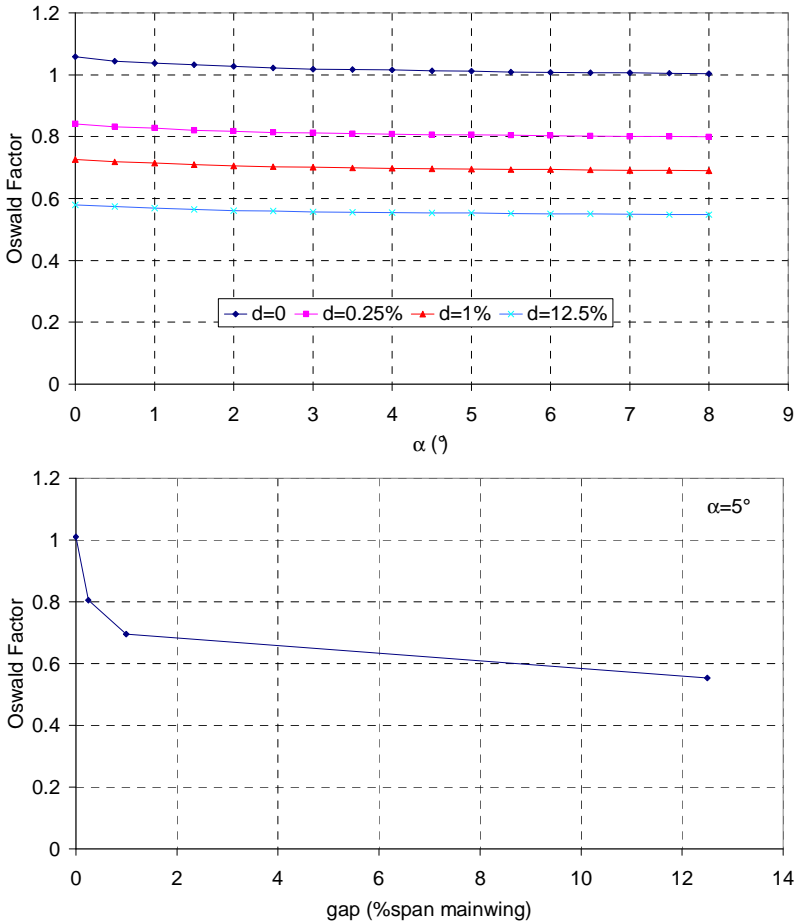


**Fig. 82 Effect of percent gap on the Oswald factor.**

After this preliminary analysis, the effective analysis on the multiple winglets configuration has been performed by using the minimum gap allowed to obtain numerical convergence (0.15%).

During the experimental tests, the comparison between aerodynamic characteristics of elliptical wing and multiple winglets configuration has been computed. This has been done for efficiency, lift coefficient and endurance parameter.

Then for the design condition, lift coefficient equal to 1.2, the difference between two configurations has been measured.

In numerical analysis performed by using VWING, the same procedure has been used and the results are illustrated in the following figures.

CL=1.2	Results	
	Numerical	Experimental
CD	-8%	-8%
L/D	9.60%	10%
Endurance Parameter	10.40%	9%

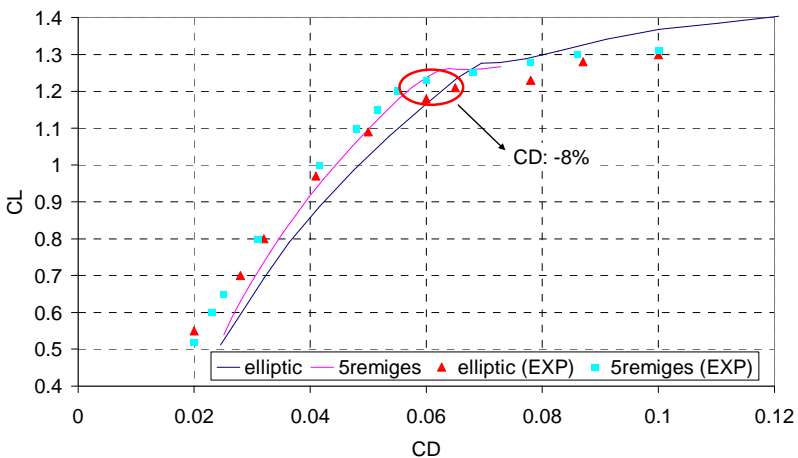


**Fig. 83 Drag polar curve; numerical-experimental comparison.**

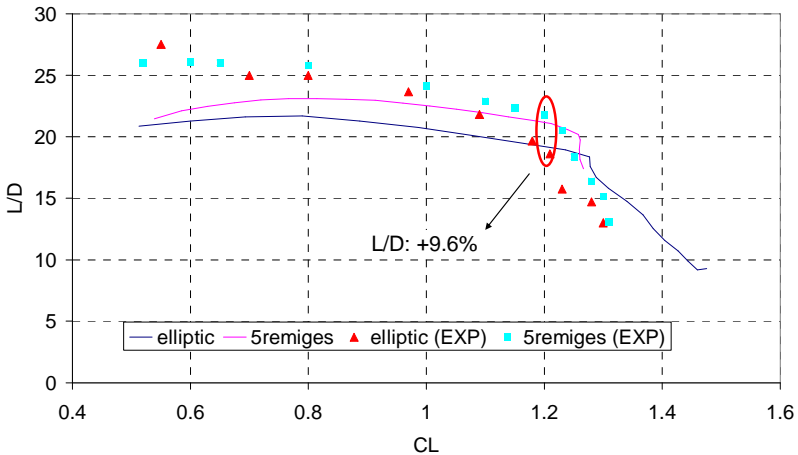


**Fig. 84 Efficiency curve; numerical-experimental comparison**

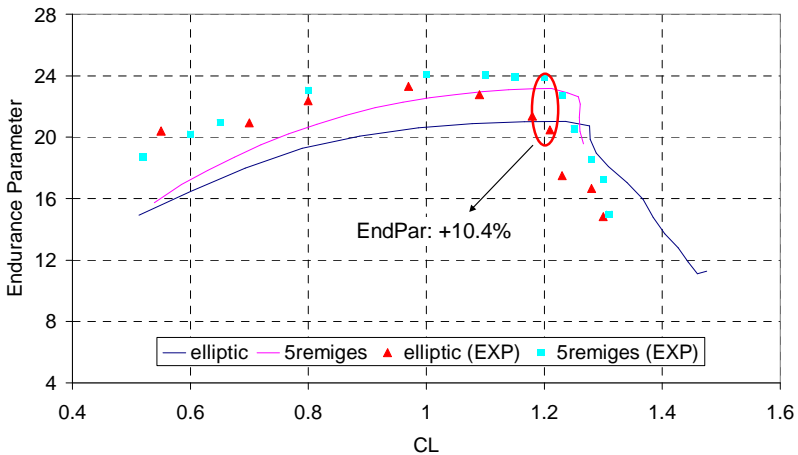


**Fig. 85 Endurance parameter curve; numerical-experimental comparison**

First of all, also by using VWING an aerodynamic enhancement is found if multiple winglets are used; then, in correspondence of the design condition a very good agreement is found between numerical evaluations and experimental tests.

### 4.3 Numerical Optimization Examples

In this section, three practical examples are provided to demonstrate the potentialities of the numerical optimization applied to the lifting surfaces design problem. In each subsection the design of a particular configuration to satisfy specific requirements is illustrated; for each case time histories and other details regarding the optimization process are provided.

The aim of this section is also to verify the capabilities of VWING as aerodynamic solver integrated in an optimization process. The selected cases are well know results of aerodynamics. Each case is repeated by increasing the quantity of degrees of freedom in order to test the robustness of solution and optimization process.

#### 4.3.1 Chord Distribution Optimization

Starting from a rectangular wing, numerical optimization has been carried out varying the chord distribution along wing span, in order to maximize the wing's Oswald factor. A span value of 12m and an initial chord value of 1m were fixed.

Design Variable ID	Design Variable	Lower bounds (m)	Initial value of design variable (m)	Upper bounds (m)
Dof1	Chord at y=2m	0.01	1	1.2
Dof2	Chord at y=4m	0.01	1	1.2
Dof3	Chord at y=6m	0.01	1	1.2

**Table 21: Degrees of freedom and bounds.**

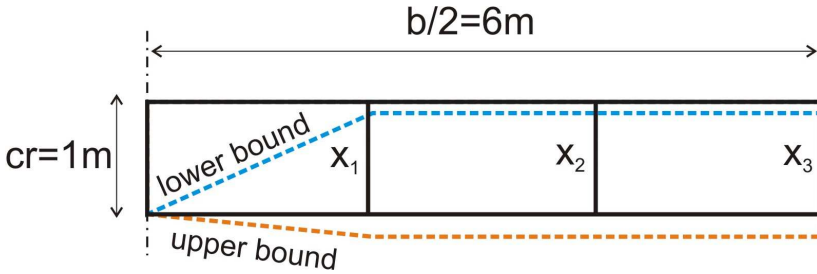


**Fig. 86** Wing's geometrical characteristics.

Table 21 shows the lower bounds and the upper bounds in case of three design variables.

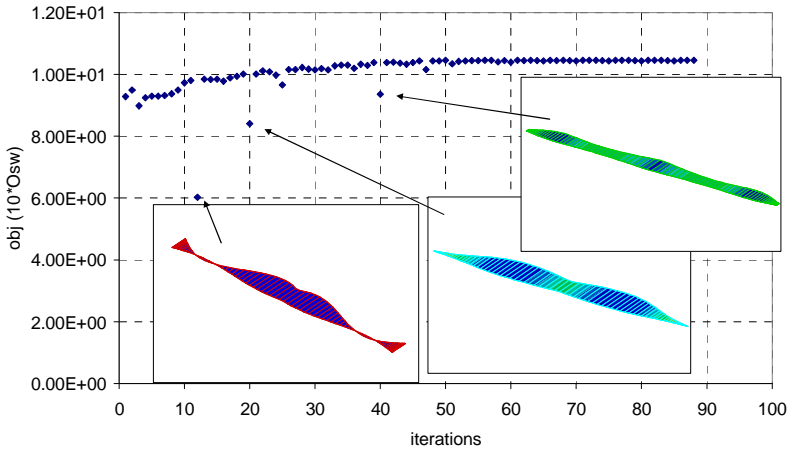


**Fig. 87** Objective function history.

In Fig. 87 the objective function history is shown, Fig. 88 shows the history of degrees of freedom.

Some of the calculated unfeasible configurations are illustrated in the following figures.

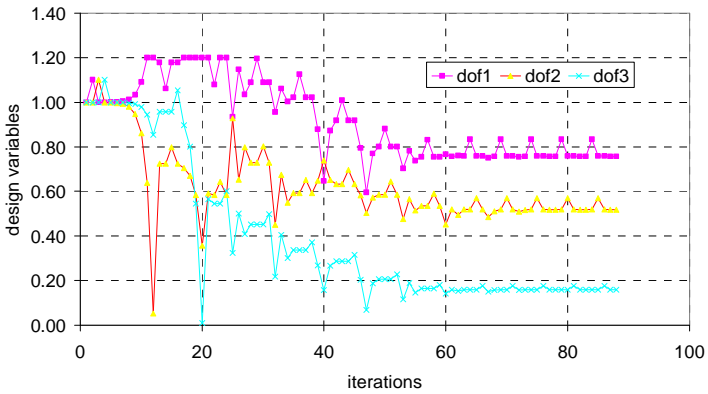


**Fig. 88 Degrees of freedom history.**

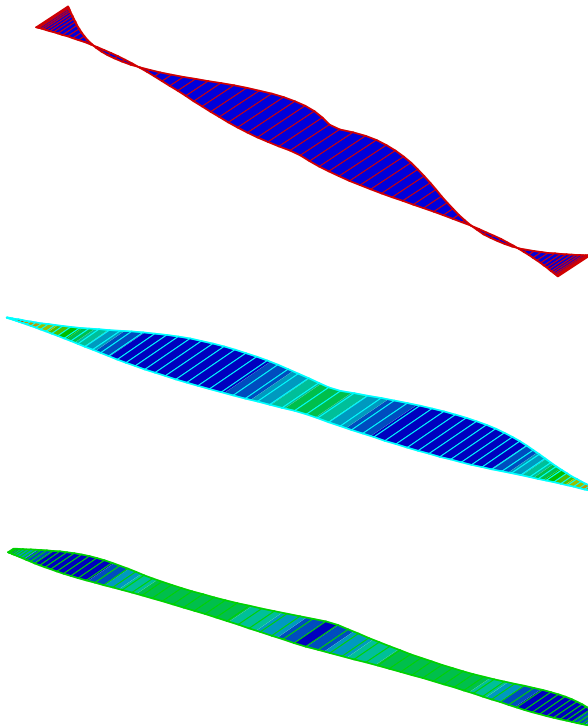


**Fig. 89 Non optimal configurations.**



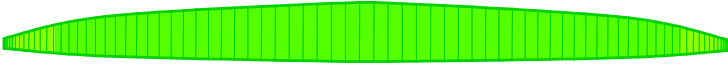


**Fig. 90 Optimal configuration.**

The optimal solution is the elliptical distribution and this result is a priori known because it is a theoretical result. The aim of the test is to verify if the numerical solution is close to the theoretical one.

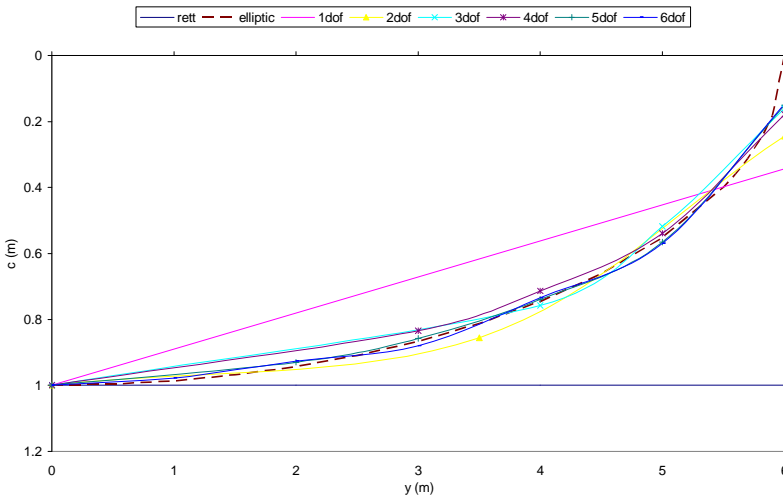


**Fig. 91 Chord distribution along the span; effect of degrees of freedom increasing.**

In order to study the robustness of the code in comparison with the number of degrees of freedom, the same test has been performed several times increasing the number of design variables. Fig. 91 shows the comparison between the final configurations and the theoretical elliptical distribution; in any case, a very good agreement is found

### 4.3.2 Twist Angle Distribution Optimization

Starting from a rectangular wing, numerical optimization has been carried out varying the twist angle distribution along wing span, in order to maximize the wing's Oswald factor. A span value of 12m and a chord value of 1m were fixed.

In order to study the robustness of the code in comparison with the number of degrees of freedom, the same test has been performed several times increasing the number of design variables. Table 22 shows the lower bounds and the upper bounds in case of six design variables.

Design Variable ID	Design Variable	Lower bounds (°)	Initial value (°)	Upper bounds (°)	Final value (°)
dof1	twist angle at y=1m	-5	-0.05	1	-0.0104
dof2	twist angle at y=2m	-5	-0.05	1	-0.122
dof3	twist angle at y=3m	-5	-0.05	1	-0.29
dof4	twist angle at y=4m	-5	-0.05	1	-0.58
dof5	twist angle at y=5m	-5	-0.05	1	-1.05
dof6	twist angle at y=6m	-5	-0.05	1	-2.2

**Table 22: Initial, final values of design variables and their bounds.**

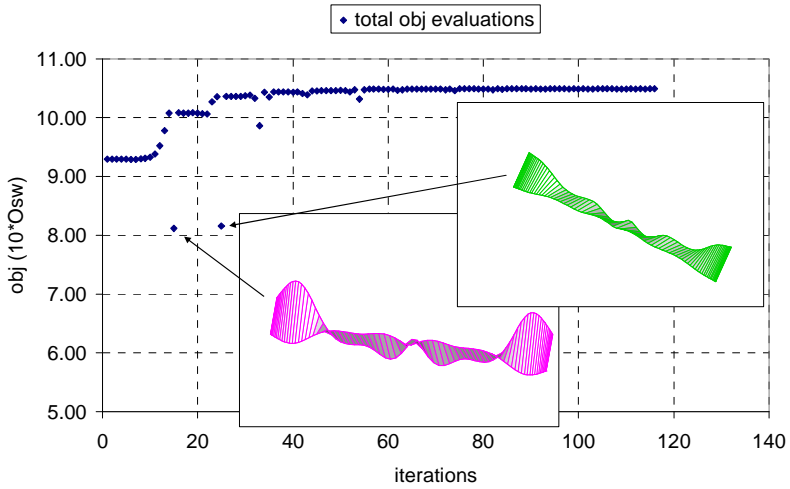


**Fig. 92 Objective function history.**

In Fig. 92, the objective function history is illustrated, in Fig. 93 the degrees of freedom history is shown.

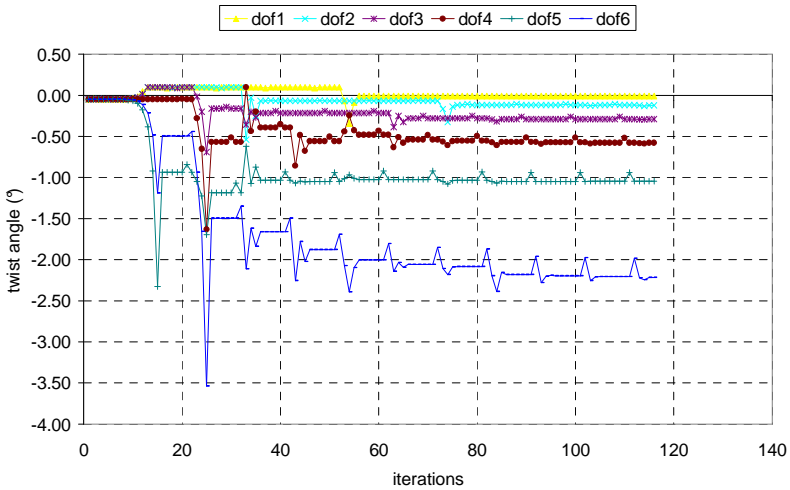


**Fig. 93 Degrees of freedom history.**

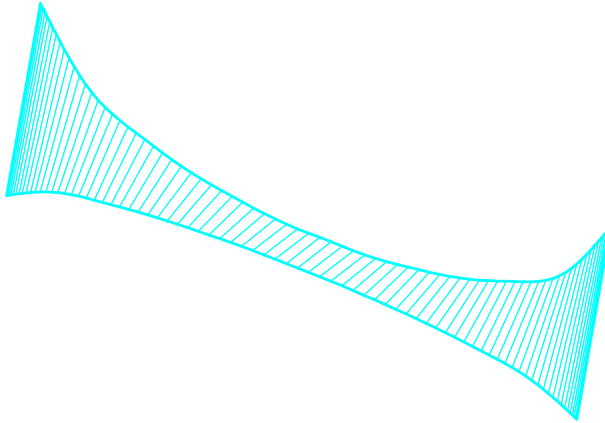


**Fig. 94 Final configuration.**

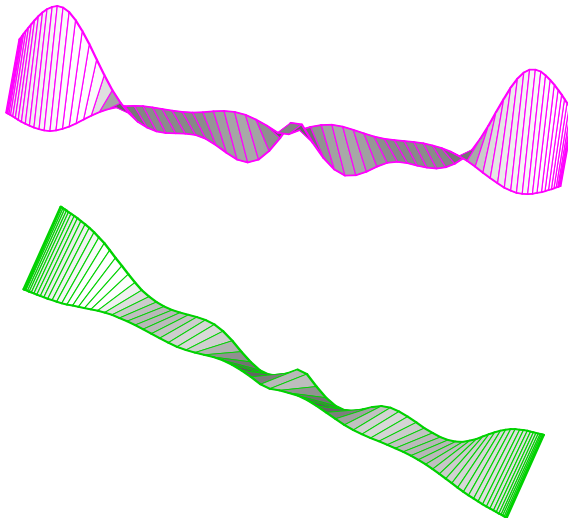


**Fig. 95 Some of the unfeasible configurations.**

Fig. 96 shows the comparison between the different twist angle distributions obtained by increasing the quantity of degrees of freedom; in any case there is a very good agreement with the elliptical distribution.

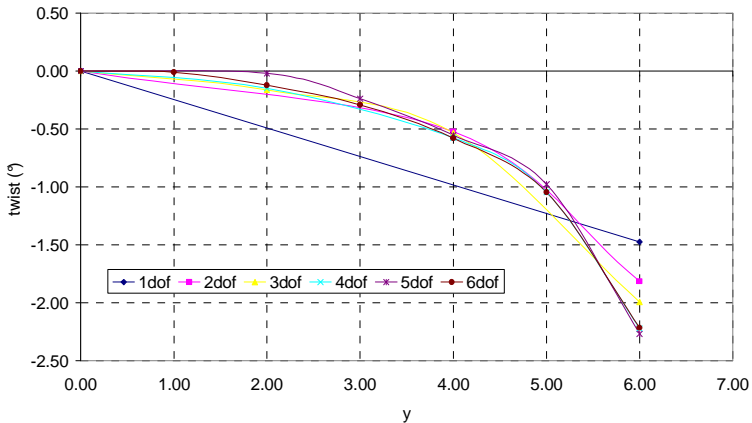


**Fig. 96 Twist angle distribution along the span; effect of degrees of freedom increasing.**

### 4.3.3 Dihedral Angle Distribution Optimization

In this example, the geometry shown in Fig. 97 is used as initial configuration in order to maximize the value of Oswald factor. The chord distribution is constant and not twist angle distribution is prescribed. The degrees of freedom are the vertical and spanwise positions of points indicated in the figure as 1, 2, 3. In this way the optimization process should calculate the best distribution of dihedral angles.

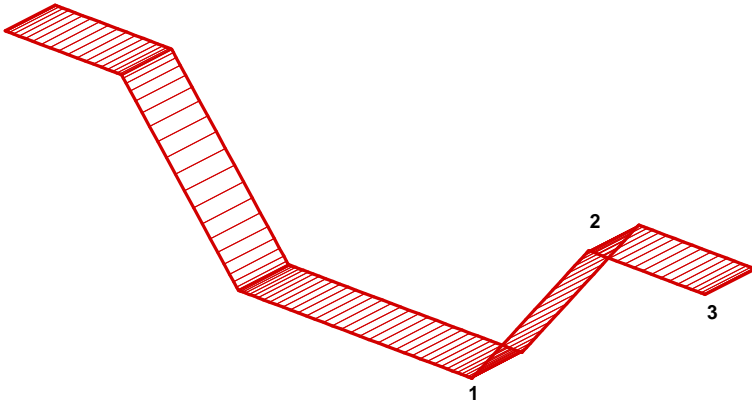


**Fig. 97 Initial configuration.**

DOF		Lower bound (m)	Initial Value (m)	Upper bound (m)	Final Value (m)
1	y1	0	2	10	1.96
	z1	0	0	3	0
2	y2	0	4	10	5.74
	z2	0	2.4	3	0
3	z3	0	2.4	3	3
Elapsed time (sec)				468	

**Table 23: Initial, final values of degrees of freedom and their bounds.**

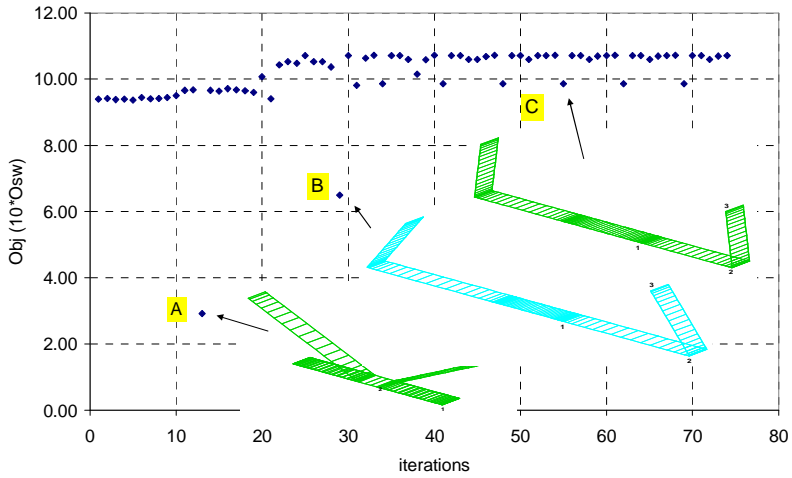


**Fig. 98 Objective function history.**

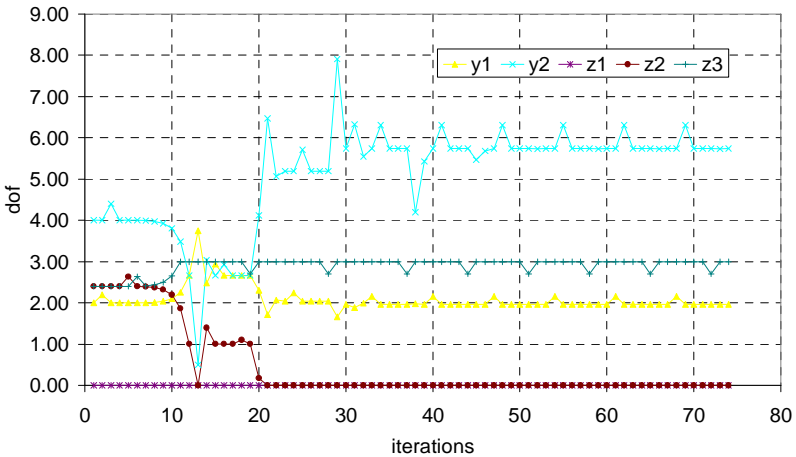


**Fig. 99 Degrees of freedom history.**

Fig. 98 illustrates the history of the objective function; during the optimization process, also unfeasible configurations are

explored, but the optimizer is robust and able to move far from these configurations. In the following figures, with reference at Fig. 98, some of these unfeasible configurations are shown and the optimal one is illustrated in Fig. 103.

In this case too the final result is in accordance with the expected one from the theory.

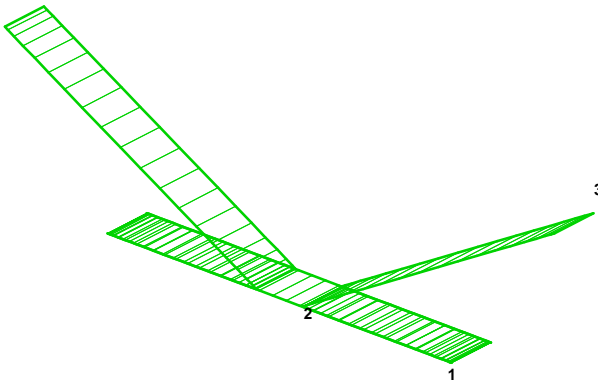


**Fig. 100 Configuration A.**

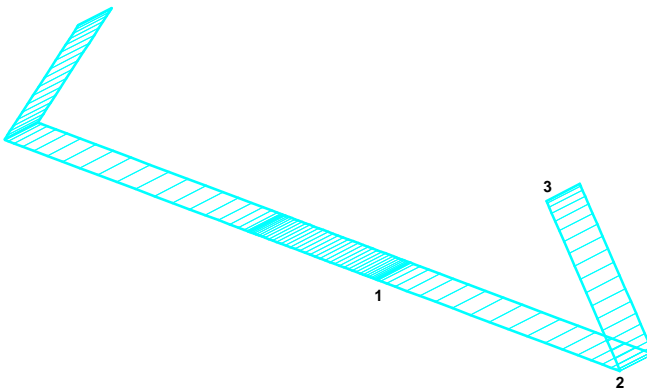


**Fig. 101 Configuration B.**



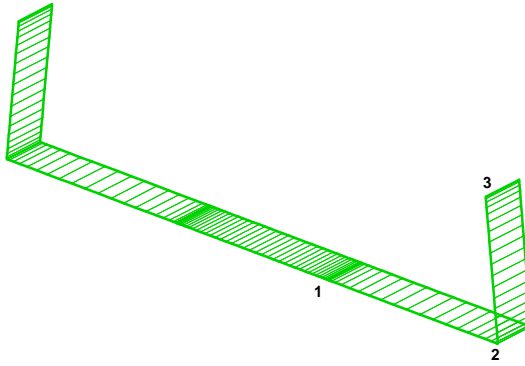


**Fig. 102 Configuration C.**

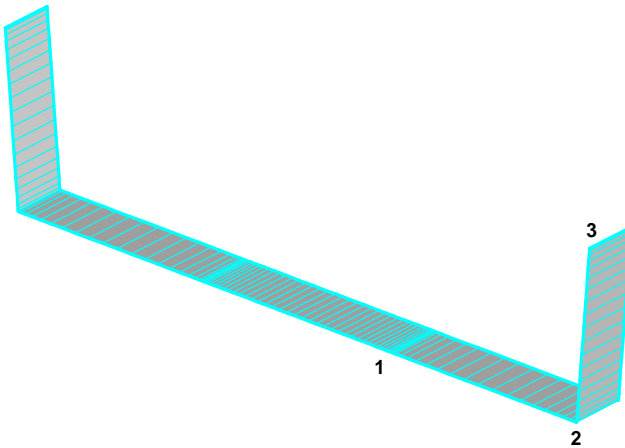


**Fig. 103 Optimal configuration.**



## Chapter 5

### Conclusions and Future Works

#### **5.1 Conclusions**

The aim of the present research was to investigate the possibility to use the numerical optimization approach as design methodology, instead of classic methods. Our attention has been focused on the aerodynamic design both of airfoils and lifting surfaces; in both two cases, it has been demonstrated that numerical optimization is an effective approach to solve design problems.

In airfoil design, a smart parameterization has been developed and realistic constraints, both geometric and aerodynamic, have been implemented; several efficient aerodynamic solvers, like XFOIL and MSES, have been integrated. The final result is the capability of design realistic airfoils in a very competitive time, both in single point and multi-point problems, taking into account, at the same time, aerodynamic, geometrical and feasibility constraints.

About lifting surfaces, a new numerical code, named VWING, has been developed and extensively tested. In order to increase its capabilities, several extensions have been added and tested to the original formulation. One of the more interesting features of VWING is the possibility to analyze multi-body and non conventional configurations. VWING is also used as aerodynamic solver of an optimization process in which the aim is to develop innovative and non planar configurations. The numerical examples proposed in this thesis demonstrate the potentialities for innovative configurations design.

## **5.2 Future Works**

In the next future, the idea is, on one hand, to enhance the general robustness of the developed numerical codes in order to increase their versatility and use them in more complex contexts. This can be done, for example, by implementing more constraints and integrating some other aerodynamic solvers in the optimization process. In airfoil design, by adding VGK numerical code or some CFD codes, it will be possible to extent the field of application of numerical optimization approach also to transonic and supersonic studies. About the design of lifting surfaces, by integrating, for example panel codes, it will be possible to take into account also interferences between wing sections (i.e. wing-winglets juncture).

About VWING code, despite of its formulation based on the Prandtl's lifting line theory, several improvements are scheduled; in this way its usage will be extended and also in design processes, it will be possible to study more complex conditions.

On the other hand, the present research demonstrated the potentialities of the numerical optimization also in design problems. The idea is to extend these potentialities also in multidisciplinary problems as, for example, design of lifting surfaces taking into account not only aerodynamics, but also structures and performances. If a proper formulation is implemented, it will be possible also take into account aspects connected with costs.

In the present investigation, airfoil design and lifting surfaces design have been developed as two different and independent problems; an interesting evolution can be the development of an optimization process in which, both airfoil and wing shape are degrees of freedom of the problem at the same time.

## Appendix A: Publications

1. D.P. Coiro, F. Nicolosi, A. De Marco, F. Scherillo, F. Grasso, *“High-Lift Systems for STOL Ultra-Light Aircraft, Design and Wind-Tunnel Tests”*, XIX AIDAA National Congress, 17-21 September 2007, Forlì (Fc), Italy.
2. D.P. Coiro, S. Figliolia, U. Maisto, S. Melone, F. Grasso, *“Horizontal Axis Tidal Current Turbine: Numerical and Experimental Investigations”*, OWEMES 2006, 20-22 April 2006, Civitavecchia (Roma), Italy.



## HIGH-LIFT SYSTEMS FOR STOL ULTRA-LIGHT AIRCRAFT, DESIGN AND WIND-TUNNEL TESTS

D.P. COIRO, F. NICOLOSI, A. De MARCO, F. SCHERILLO, F. GRASSO

*Dipartimento di Ingegneria Aerospaziale (DIAS), Università degli Studi di Napoli Federico II, Napoli, ADAG research group (Aircraft Design and Aeroflightdynamics Group); [www.dpa.unina.it/adag](http://www.dpa.unina.it/adag)*

### ABSTRACT

*Design of a STOL (Short Take-Off and Landing) ultralight aircraft has been carried out at Dipartimento di Ingegneria Aerospaziale (DIAS) of University of Naples by ADAG research group. Design of the aircraft has been focused on an accurate design of the high-lift system that allows very good STOL performances. In the paper all activities related to the design of the flap and slat geometries will be presented. The paper deals with the general design of flap and slat on the wing and with an accurate design of a 3-component airfoil able to achieve a maximum lift coefficient of about 4.0 in landing configuration. The numerical analysis and design activities (airfoil and 3-D design) have been supported by deep and intensive experimental activities that have been performed in the main wind-tunnel belonging to DIAS. Many experimental results will be presented and compared to numerical predictions.*

### 1. INTRODUCTION

Following the experience acquired in our department in designing light and ultra light aircraft, the design of a new STOL (Short Take-Off and Landing) Ultra-Light Aircraft has been carried out at DPA by ADAG group. The aircraft, named Easy-Fly has been designed with a research activity financed by Aerosoft S.r.l. that started in 2004. A general view of the aircraft is shown in fig. 1-2. The commercial success of the aircraft is mainly dependent on the achievable STOL aircraft capabilities and on

improved STOL characteristics respect to other similar light aircraft. Some STOL light aircraft as the well-known Zenith CH701 (fig.3) have been appreciated worldwide and demonstrates that STOL capabilities can be a key for commercial success in the category of light and ultralight aircraft. Recently other ultralight aircraft have been modified and sold in STOL version. The Savannah ADV (fig. 4) produced by ICP has been introduced in the market in 2005. These aircraft are usually characterized by a not streamlined fuselage and by not very complex and sophisticate airfoil shape. In example Savannah ADV adopt a NACA 5-digit airfoil and a very simple flap shape. Some STOL aircraft of this category are characterized by a fixed slot at leading edge (see fig. 5) penalizing parasite drag and flight speed at cruise conditions. The starting idea on the base of Easy-Fly project was to design a STOL ultralight aircraft made in composite material with good drag characteristics and very low stalling speed. The wing high-lift system (flap and slat) was designed to have low-drag characteristics in cruise conditions and very high maximum lift coefficient in full-flap configuration. Both leading edge slat and slotted flap are retractable. The general design of the aircraft was presented in previous conferences [1-2]. The aerodynamic design (performed through numerical aerodynamic analysis) and wind-tunnel tests of the high lift systems (which is composed by a 3 component airfoil with slat and slotted flap) has been performed during several months in 2005-2006 and is presented in the present paper.



*Fig.2: Perspective CAD view of the aircraft.*



*Fig.3: CH701 aircraft – Zenith Aircraft*





*Fig.4: Savannah ADV - ICP aircraft Industries*

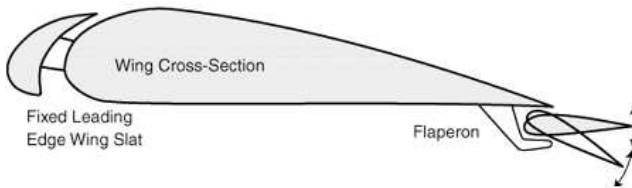


*Fig.5: High-lift system of standard STOL ultralight aircraft (CH701 wing section).*

## **2. PRELIMINARY 2-D CHARACTERISTICS AND HIGH-LIFT PLANFORM DESIGN**

Obviously the high-lift capabilities of the aircraft depends on the aircraft maximum lift coefficient with flap extracted. The chance to get a very-high maximum lift coefficient for the aircraft depends of course from the high-lift system (slat-flap) 2-D effectiveness and from its spanwise extension. The flap spanwise extension has been chosen considering the constraint of acceptable aileron extension and consequent aircraft rolling capabilities. The slotted flap extend from wing root up to 70% of the wing semi-span. The first step has been the choice of flap and slat system and their chord extension. A slotted flap and a fowler flap solutions have been considered in the preliminary design phase. In order to obtain information about a 2-D high lift system that can satisfy design specifications, a sizing procedure, based on Roskam's semi-empirical methodology [3], has been used. In particular two solutions have been considered for the flap: single-slot flap and fowler flap. A chord extension of about 30% has been considered for the flap to optimise flap effectiveness and to contain the increase of wing pitching moment. Table 1 and Table 2 show the results of this preliminary analysis. From the performed analysis it can be seen that a 2-D lift increment (full flap landing conditions) of 1.4 can be obtained through a

slotted flap and an increment of 1.80 for the fowler flap solution. The assumed slat chord (about 15%) should lead to an increment of about 0.40. Table 2 shows that, starting from a 2-D maximum lift coefficient of 1.65 (clean airfoil) a 2-D  $c_{l\_max}$  for the flapped configuration of 3.5 should be achieved with the slotted-flap-slat configuration. Adopting the fowler flap it is possible to obtain a better value of maximum lift coefficient,  $C_{l_{max}}$ , but the singleslot flap has been chosen because the fowler solution is more complex, more expensive and heavier, thus it is not compatible with an ultralight aircraft.

<b>SINGLE SLOT</b>	cf/c						
	0.30						
	$\delta f$ [deg]	c'/c	$\Delta C_l$	$\Delta C_{l_{max}}$	$(C_l \alpha) \delta$ [rad <sup>-1</sup> ]	$\Delta C_d$	$\Delta C_m$
Take-off	20	1	1.24	0.59	6.69	0.018	-0.24
Landing	40	1.05	2.10	1.39	7.02	0.065	-0.45
<b>FOWLER</b>	cf/c						
	0.30						
	$\delta f$ [deg]	c'/c	$\Delta C_l$	$\Delta C_{l_{max}}$	$(C_l \alpha) \delta$ [rad <sup>-1</sup> ]	$\Delta C_d$	$\Delta C_m$
Take-off	15	1.11	1.07	0.63	7.43	0.009	-0.26
Landing	40	1.15	2.42	1.80	7.69	0.065	-0.62
<b>SLAT</b>	cs/c						
	0.15						
	$\delta f$ [deg]	c'/c	$\Delta C_l$	$\Delta C_{l_{max}}$	$(C_l \alpha) \delta$ [rad <sup>-1</sup> ]	$\Delta C_d$	$\Delta C_m$
Take-off	12	1.11	0.04	0.42	7.43	0.033	...
Landing	""	""	""	""	""	""	""

Table 1: Two-dimensional geometrical and aerodynamic achievable characteristics (semi-empirical)

<b><math>C_{l_{max}}</math></b>	Clean airfoil	single slot	fowler	slat	single slot+slat	fowler+slat
Take-off	1.65	2.23	2.28	2.07	2.65	2.70
Landing	""	3.03	3.45	""	3.46	3.87

Table 2: Expected 2-D aerodynamic performances of different devices.

Starting from assumed airfoil characteristics, design and choice of flap and slat extension on wing planform has been performed. Through standard Roskam semi-empirical methodologies [3] the wing flapped area has been calculated. A value of maximum lift coefficient of the aircraft with the leading edge extracted of about 2.20 has been considered. The aircraft design specifications (stall speed in landing configuration below 50 Km/h with a MTOW=450 Kg) lead to required values of aircraft maximum lift coefficient of 2.60 in take-off configuration and 3.20 in full-flap condition. The required maximum lift coefficient increment can be estimated for take-off and landing:

$$\Delta C_{L_{\max_w\_TO}} = 1.06(C_{L_{\max TO}} - C_{L_{\max}}); \quad (1)$$

$$\Delta C_{L_{\max_w\_L}} = 1.06(C_{L_{\max L}} - C_{L_{\max}}); \quad (2)$$

The required flapped area (for the slotted flap solution) can be estimated from the following formula:

$$\Delta C_{L_{\max}} = \Delta C_{L_{\max_w}} (S_{wf}/S)(K\lambda) \quad (3)$$

knowing the 2-D achievable maximum lift coefficient increment with slotted flap, assuming minimum and maximum possible flap extension (min. 40% span,  $S_{wf}/S=0.40$ ; max 80% span  $S_{wf}/S=0.80$ ) and interpolating with the desired global max lift coefficient increment of (1) and (2). Table 3 show results of this design process. An extension up to about 70% of wing span has to be chosen to cope with landing configuration requirements. The slotted flap extend from 10% up to 70 % of wing span. Fig. 6 shows the wing drawings with high-lift systems and aileron. The aileron extension (30% of wing span) allows acceptable rolling and lateral control capabilities. An expected value of aileron efficiency  $p_b/(2V)$  of about 0.070 has been calculated.

CLmax	CLmaxTO	CLmaxL				
2,20	2,60	3,20				
$\Delta CL_{maxTO}$	$\Delta CL_{maxL}$	$K\Delta$				
0,42	1,06	0,92				
TO	k	$\Delta C_{ITO}$	$\Delta CL_{maxTO}$	Swf/S	$\Delta CL_{maxTO}$	
	0,80	1,24	0,99	0,4	1,15	
				0,8	0,58	
L		$\Delta C_{IL}$	$\Delta CL_{maxL}$	Swf/S	$\Delta CL_{maxL}$	
		2,10	1,68	0,4	2,88	
				0,8	1,44	
Flap Area	m	q	Swf/S landing	m	q	Swf/S take-off
	-0,28	1,20	0,73	-0,69	1,20	0,51

Table 3: slotted flap extension design

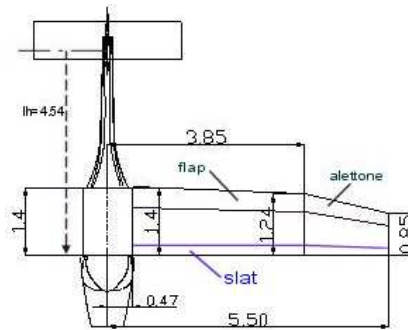


Fig.6: Flap, aileron and slat extension on Easy-Fly wing.

### 3. AIRFOIL DESIGN

A new airfoil was designed at DIAS. Aerodynamic requirements have been:  $CL_{max}$  not less than 1.6 at Reynolds number  $1.7e6$ ,  $Cd_{min}$  less than 0.006 and  $Cm_{c/4}$  greater than  $-0.08$  at Reynolds number  $4e06$ ; looking at other ULM aircraft, a 13.5% chord referred thickness was chosen. The adopted design methodology [4] has included preliminary airfoil selection to obtain a

starting point not too far from design requirements. Fig. 7 shows the airfoil design loop. The design loop includes evaluation of complete aircraft aerodynamics and performances performed through AEREO code [5]. Our starting airfoil was GAW(1) (its maximum thickness has been reduced to 13.5%; see fig. 8); at first, mean line maximum camber was reduced and its position was moved forward to improve  $C_{m_{c/4}}$ . In order to achieve high lift performances, the leading edge has been slightly dropped; at the same time leading edge radius was increased to obtain good stall characteristics. The obtained airfoil was named G1 (see fig.8). The G1 airfoil was compared to several airfoils as NLF0115 (13.5% thickness reduced) that have better  $C_{m_{c/4}}$  (lower pitching moment). As an example a comparison of effect of airfoil shape on complete aircraft aerodynamics is shown in fig. 9 and 10. Fig. 9 shows effect of airfoil on aircraft trimmed lift curve and fig. 10 shows the effect of airfoil aerodynamics on complete aircraft estimated trimmed polar. Performances estimation has been done and is presented in table 4. The aircraft tail loads at cruise conditions becomes severe if the airfoil is characterized by high pitching moment values. In order to improve these aspects, the trailing edge area was rotated  $3^\circ$  upward. Airfoil was named G1-3F (see fig.8). During the modifications, both airfoil and global aircraft performances have been checked to verify if the design goals had been met, see fig. 7; complete aircraft performances check was done using AEREO code [5]. Using XFOIL code [6] and other aerodynamic codes developed at DIAS [7, 8, 9] the aerodynamic characteristics of original GAW airfoil and G1-3F airfoil have been estimated. The calculations have been extended to stall and post-stall conditions in order to check influence of geometry modification on maximum lift coefficient. In fig. 11 and 12 the lift curve and moment coefficient are shown. It can be seen that the maximum lift coefficient (at  $Re=2$  million) of G1-3F is very close to that one of original GAW airfoil. A value close to 1.60 has been estimated. Fig. 11 shows that G1-3F is characterized by a very low pitching moment coefficient (about  $-0.040$ ) compared to that one ( $-0.10$ ) relative to GAW airfoil. In term of drag characteristics, G1-3F airfoil is characterized by similar drag coefficient values (about 0.0060 at  $Re= 4$  mill.) respect to GAW, showing some laminar flow extension on upper and lower surface.

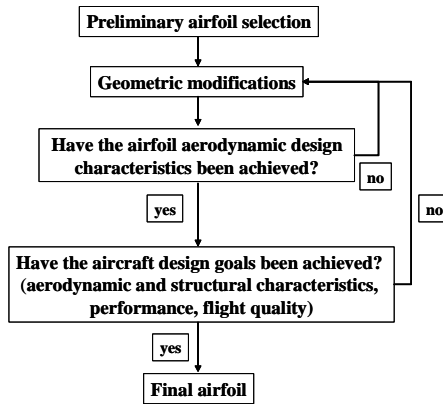


Fig.7: Airfoil design loop.

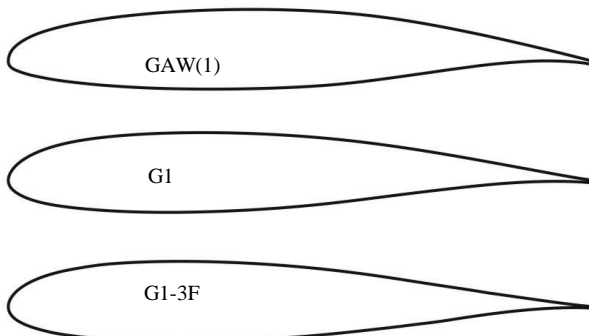


Fig. 8 : 2-D airfoil shapes and chosen airfoil

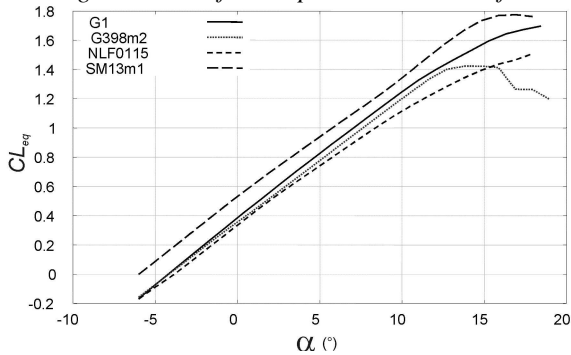


Fig.9: Effect of airfoil on aircraft lift curve.

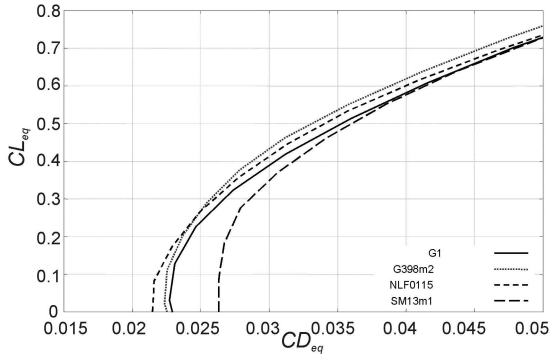


Fig. 10 : Effect of airfoil on aircraft drag polar

Airfoil	$V_{max}$ , km/h	$V_s$ , Km/h	$V_{sff}$ , Km/h		$RC_{max}$ , m/s	$Lh_{Vmax}$ , Kg
			slat + single slot flap	slat + fowler flap		
G1	194.095	64.926	47.568	45.565	6.69	-159.63
NLF0115M1	194.529	69.457	49.266	47.051	6.85	42.77
G398m2	194.769	67.456	48.537	46.414	6.78	-104.77
SM13m1	191.508	62.172	46.453	44.581	6.63	-310.73

Table 4: Easy-Fly aircraft performances with different airfoils

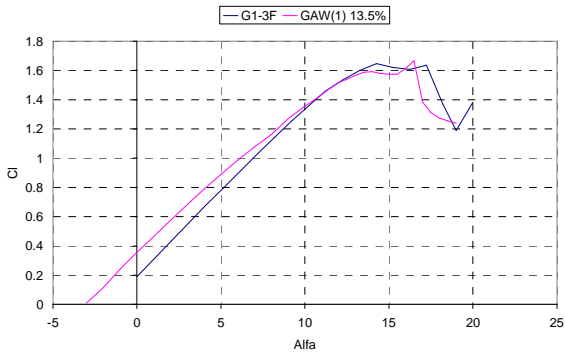


Fig. 11: GAW and G1-3F airfoil lift curve.  $Re=2$  mill.

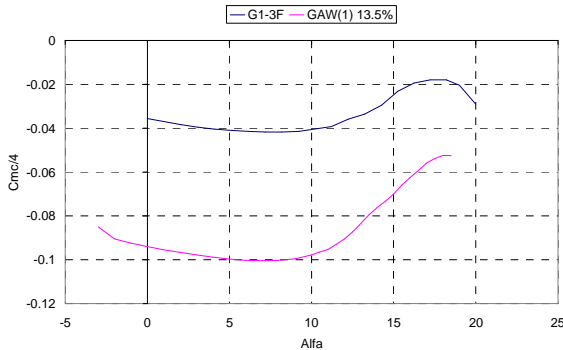


Fig. 12 : GAW and G1-3F pitching moment

#### 4. HIGH-LIFT SYSTEM DESIGN

Starting from G1-3F airfoil, an advanced high lift system, including retractable slat and flap, has been designed. Design activities have been performed considering similar research and design performed by other authors [10, 11, 12]. Fig. 13 shows the high lift design loop; assuming semi-empirical results as aerodynamic requirements, slat and flap have been separately designed, then the complete high lift configuration has been developed and optimised through the use of the well known MSES [13] multi-component 2D aerodynamic code. The landing condition has been taken in consideration as main design configuration. In order to obtain a  $C_l$  not less than 3.4 at the angle of attack of  $10^\circ$  with flap deflection of  $40^\circ$  at Reynolds number of  $1.3e06$  and assuming a flap chord of 30% compared to the airfoil chord, different shapes have been developed acting upon the flap shape, slot shape and lip extension. The configuration is characterized by a quite large extension of the main component's lip compared to the classical single-slot flap configurations and by the presence of the cove to guarantee the minimum interference in cruise condition and a kind of self-adaptability of the flow's direction in the slot. In the same way, in order to achieve a  $C_l$  not less than 1.9 at angle of attack of  $15^\circ$ , different slat geometries have been designed playing on slat shape and slot shape. A  $25^\circ$  deflection angle and a 15% slat chord compared to the airfoil chord have been fixed from preliminary sizing process. Merging flap geometry and slat geometry together, the three components configuration fs6 (see fig. 14) has been obtained. The single-slot flap is characterized by lower hinge position. In order to reduce the forces acting upon the hinge point, a modification of the flap leading edge has been applied. Fig. 14 shows the final shape. The G1-



3F airfoil in landing configuration is shown in the same figure with flap deflection of about 40 deg. and slat deflection of about 25 deg.

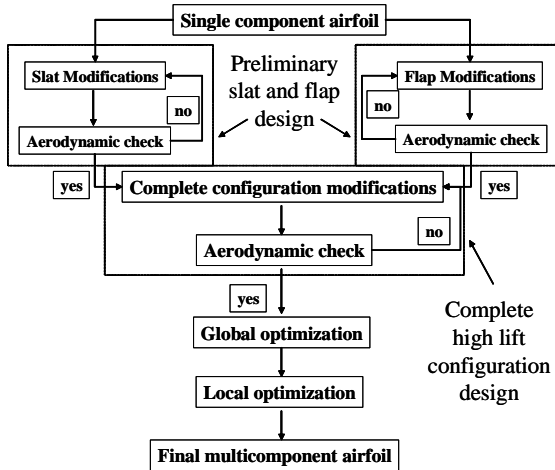


Fig. 13 : Flap and slat design loop

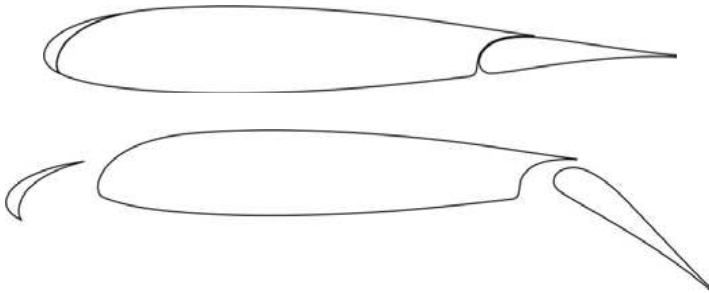
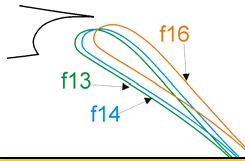


Fig. 14 : Final slotted flap and slat configuration

The numerical results obtained with MSES were very challenging, with a 2-D maximum lift coefficient of about 4.00 at Reynolds of 1.3 million.

#### 4.1 Global optimization of flap position

Different configurations with different flap position and the same slat position have been analysed with MSES; table 5 shows the explored geometries and the calculated  $C_{l_{max}}$  at the angle of attack of  $18.5^\circ$ .



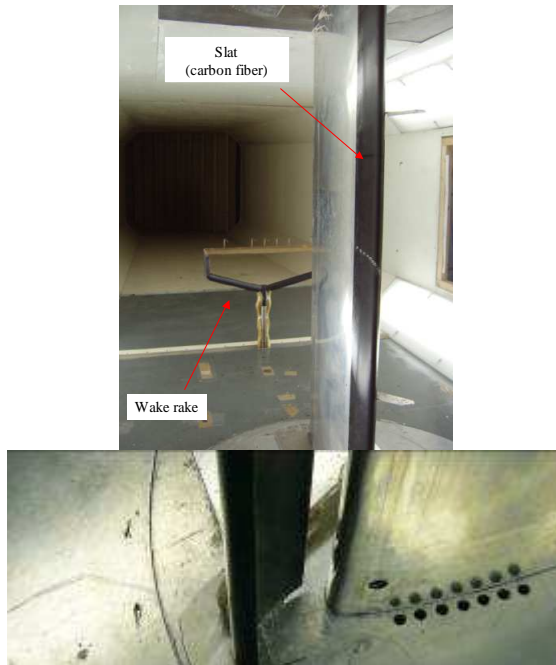
Configurations		Overlap (%)			
		3	1.9	1	0
Gap (%)	1.7	f1	f2	f3	f4
	1.8	f5	f6	f7	f8
	1.88	f9	f10	f11	f12
	2	f13	f14	f15	f16
$Cl_{max}$ ( $\alpha=18.5^\circ$ )		Overlap (%)			
		3	1.9	1	0
Gap (%)	1.7	1.32	4.01	4.03	3.97
	1.8	3.83	3.95	3.99	3.93
	1.88	3.87	4	4.02	3.87
	2	3.92	4	3.98	3.88

Table 5: Analysed flap configurations and  $Cl_{max}$  characteristics.

Careful examination of results and the lift curves, led to the selection of several possible solutions. Configuration  $f10$ ,  $f11$  and  $f14$  (see table 5) have been selected. The  $f11$  configuration is slightly more performing because of the lower flap overlap value, but in the  $f14$  configuration the hinge position is closer to the airfoil's chord. Therefore the  $f14$  configuration has been preferred. Similar numerical optimisation has been performed for the slat position.

## 5. 2-D WIND TUNNEL TESTS

After deep numerical analysis, experimental tests have been performed on a 2D model. All tests have been performed in the main DIAS wind tunnel. In order to experimentally obtain aerodynamic characteristics and to validate numerical results, extensive tests have been performed on a 2D model of three component G1-3F airfoil. Tests have been also focused on the optimisation of elements position. This model has been made by using an aluminium flap and main component and a carbon fiber slat to avoid high deformation of slat at the centre of the model where pressure taps are placed. The model with a retracted chord of about 55 cm mounted in the test section is shown in fig. 15



*Fig. 15 : 2-D wind tunnel test model of G1-3F 3-component airfoil*

### **5.1 Cruise retracted configuration**

The first tests were conducted on the retracted cruise configuration (see that one in the upper part of fig. 14). Test Reynolds number was 1.3 million. Fig. 16 shows some flow visualization made with fluorescent oil on airfoil upper surface at  $\alpha=0$  and 8 deg.. It can be observed that at low angles of attack the geometrical discontinuity on the airfoil upper surface due to the slat trailing edge causes anticipated transition. This discontinuity causes absence of laminar flow on main component upper surface. Anticipate transition will cause higher airfoil drag than expected by numerical calculations.

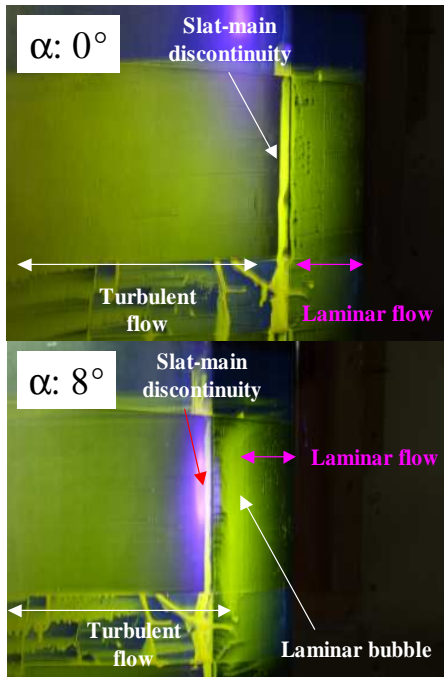


*Fig. 16 : Flow visualization on airfoil upper surface(cruise configuration)*

Fig. 17 shows the comparison between the numerical and the experimental results in terms of airfoil pressure coefficient distribution. It can be observed the local difference due to slat-main component geometrical discontinuity. Fig. 18 show the comparisons between numerical and experimental analysis in terms of lift and drag coefficient. A good agreement between numerical and experimental results can be observed. In the drag polar curve there is a difference between numerical and experimental data because of a low under-predicted numerical data and probably an over-estimated experimental data arising from the above mentioned discontinuity.

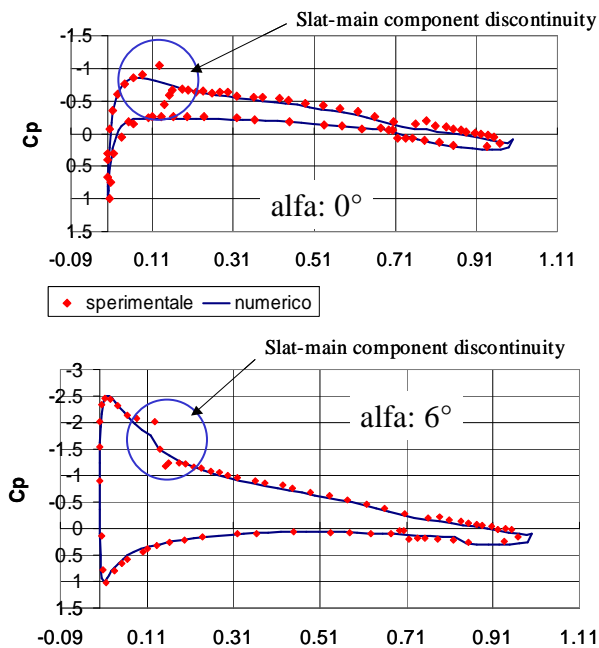


Fig. 17 : Pressure coefficient distribution. Cruise condition. Numerical and experimental comparison.

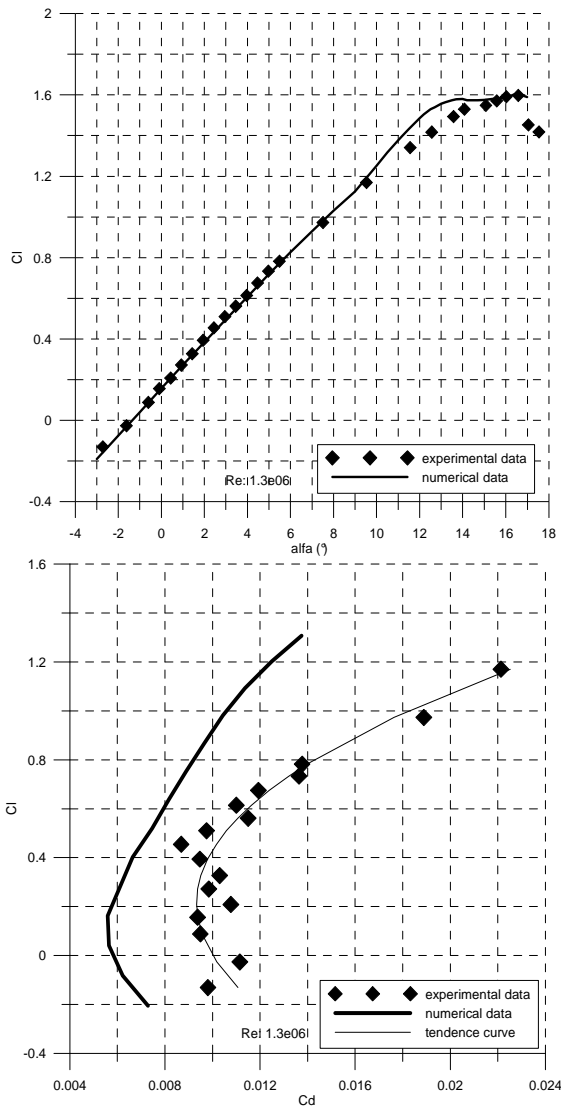


Fig. 18 : Cruise configuration. 2-D experimental and numerical comparison. Lift curve (left) drag polar (right)

## 5.2 Landing configuration

Landing configuration shown in fig. 14 (lower part) has been also extensively tested. Starting from final configuration chosen after detailed numerical analysis, an experimental optimisation has been carried out acting separately on slat and flap position; the same definitions of gap and overlap used for the numerical analysis have been here applied. In the case of the slat different configurations have been analysed at angle of attack of  $15^\circ$ . From table 6 it can be seen that maximum lift coefficient for landing configuration is dependent on slat gap and overlap.

Configuration	Gap %	Overlap %	alfa (°)	Cl
s1	3.37	4.12	15.37	3.7
s2	5.1	3.9	15.5	3.3
s3	6.1	4.44	15.46	3.5
s4	2.22	2.56	15.36	3.22

*Table 6 : Slat position experimental optimisation*

Configuration	Gap %	Overlap %
p1	1.18	2.3
p2	1.35	3.4
p3	1.35	3.2
p4	1.35	1.96
p5	1.35	3.73

*Table 7 : Flap position experimental optimisation*

In the same way different flap configurations have been considered (table 7) with a deflection of  $39^\circ$ ; Fig. 19 shows the comparison between the different lift coefficient curves measured through wind-tunnel test of each configuration. From fig. 19 it can be seen that experimental results show that a 2-D maximum lift coefficient higher than 4.0. Fig. 20 shows the distribution of pressure coefficient at  $12^\circ$  and  $24^\circ$  angle of attack. Fig. 21 shows the lift coefficient curve of the optimal landing configuration; in the same figure the effect of the flap deflection angle is shown.

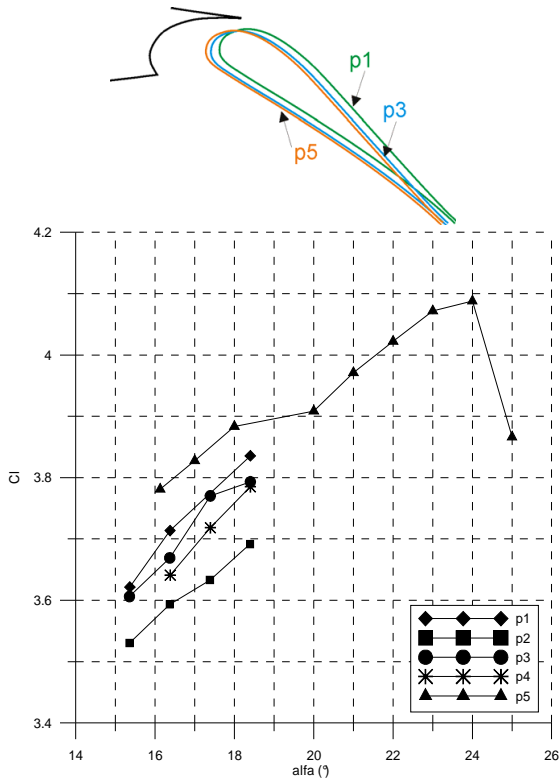


Fig. 19 : Slotted flap position optimisation.



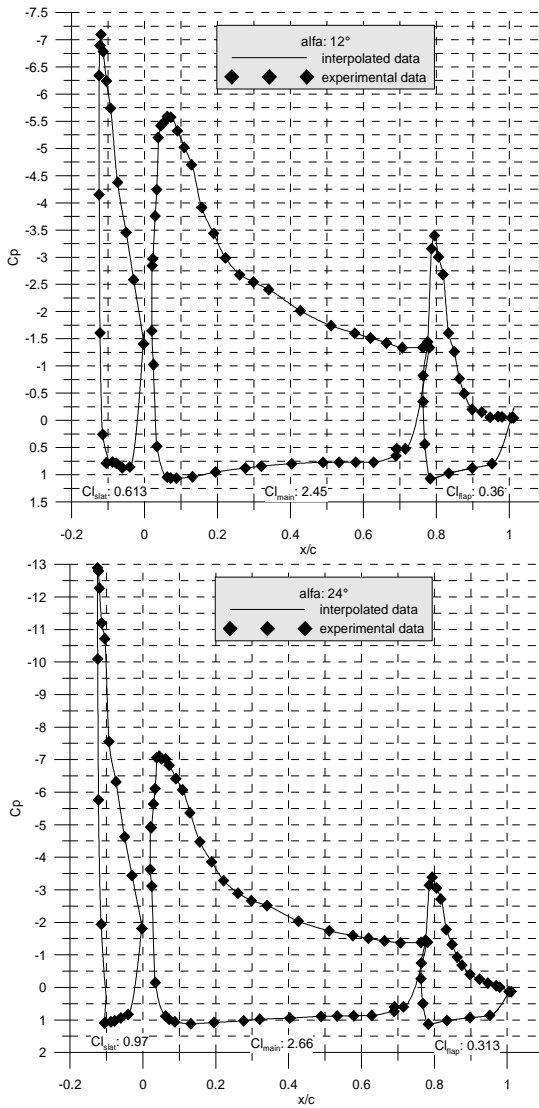


Fig. 20 : Pressure distribution measured on final landing configuration.

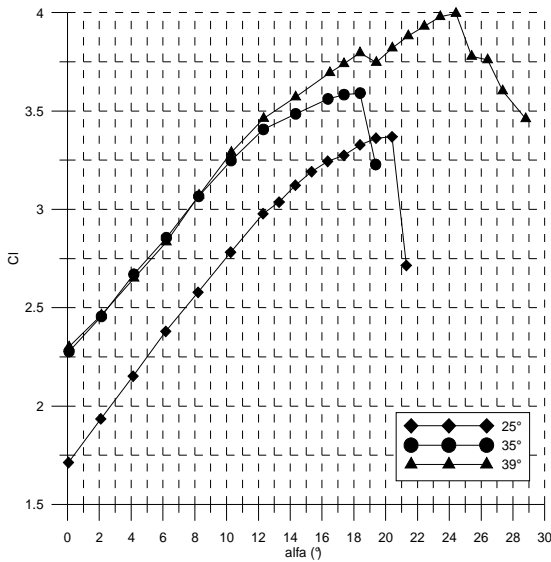


Fig. 21 : Lift curve for different flap deflections.

### 6. 3-D WIND TUNNEL TESTS ON AIRCRAFT MODEL

In order to verify the 3D aircraft stall characteristics, wind-tunnel tests have been performed on a 1:6.8 scaled aircraft model. These tests have been performed both on cruise and landing configurations, measuring the forces acting on the model with a strain gauge balance. All tests have been performed with a Reynolds number of 0.6 million and with an imposed transition to eliminate the critical problem, at this Reynolds number, of the laminar bubbles. In fig. 22 a picture of the aircraft model is represented.



Fig. 22 : 3-D aircraft model, cruise configuration

### 6.1 Cruise (clean) configuration tests

Fig. 23 shows the results in terms of lift coefficient curve and moment coefficient curve. Different horizontal tail deflection angles have been used to verify the aircraft trim capability. Wing-body maximum lift coefficient of 1.40 has been measured for the aircraft. Trimmed stall value of about 1.40 is expected. The flight maximum lift coefficient should have an increase due to Reynolds number effect. A  $CL_{max}$  of 1.50 is expected for the trimmed aircraft in clean configuration. Fig. 23B shows that the aircraft can be easily trimmed with reasonable stabilator deflections. The stall should be achieved with a stabilator deflection  $\delta_s = -10^\circ$ .

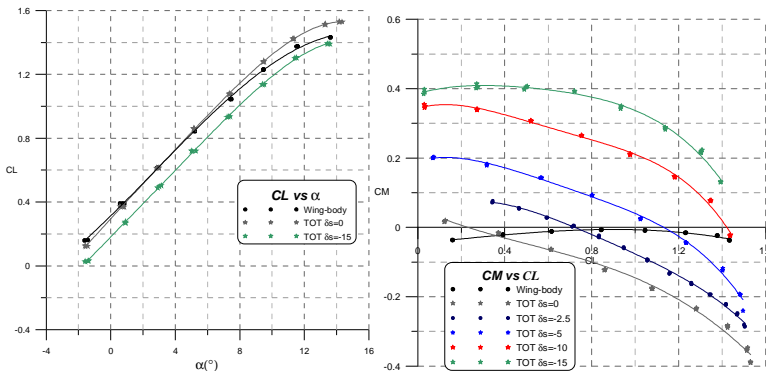
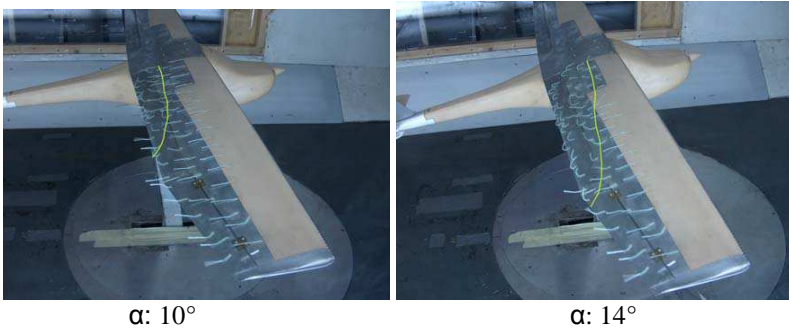


Fig. 23 : 3-D aircraft model, cruise configuration. Lift (A) and moment coefficient (B) curves.

After forces measurement, a set of tufts visualization tests have been conducted in order to analyse stall path (Fig. 24). Increasing the angle of attack, the separated zone increases but the flow at the wing tip zone remains attached; this means that the aileron's effectiveness will not be influenced by flow separation.

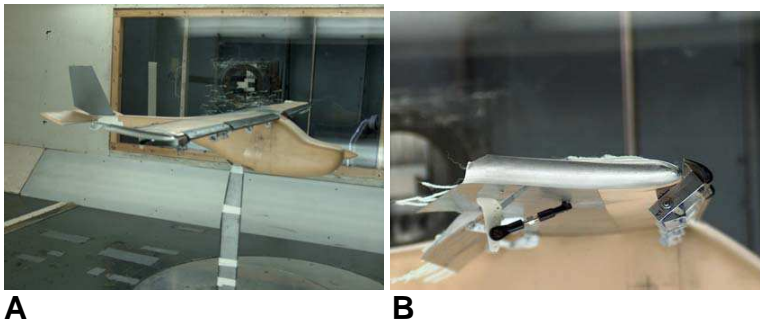


*Fig. 24 : 3-D aircraft model, cruise configuration. Stall path visualisation through tufts.*

## 6.2 Landing configuration tests

In fig. 25 (A,B) the model in full-flap and slat configuration is shown. The slat, made in carbon fiber (due to very small dimension and relatively high loads) has been added at wing leading edge. Fig. 25 shows the aircraft model in landing configuration. The flaps and the ailerons have been carried out as mobile parts. The carbon fiber slat has been thought as an add-on solution, it has been made and mounted ahead of the original wing leading edge (in order to realize the slat effect of delaying upper surface flow separation). Many difficulties have been encountered in realizing and setting in the right position this slat because of its very thin shape and small dimensions. Fig. 26 shows the results of the tests; different horizontal tail deflection angles have been used to verify the aircraft trim capability in landing configuration. The measured  $CL_{max}$  of the wing-body configuration with full-flap (deflected  $39^\circ$ ) and slat open at Reynolds number of about 0.6 million based on wing chord is about 3.2, see fig. 26-A. Considering stabilator deflection necessary to trim the aircraft in landing configuration a maximum lift coefficient of about 3.1 has been measured (fig. 26-A, deflection  $\delta_s = -25^\circ$ ). Fig. 26-B shows that this lift coefficient can be achieved in trimmed conditions. The stabilator deflection is sufficient to ensure aircraft equilibrium up to  $20^\circ$  angle of attack. The aircraft show

positive stability up to stall and post-stall conditions. Considering the landing flight Reynolds number of about 1.3 million, a maximum lift coefficient for the complete aircraft of about 3.4-3.5 is not an optimistic estimation. The obtained value of about  $3.1 \div 3.2$  confirm all predictions and estimations of performed design activities. The measured airfoil maximum lift coefficient in landing conditions of 4.0 (see par. 5.2 ), taking into account that only 60% of the wing span is covered by flap, lead to an expected value of about 3.2 for the complete aircraft. The trimmed experimentally obtained value  $CL_{max}=3.1$  reported above is in good agreement with expectations. This last consideration confirm the good quality of the performed design (also 3D wing planform shape and fuselage shape).



**A** **B**  
 Fig. 25 : 3-D aircraft model, landing configuration. Particular of the model.

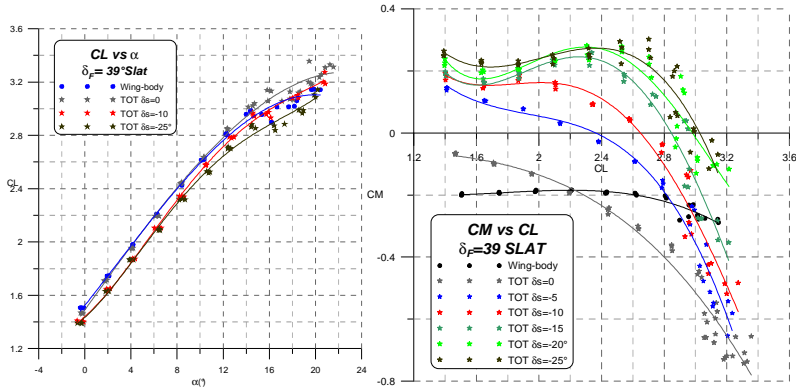
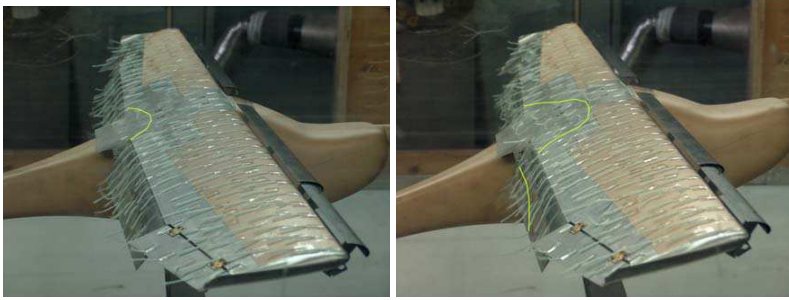


Fig. 26 : 3-D aircraft model, landing configuration. Lift curve (A) and Moment curves (B)

The stall path of full-flap configuration was measured and visualized. As shown in fig. 27 the flow separation starts close to the wing root. At an angle of attack of 19 deg. Only a small portion of the slotted flap is interested by separated flow. Flow on the aileron is completely attached.

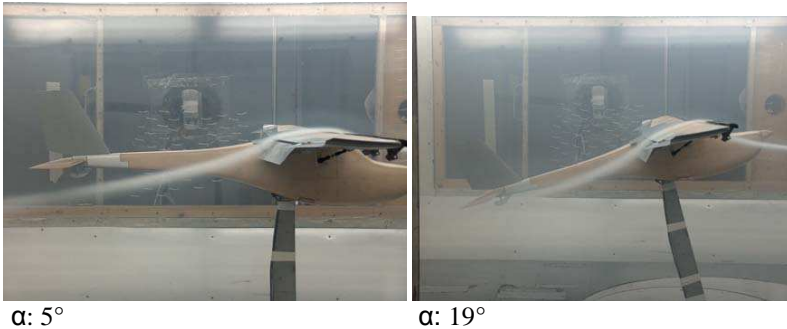


$\alpha: 12^\circ$

$\alpha: 19^\circ$

*Fig. 27 : 3-D aircraft model, landing configuration. Stall path visualisation with tufts.*

In order to evaluate the wake location and to check the distance of the horizontal tail from wing wake, a visualization has been performed by smoke visualization technique. Fig. 28 shows the results at the angle of attack of  $5^\circ$  and  $19^\circ$ . For low values of the angle of attack the flow is completely attached on the flap and the wake distance from the horizontal tail is considerable. When the angle of attack increases, the flow remains attached on the flap but the distance between the wake and the horizontal tail decreases. At the stall condition ( $\alpha=19^\circ$ ), the wake is very close to the horizontal tail. It should be considered that the wake is not caused by massive flow separation, even at this high angles conditions because flow separation on the flap is quite limited. Consequently the horizontal tail should not be subject to excessive vibrations due to the turbulent wing wake.



$\alpha: 5^\circ$   $\alpha: 19^\circ$   
 Fig. 28 : 3-D aircraft model, landing configuration. Wing wake visualisation.

## CONCLUSIONS

Many results of a deep experimental and numerical design activity focused on high-lift system design for a light aircraft has been presented. The obtained experimental results show that a good high-lift system has been designed and the aircraft should achieve very good STOL characteristics.

## ACKNOWLEDGEMENTS

The authors want to thank Aerosoft S.r.l. and Italian Law 297 for the financing of this research project.

## REFERENCES

- [1] Coiro D.P., Nicolosi F., De Marco A., Genito N. and Figliolia S. “*Design of a Low Cost Easy-to-Fly STOL Ultralight Aircraft In Composite Material*” Acta Polytechnica, Vol. 45 no. 4/2005, pp. 73-80 ; ISSN 1210-2709 (Presented at 4<sup>th</sup> Advanced Engineering Design Conference, Glasgow, Sept. 2004)
- [2] D.P. Coiro, F. Nicolosi, S. Figliolia, F. Grasso , A. De Marco, N. Genito, “*Design of a S.T.O.L. Ultra Light Aircraft in Composite Material*”, XVIII Congresso Nazionale AIDAA, 19-22 settembre 2005, Volterra (Pi).
- [3] Roskam, J.: Part I-II and IV: Preliminary Sizing of Airplanes. Lawrence, Kansas 66044, U.S.A.: 120 East 9th Street, Suite 2, DARcorporation, 1997.
- [4] Francesco Grasso, “Progetto e analisi di un profilo alare multicomponente per applicazioni S.T.O.L.”, Aerospace Engineering Thesis, Università degli Studi di Napoli Federico II, Dipartimento di Ingegneria Aerospaziale, Academic Year 2004-2005 (Supervisor: F. Nicolosi).

- [5] Coiro, D. P. – Nicolosi, F.: “Aerodynamics, Dynamics and Performance Prediction of Sailplanes and Light Aircraft”. Technical Soaring, 24, No. 2, April 2000.
- [6] Drela, “XFOIL 6.94 User Guide”, MIT Aero & Astro, Dec 2001.
- [7] Coiro, D.P. and de Nicola, C. “Prediction of Aerodynamic Performance of Airfoils in Low Reynolds Number Flows,” Low Reynolds Number Aerodynamics Conference, NotreDame, USA. 1989
- [8] Coiro D.P. and Dini P.: "*Stall and Post-Stall Performance Prediction of Advanced Wind-turbine Airfoils*" XII AIDAA Congress, Como(ITALY) 1993.
- [9] Coiro D.P. and Dini P., "*Prediction of Airfoil Stall over Wind-Turbine Airfoils*", FTEC '97 Congress, YogJakarta, Indonesia, July 1997.
- [10] Besnard, Schimtz, Cebeci, “Two dimensional Aircraft High Lift System Design and Optimization”, AIAA 98-0123, 1998.
- [11] Kim, Alonso, Jameson, “Design Optimization of High Lift Configurations using a Viscous Adjoint-Based Method”, AIAA 2002.
- [12] Egglestone, McKinney, “Development of a New Flap for a Light Utility Transport Aircraft”, Canadian Aeronautic and Space Journal, December 2002.
- [13] Drela, “A User’s Guide to MSES 2.9”, MIT Computational Aerospace Sciences Laboratory, October 1995.



## **Horizontal Axis Tidal Current Turbine: Numerical and Experimental Investigations**

D.P. Coiro, U. Maisto, F. Scherillo, S. Melone, F. Grasso

*Department of Aeronautical Engineering (DPA), University of Naples  
"Federico II" - Naples, Italy*

*Tel. +390817683322; Fax. +390817683622*

*coiro@unina.it*

### ABSTRACT

Marine current energy is one of the most interesting renewable and clean energy resources that have been less exploited respect to wind energy. Only in Europe this type of energy is available for 75 millions of KiloWatts and in terms of exploitable energy the amount is about 50 milliards of KiloWattHour. In the last years, the realization of horizontal axis turbine for the exploitation of the tidal currents is having, to world-wide level, a considerable increment. Many are the societies and the consortia that have decided to invest in such type of energetic source.

The present paper provides a summary of the work done at the Department of Aeronautical Engineering (DPA) of the University of Naples "Federico II" regarding the numerical and experimental investigations of a scaled model of an horizontal axis hydro turbines designed to harness energy from marine tidal currents.

The horizontal axis hydro turbine has been designed and analyzed using numerical codes available at DPA. Among these codes, some were already available at DPA and were based on standard Glauert's blade element theory, modified following Prandtl's theory and the "Higher Order Correction" method, while a new unsteady code, based on vortex lifting line theory, has been developed and now is under validation.

The wind turbine has been designed to work at a specific Tip Speed Ratio (TSR) and particular effort has been put in order to avoid the cavitation on the blade surface.

The blades are composed by airfoils with decreasing thickness from root to tip to accommodate both structural and aerodynamic needs.

Airfoil design and selection are based on:

- appropriate design Reynolds number;
- airfoil thickness, according to the amount of centrifugal stiffening and desired blade rigidity;

- roughness insensitivity, most important for stall regulated wind turbines;
- low drag, not as important for small wind turbines because of passive over speed control and smaller relative influence of drag on performance;
- high-lift root airfoil to minimize inboard solidity and enhanced starting torque.

Experimental investigations have been carried out into the water towing tank at the Naval Engineering Department of the University of Naples “Federico II” and attention has been paid in order to reproduce the real operating conditions of the full scale turbine during the towing tank tests.

### Nomenclature

$P$	Turbine Output Power	$Cl_{max}$	Max Airfoil Lift Coefficient
$R$	Rotor Radius	$TSR = \frac{\Omega R}{V_{\infty}}$	Tip Speed Ratio
$\Omega$	Rotational Speed	$CP = \frac{P}{0.5\rho V_{\infty}^3 S}$	Power Coefficient
$V_{\infty}$	Free Stream Velocity	$c_p = \frac{p - P_{\infty}}{0.5\rho V^2}$	Pressure Coefficient
$V = \sqrt{V_{\infty}^2 + (\Omega R)^2}$	Local Velocity	$\sigma_v = \frac{P_s - P_v}{0.5\rho V^2}$	Cavitation Number
$S$	Rotor Frontal Area		
$\rho$	Fluid Density		
$P_s = P_{\infty} + \rho gh$	Static Pressure		
$h$	Blade Tip Depth		
$P_v$	Water Vapor Pressure		
$P_{\infty}$	Atmospheric Pressure		

## 1 Introduction

Marine or river current turbines, due to the water’s greater energy density than air can be much smaller than their wind counterparts.

Furthermore, tidal power is much more reliable than wind power due to its predictable nature thus making it a better source of electrical energy for feeding the electrical grid.

In the present work it will be described the preliminary design phase of a tidal turbine rated approximately at 300 kW with a marine current in the range of 2~3 m/s with the hub supposed to be set at 20 meters below the water surface.

In this phase an experimental model has been designed, built, instrumented and tested in the towing tank of the Naval Engineering Department of the University of Naples Federico II. The rotor has been designed in order to work at the same Tip Speed Ratio of the 300 kW turbine.

During the experimental tests set up, particular attention has been paid to simulate the same cavitation number of the real scale case.

## 2 Experimental model: Rotor design Phase

As it is well known, two rotors with the same geometrical characteristics but with different diameter will produce the same non-dimensional forces if they work at the same TSR. According to this concept the experimental model rotor has been designed to work at the same design TSR of the full scale rotor. The TSR has been chosen taking in account that higher TSR value means higher tip tangential velocity and consequently lower cavitation number. We believe that a good compromise is a design TSR around 3.5.

The dimension of full scale model has been supposed to be: *Rotor radius*  $\sim 5.5$  m; *Minimal hub depth*  $\sim 15$  m. Therefore the minimal blade tip depth during the rotation will be  $h=10$  m. Using these data, it is possible to estimate the cavitation number at the blade tip of the full scale model.

Evaluating the cavitation number for a marine current velocity of 2.5 m/s and a water temperature of 10 °C we obtain  $\sigma_v=4.1$ . It is possible to obtain a similar cavitation number for the scaled model dipping the hub of the scaled model of 1.5 m under the water level and having a towing tank speed of  $\sim 2$  m/s.

### 2.1 Airfoil Design

The blades are composed by airfoils with decreasing thickness from root to tip to accommodate both structural and aerodynamic needs. In order to have thicker airfoil at the root and thinner at the tip, it has been chosen to use two different airfoils.

Between 15% and 35% of the blade radius it has been chosen an *ad hoc* designed thick airfoil (Fig 1), while, for the remaining section of the blade, an airfoil (named GT1), obtained modifying the S805 airfoil, has been used (Fig 2). The airfoils are shown deformed for confidential reason.

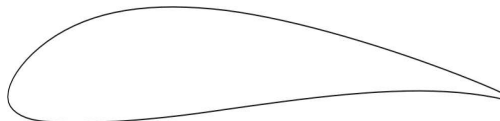


Figure - 1 Root airfoil (deformed)

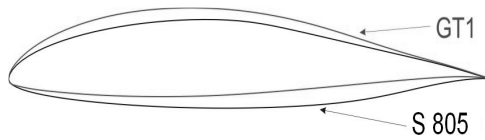


Figure 2 - GT1 tip modified airfoil (deformed)

Both the airfoils have been chosen and designed to have high efficiency at their design angles of attack and Reynolds number, estimated to be about 500000 at the blade tip and 200000 at the blade root.

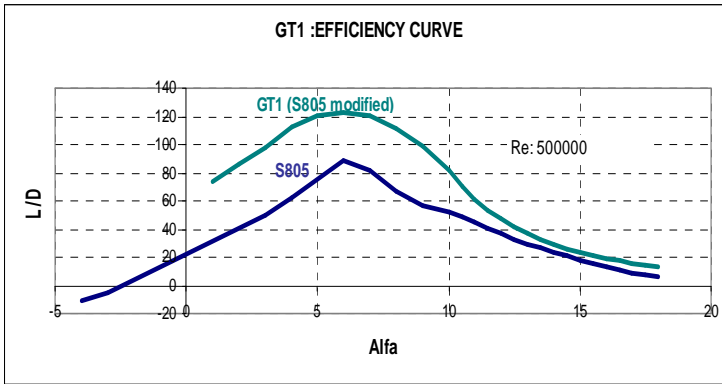


Figure 3 - GT1 efficiency curve

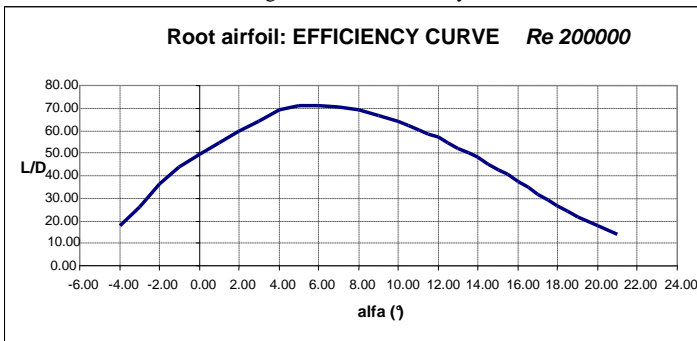


Figure 4 – Root airfoil: efficiency curve

The design of the blade tip airfoil has been performed in order to avoid cavitation. Cavitation occurs when the absolute value of the local pressure coefficient on the airfoil,  $|c_p|$ , is greater than the cavitation number,  $\sigma_v$ . According to this, the blade tip airfoil has been designed to obtain  $|c_p| < \sigma_v$ .

for the pressure distribution corresponding to  $Cl_{max}$  where high negative pressure peak is reached. An example of pressure modifications at design angle of attack is reported in te figure 4a.

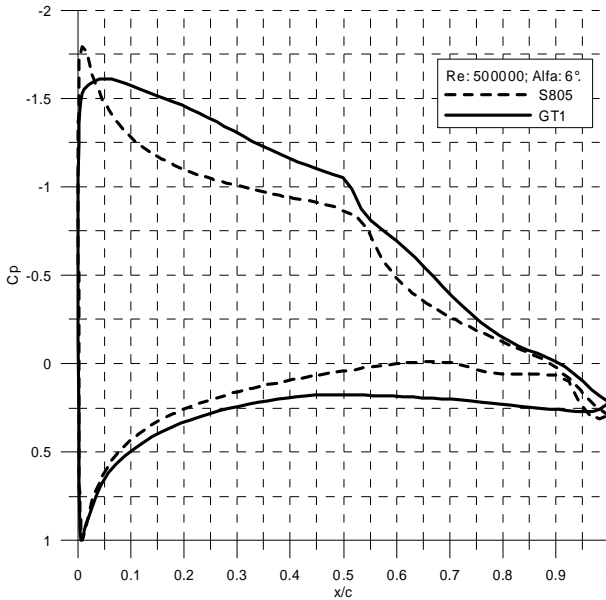


Figure 4a: Pressure coefficient distribution for the original and modified airfoil

## Blade Design

The blades have been designed using a numerical code developed at DPA. The code is based on the classical Glauert's theory modified including real viscous behaviour of airfoils and higher order correction terms (finite span, hub loss, etc.)

The code input allows the user to supply the desired angle of attack of each section and the TSR design point, and, as output, it supplies the chord distribution and the twist distribution along the blade, see figures 5 and 6 (real values are not shown for confidential reasons). There is also the possibility to perform a multi-point design. The final rotor diameter is .8 m and the area is .5 m<sup>2</sup> leading to a global rotor solidity of .2.

Using both chord and twist distributions, a complete numerical analysis, to obtain the characteristic curves of the turbine, has been performed. It's important to remark that it has been preferred to use a linear chord distribution instead of the optimum one obtained from the design phase because it is much easier to build. In any case, the two planform shapes were both numerically analysed and the comparison suggests that the

differences between optimal chord distribution and the linear one, is negligible.

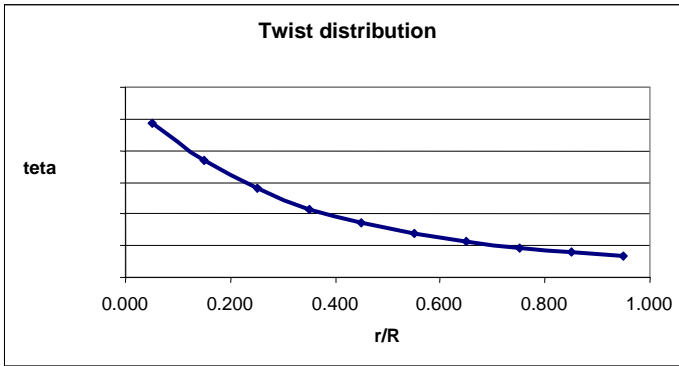


Figure 5 - Blade Twist distribution

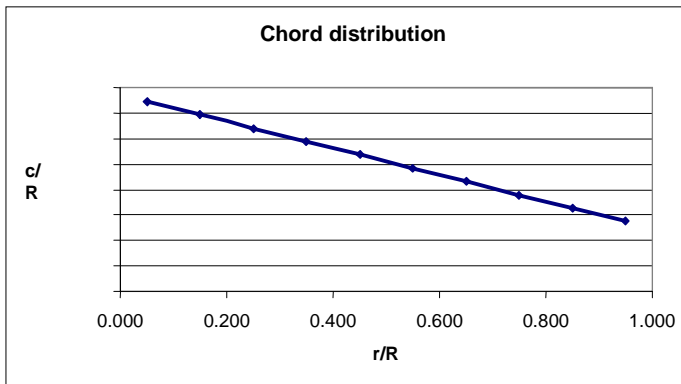


Figure 6 - Blade Chord distribution

In the figures 7 and 8, the Power Coefficient  $C_P$  vs TSR and the Power vs Rpm, at different water speeds, are showed. As it is possible to see from the figures, it looks that the turbine shows a good behaviour not only at the design TSR but also at higher TSR values ( $TSR=3\div 5$ ). This has been one of the main guideline of the proposed design: renouncing a bit in terms of maximum efficiency in favour of a larger extent of TSR at which the rotor shows its maximum value.

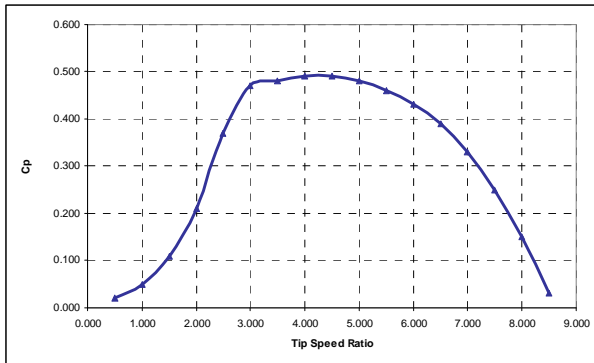


Figure 7 - Power coefficient vs Tip Speed Ratio (numerical)

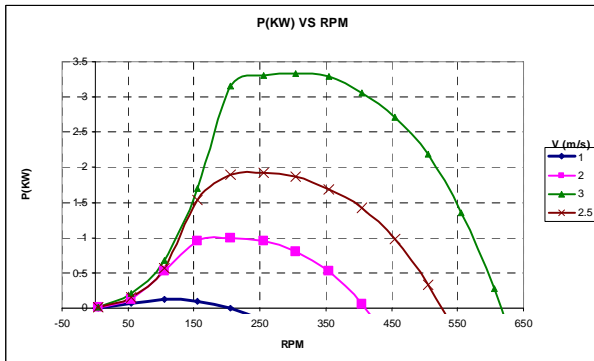


Figure 8 - Power vs Rpm varying towing tank speed (numerical)

### 3 Equipment and experimental setup

The blades have been manufactured in aluminium using CNC machines and, as showed in Fig 9, it has been possible to set different pitch angles of the blades.

The whole experimental equipment has been CAD designed and it has been verified from a structural point of view through a finite element analysis (Fig 10).

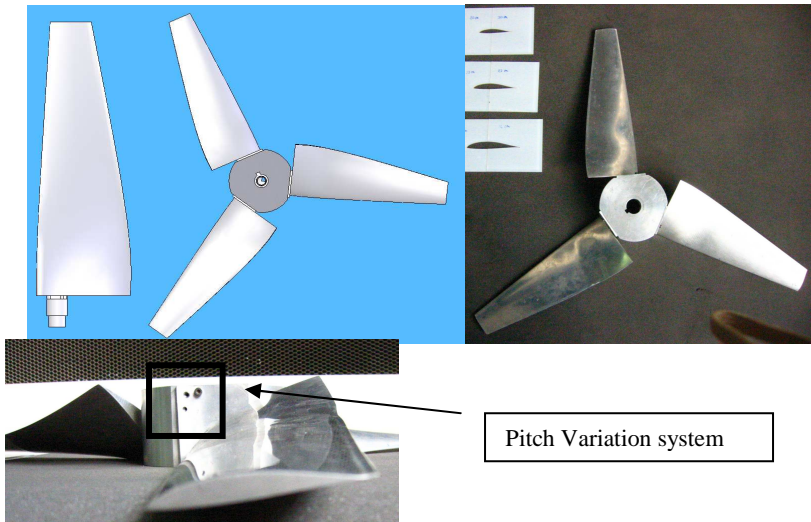


Figure - 9 - The rotor: a) CAD model; b) Real model with airfoils template; c) Pitch variation system

Downstream the rotor, a box has been designed to hold the complete measurement equipment (Fig 10).

The motion is transmitted to an engine through a 90 degree gear box with ratio 1:1. Finally a two steps gear box of ratio 1:16 brings the rotational speed to a value suitable for the engine. This is an electronically controlled asynchronous motor/generator that is capable to maintain a prefixed rotational speed. So the user can set a specific speed and the engine maintains that speed independently on the needed torque or power (i.e. it can behave like a motor or like a generator). In the experiments the engine worked as an *intelligent* brake: in particular it acted as a standard resistive load on the stable branch of the power curve (high TSR) while it acted as a perfect controllable brake on the instable branch of the power curve (low TSR). The torque-meter was specifically modified to work in the water. It had a full scale range of 226 Nm (2,000 lbf-in) and an accuracy of  $\pm 0.1\%$ FS. It needed air pressure to prevent entering the water inside the case. The torque-meter was also equipped with a rotational speed pick-up and it has been mounted floating. Finally, a load cell with 500 kN FS was installed at the end of the transmission shaft to measure compressive or traction loads produced by the rotor, see figure 10. The rotor hub has been set at 1.5 meter below the water surface.



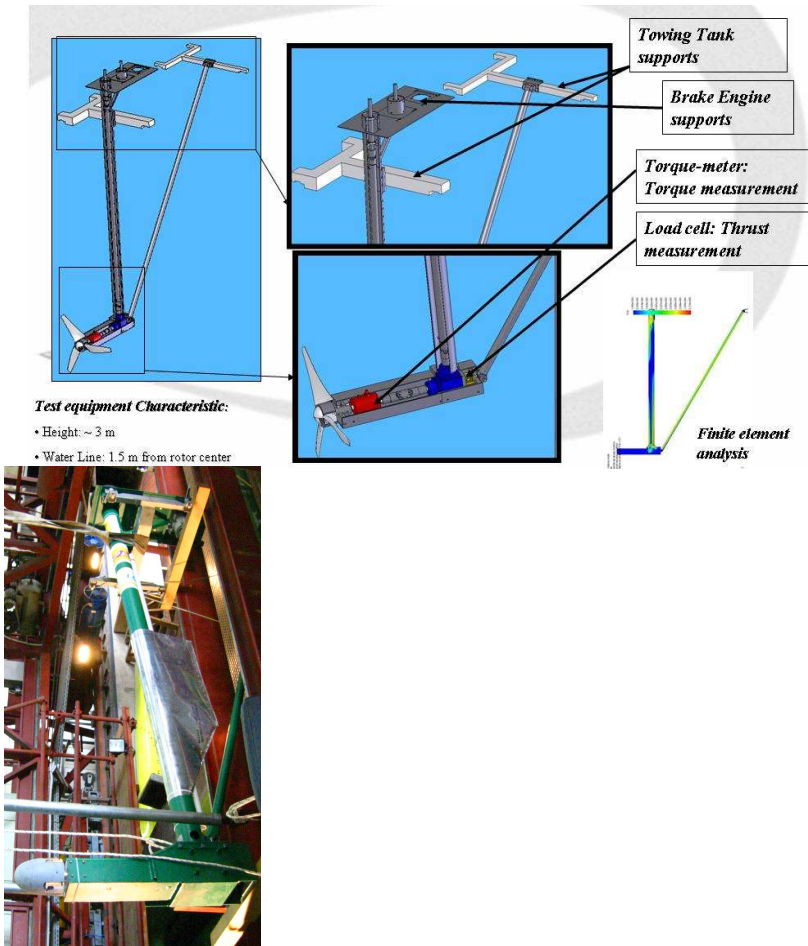


Figure 10 - Experimental equipment

#### 4 Experimental tests

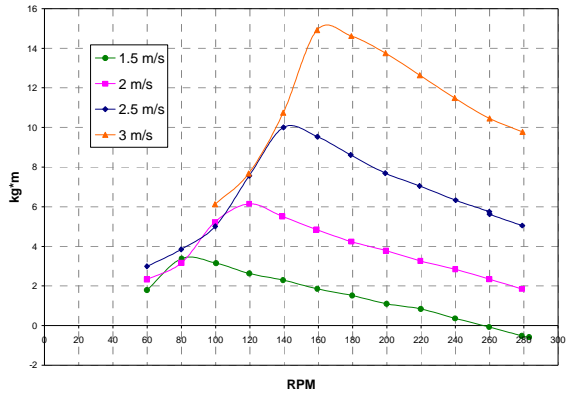
The experimental tests have been carried out at the Naval Department's Towing Tank of the University of Naples Federico II (Fig 11)



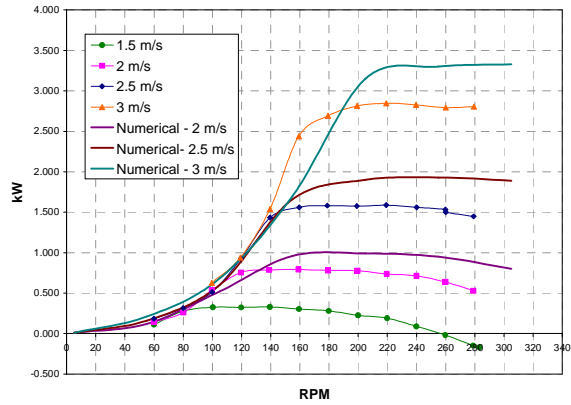
Figure 11 - Towing Tank, Turbine ready to be installed

The towing tank main dimensions are: 135.5m x 9.0m x 4.5m (depth). The experimental tests have been carried out at different towing speeds. During the tests a range of velocities between 1.5 m/s and 3.5 m/s and different blade's pitches ( $-4^\circ$ ,  $0$ ,  $4$ ) have been investigated (negative pitch: toward stall). In the following figures a comparison between numerical results and experimental results at the blade pitch of 0 degrees and at different speeds are shown; figure 14a shows measured torque while figure 14b illustrates the differences between the numerical evaluated power with measured data. Considering that the numerical curves are based only on numerically evaluated airfoil coefficients and that there is a little loss due to the bearing holding the rotor, the agreement is acceptable. Figure 12c is referred to a water speed of 2 m/s and shows the measured power, the numerical one and the power derived from the measured thrust applying the disk actuator theory and using the theoretical value of the speed in the far wake downstream. The curve indicated as *Exp. From Thrust* has been obtained by the theory reducing the derived power of 20% to take in account the loss connected to the real streamtube which is different from the theoretical one. Figure 12d shows the measured thrust at different water speed. The efficiency (also named power coefficient) at the nominal pitch and for different water speed is shown in figure 13a while the pitch variation effect is illustrated in figure 13b. The collapsing of efficiency curve at different water speed is an indication of the accuracy of data. Nevertheless is worth to note that there is a little increment in the power coefficient at higher water speed due to the increase of airfoil blade Reynolds number reducing then the drag coefficient.

Torque (Pitch 0°)



Power (Pitch 0°)



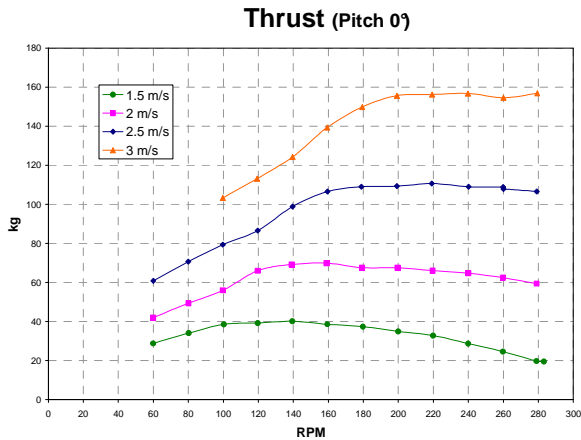
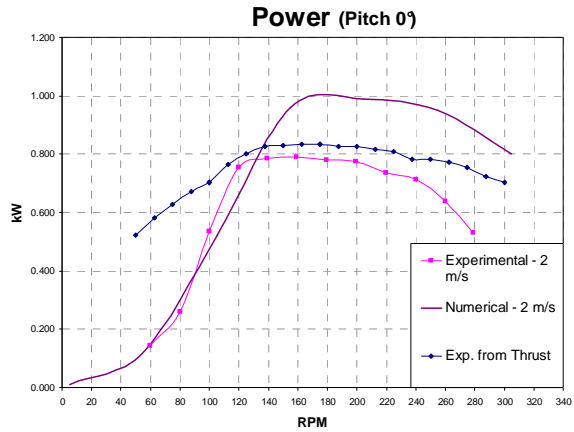


Figure 12: a) Experiments: Power; b) Numerical vs experiments: Power at different velocities; c) Power at V=2 m/s d) Experiments: Torque

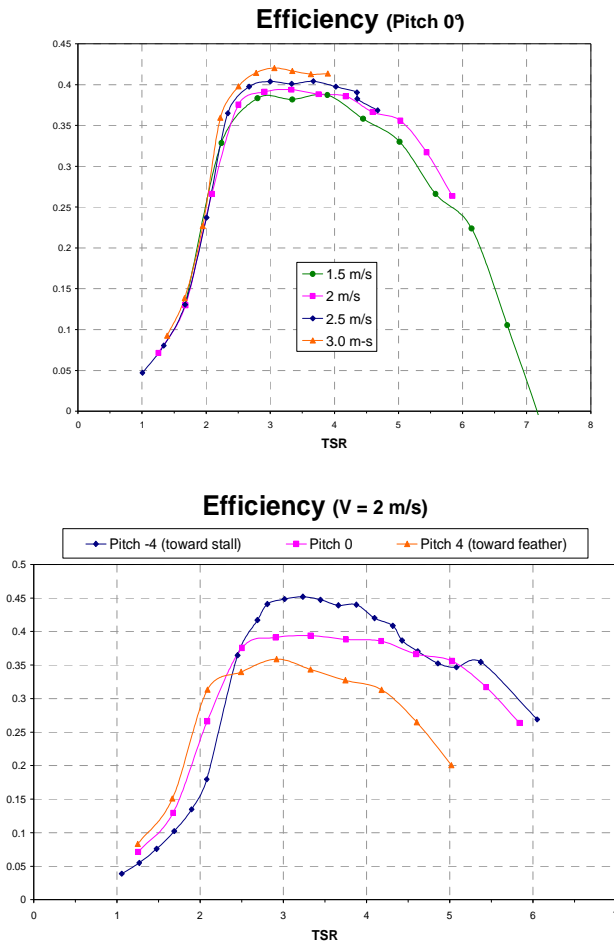


Figure 13: a) Experiments: Efficiency at different velocities; b) Experiments: Efficiency at different pitches

Figure 14a shows the torque variation in time at steady water speed of 2.5 m/s with turbine rotational speed of 200 rpm: it can be seen that the torque ripple is very small. The start-up of the rotor is illustrated in figure 14b that shows the variation of the rotor torque with time letting the rotor accelerate autonomously without any breaking load.

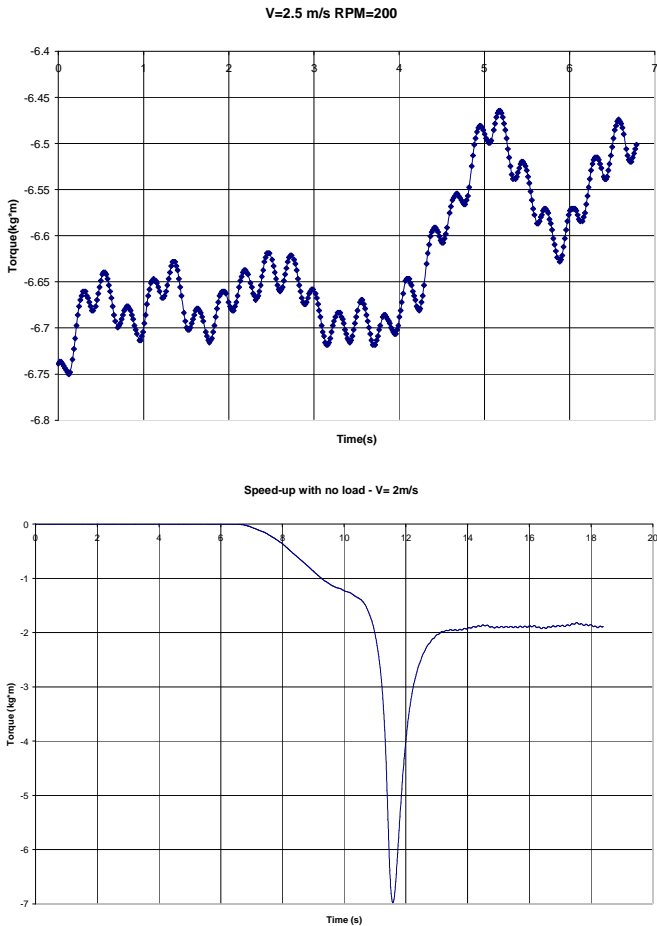


Figure 14: a) Experiments: Torque vs time; b) Experiments: Torque vs time at speed-up with no load

## 5 Conclusions

An horizontal axis hydro turbines has been designed to harness energy from marine tidal currents and a scaled model of it has been built and tested in the towing tank of the Department of Naval Engineering, University of Naples “Federico II”, reproducing the same cavitation number of the real

turbine. Turbine performances have first been predicted numerically by means of numerical codes based on standard Glauert's blade element theory modified *ad hoc*, and then they have been measured experimentally through several towing tank tests during which water speed, blade pitches and depth of rotor hub has been systematically varied. During the experimental tests, particular attention has been paid to simulate the same cavitation number and the same TSR of the real scale turbine that is expected to produce 300kW of clean electrical energy. The blades have two different airfoils for the root and the tip. Tip airfoil has been designed to avoid cavitation at the design working condition. The experimental data confirm that the turbine has good performances not only at the design TSR (3.5) but also for higher TSR values (TSR=3÷5) according to one of the main design requirements. Furthermore a maximum efficiency of 45% has been measured that can be considered an excellent value considering the small blade airfoils Reynolds numbers. This has been obtained with pitch equal to -4 degrees that, from another side, retards the speed-up of the turbine respect to the case with pitch=0 degree. It is also worth to mention that even with the tip blade set at only 20 cm from the water surface, the cavitation never appeared, satisfying also another of the design requirements.

### **Acknowledgements**

The authors would like to thank the staff of the Naval Engineering Department for the precious assistance during the towing tank experimental tests.

The project has been totally funded by MoliseInnovazione S.C.p.A in the framework of the GEM turbine project.

### **References**

1. Eggleston, D.M. and Stoddard, F.S., (1987), Wind Turbine Engineering Design, Van Nostrand Reinhold Company, New York.
2. Coiro, D.P. and de Nicola, C. (1989), Prediction of Aerodynamic Performance of Airfoils in Low Reynolds Number Flows, Low Reynolds Number Aerodynamics Conference, NotreDame, USA.
3. Coiro, D.P. and Dini P., Stall and Post-Stall Performance Prediction of Advanced Wind Turbine Airfoils, XII AIDAA National Congress, Como, July 1993.
4. Coiro, D.P. and Dini, P. (1997), The Prediction of Aerodynamic Stall Over Wind-Turbine Airfoils, International Conference on fluid and thermal energy conversion, Yogyakarta, Indonesia.

5. G. Cerbasi, Experimental Analysis of a Small Wind Turbine and Aerodynamic Design of a 5kW Rotor, Degree Thesis, University of Naples "Federico II", Department of Aeronautical Engineering, A.A. 2002/2003.
6. A. Nicoli, Aerodynamic Optimization and Wind Tunnel Tests of an Horizontal Axis Wind Turbine, Degree Thesis, University of Naples "Federico II", Department of Aeronautical Engineering, A.A. 2001/2002.



## Appendix B: Optfoil user's Manual

**Author:** Francesco Grasso

**Contacts:** [skyflash@inwind.it](mailto:skyflash@inwind.it), [francesco.grasso@unina.it](mailto:francesco.grasso@unina.it)

### Overview

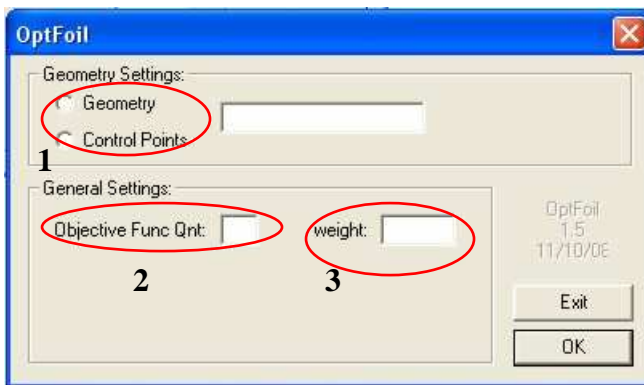
Optfoil is a numerical code created to design and optimize airfoil shape by using numerical optimization approach.

It is fully developed in FORTRAN 90. In order to guarantee an easy usage, an intuitive GUI is provided for any input parameter.

### System Requirements

No particular requirements are necessary to use Optfoil; just the operative system should be a Windows OS (Windows98, 2000, XP, Vista).

### Input Settings

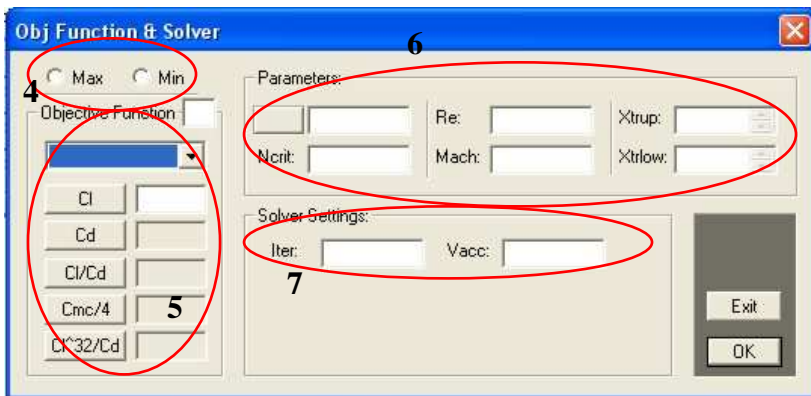


**1) Geometry Settings:** the user should provide the coordinates of the geometry to be used as initial configuration. No particular format rules are necessary; just two columns with “x” and “y” coordinates starting from the trailing edge, passing through the leading edge, to the trailing edge, both in clockwise or in counter-clockwise directions. In order to help the user and reduce the number of parameters to prescribe, during the design process, the same number of points and the same distribution density of the initial geometry is used.

Alternatively, the user can prescribe an initial set of control points; in this case the file should be named “control.txt” and two columns with “x” and “y” positions of 13 control points should be assigned in counter-clockwise direction. In any case a geometry file should be indicated in order to set number of coordinates and their distribution

**2) Objective Function Quantity:** Optfoil can optimize airfoil shape also in multi-objective problems. The user should prescribe how many objective functions will be specified.

**3) Weight:** in case of multi-objective problems, a weighting factor should be specified in order to combine the single objective functions.

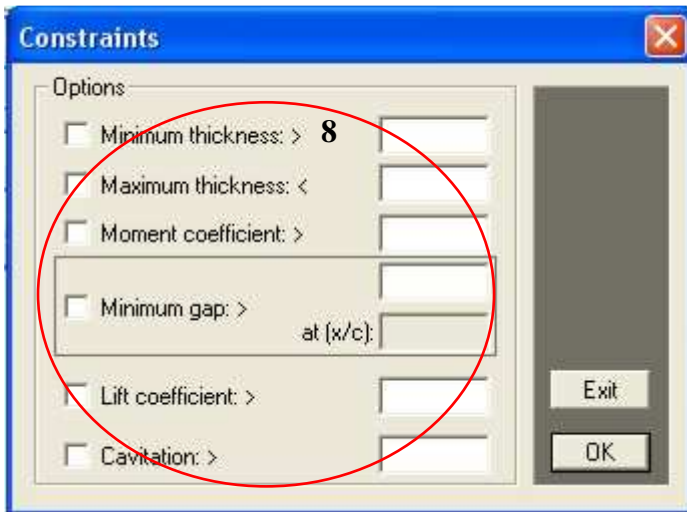


**4) Min/Max:** the user should choice if the design problem is a maximization or a minimization problem.

**5) Choice of objective function:** for each objective function, the user should choice which aerodynamic parameter is associated. By using Optfoil, lift coefficient, drag coefficient, aerodynamic efficiency (L/D) and endurance parameter ( $Cl^{3/2}/Cd$ ) are available as objective function.

**6) Parameters:** for each objective function, angle of attack, Reynolds number, Mach number, transition parameters and turbulence parameter “n” should be assigned.

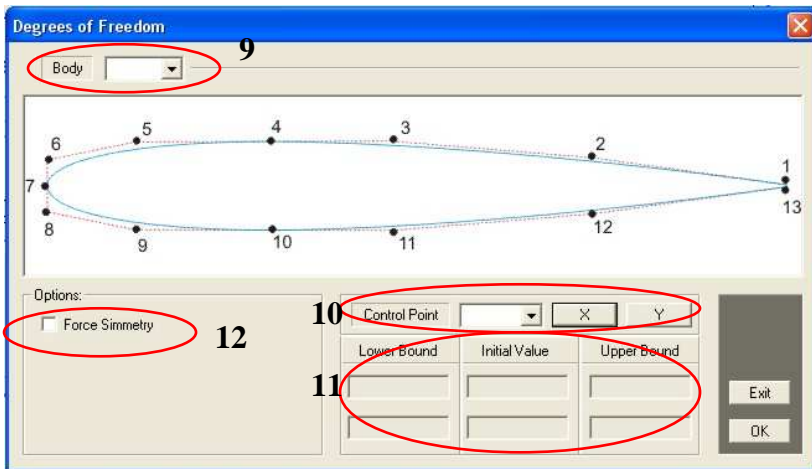
**7) Solver Settings:** Optfoil uses XFOil, TBVOR and MSES as aerodynamic solvers; in dependence of the aerodynamic solver, some parameters should be specified. More details are available in their user’s manuals.



**8) Constraints:** several constraints have been implemented in Optfoil, both geometrical and aerodynamic. Each one of these constraints can enabled or disabled in dependence of the specific design problem to solve, and for each one a bound

value can be prescribed. Here, a list of implemented constraints is indicated:

- Minimum thickness
- Maximum thickness
- Minimum gap
- Minimum moment coefficient
- Minimum lift coefficient
- Cavitation check



**9) Body:** parameter not used.

**10) Control points:** for each control point, it is possible to decide if to active it or not, if to active just the horizontal or the vertical displacement, or both two.

**11) Bounds:** for each active control point, its lower bound and upper bound should be provided. If the initial value is out of the prescribed bounds, Optfoil will set automatically the value equal to closer bound.

**12) Force symmetry:** it is possible to prescribe that the airfoil will be a symmetrical airfoil.

## Output Files

Several files are generated during the design process in order to allow the user to control each parameter modified during the process.

“**finalblade.txt**”: at the end of the design process, the coordinates of the optimal solution are stored in this file.

“**report.txt**”: the history of the objective function and constraints is stored in this file.

“**fort.7**”: this file contains information similar to those ones stored in “report.txt”, but with more details about the internal parameters of the optimization.

“**fort.41**”: for each tested configuration, a new set of control points is created; in this file these sets of control points are stored.

In addition to these files, each set of coordinates corresponding to tested configurations is stored in a single file (named with the current date and time).

## Optfoil internal structure

In this section the most important subroutines of Optfoil are briefly illustrated.

**main**: main program of Optfoil

**mainmenu**: subroutine for the control of the GUI regarding the initial choice about number of objective functions and input mode.

**readgeo**: subroutine for the input of the initial geometry.

**readbez**: subroutine for the input of the control points at the beginning of the process instead of the airfoil’s geometry.

**menuobj**: subroutine for the control of the GUI regarding objective function parameters.

**menug**: subroutine for the control of the GUI regarding the management of constraints.

**menudof:** subroutine for the control of the GUI regarding the management of degrees of freedom.

**opt:** subroutine deputed to the control of the optimization process.

**x2bez:** subroutine for the conversion of degrees of freedom's vector  $X$  to Bezier control points.

**outgeo:** subroutine for the storage of the test geometry during the optimization process.

**evalg\_geo:** subroutine dedicated to the geometrical constraints evaluation.

**evalg\_aero:** subroutine dedicated to the aerodynamic constraints evaluation.

**evalobj:** subroutine dedicated to the evaluation of the objective function.

**outfinalgeo:** subroutine for the storage of the optimal configuration.



## References

1. Chong, E., K., P., Zak, S., K., “An Introduction to Optimization”, Wiley, 2001.
2. Pedregal, P., “Introduction to Optimization”, Springer, 2004.
3. Mitchell, M., “An Introduction to Genetic Algorithms”, MIT Press, 1999.
4. Drèo, J., Petrowski, A., Siarry, P., Taillard, E., “Metaheuristics for Hard Optimization”, Springer, 2006.
5. Fletcher, R., “Practical Methods of Optimization”, Wiley, 1987.
6. Vanderplaats, G., N., “Numerical Optimization Techniques for Engineers Design: with applications”, 3<sup>rd</sup> edition, Vanderplaats Research & Development Inc., Colorado Springs, CO, 1999.
7. “Optimum Design Methods for Aerodynamics”, AGARD-R-803, 1994.
8. Drela, M., “XFOIL 6.94 User Guide”, MIT Aero & Astro, Dec 2001.
9. Drela, M., “A User’s Guide to MSES 2.9”, MIT Computational Aerospace Sciences Laboratory, October 1995.
10. Rizzi, “EZ- Guide to MSES”, KTH Flyg.
11. Coiro, D.P., de Nicola, C., “Prediction of Aerodynamic Performance of Airfoils in Low Reynolds Number Flows”, Low Reynolds Number Aerodynamics Conference, NotreDame, USA, 1989.
12. Coiro, D.P. Dini P., “Stall and Post-Stall Performance Prediction of Advanced Wind Turbine Airfoils”, XII



- AIDAA National Congress, Como, July 1993.
13. Coiro, D.P. and Dini, P., “The Prediction of Aerodynamic Stall Over Wind-Turbine Airfoils”, International Conference on fluid and thermal energy conversion, Yogyakarta, Indonesia, 1997.
  14. Selig, M., Guglielmo, J.,J., “High-Lift low Reynolds number airfoil design”, AIAA, 1997
  15. Selig, M., S., Lyon, A., Giguere, P., Ninham, C., P., Guglielmo, J., J., “Summary of Low-Speed Airfoil Data”, Vol.2, Soartech Publications, ISBN 0-9646747-2-6
  16. Somers D.M., Maughmer M.D., “The SM701 an Airfoil for World Class Sailplanes”, XXII OSTIV Congress, Uvalde, Texas, USA, 1991.
  17. Landman, D., Britcher, P., “Experimental Geometry Optimization Techniques for Multi-Elements Airfoils”, Journal of Aircraft, Vol. 37, n. 4, July-August 2000.
  18. Eppler, R., Somers, D.,M., “A Computer Program for the Design and Analysis of Low-Speed Airfoils”, NASA-TM-80210, 1980.
  19. Eppler, R., “Airfoil Design and Data”, Springer Verlag, 1990.
  20. “Special Course on Inverse Methods for Airfoil Design for Aeronautical and Turbomachinery Applications”, AGARD-R-780, 1990.
  21. Katz, J., Plotkin, A., “Low-Speed Aerodynamics”, Cambridge University Press, 2001.
  22. Anderson, J., D., Jr, “Fundamentals of Aerodynamics”, McGraw Hill, 1991.
  23. Prandtl, L., “Tragflugel Theorie”, Nachrichten von der Gesellschaft der Wissenschaften zu Gottingen, Geschaefliche Mitteilungen, Klasse, 1918, pp. 451–477.

24. Phillips, W., F. “Mechanics of Flight”, Wiley, 2004.
25. Phillips, W., F., Snyder, D., O., “Modern Adaptation of Prandtl’s Classic Lifting Line Theory”, *Journal of Aircraft*, Vol.37, No.4, July-August, 2000.
26. Losito, V., “Estensione della teoria della linea portante alle ali di basso allungamento”, *L’Aerotecnica Missili e Spazio* 2/3, 1971.
27. Chattot, J.,J., “Computational Aerodynamics and Fluid Dynamics”, Springer, 2004.
28. Chattot, J.,J., “Analysis and design of wings and wing/winglet combinations at low speeds”, *CFD Journal* No.10, 2004
29. Kroo I., “Drag due to Lift: Concepts for Prediction and Reduction”, *Annual Reviews Fluid. Mech*, 2001.
30. Coiro, D.P., Nicolosi, F., Scherillo, F., Maisto, U., “Improving Hand-Glider Maneuverability Using Multiple Winglets: a Numerical and Experimental Investigation”, *Journal of Aircraft*, Vol.45, No.3, May-June, 2008.